



**Stress Changes in the Shillong Plateau and the Cause
of the Seismic Gap in the Eastern Himalaya**

Adi Saric

Dalhousie University, Halifax, Nova Scotia, Canada, B3H 4R2

SUBMITTED IN PARTIAL FULFILLMENT OF THE REQUIREMENTS FOR THE
DEGREE OF BACHELOR OF SCIENCE, HONOURS, DEPARTMENT OF EARTH
SCIENCE, DALHOUSIE UNIVERSITY, HALIFAX, NOVA SCOTIA
MARCH 17TH, 2014

Distribution License

DalSpace requires agreement to this non-exclusive distribution license before your item can appear on DalSpace.

NON-EXCLUSIVE DISTRIBUTION LICENSE

You (the author(s) or copyright owner) grant to Dalhousie University the non-exclusive right to reproduce and distribute your submission worldwide in any medium.

You agree that Dalhousie University may, without changing the content, reformat the submission for the purpose of preservation.

You also agree that Dalhousie University may keep more than one copy of this submission for purposes of security, back-up and preservation.

You agree that the submission is your original work, and that you have the right to grant the rights contained in this license. You also agree that your submission does not, to the best of your knowledge, infringe upon anyone's copyright.

If the submission contains material for which you do not hold copyright, you agree that you have obtained the unrestricted permission of the copyright owner to grant Dalhousie University the rights required by this license, and that such third-party owned material is clearly identified and acknowledged within the text or content of the submission.

If the submission is based upon work that has been sponsored or supported by an agency or organization other than Dalhousie University, you assert that you have fulfilled any right of review or other obligations required by such contract or agreement.

Dalhousie University will clearly identify your name(s) as the author(s) or owner(s) of the submission, and will not make any alteration to the content of the files that you have submitted.

If you have questions regarding this license please contact the repository manager at dalspace@dal.ca.

Grant the distribution license by signing and dating below.

Name of signatory

Date

DATE: April 24th, 2014

AUTHOR. Adi Sarie

TITLE: Stress Changes in the Shillong Plateau and the Cause of the Seismic
Gap in the Eastern Himalaya

Degree: B.Sc. (Honours) Convocation: MAY Year: 2014

Permission is herewith granted to Dalhousie University to circulate and to have copied for non-commercial purposes, at its discretion, the above title upon the request of individuals or institutions.

THE AUTHOR RESERVES OTHER PUBLICATION RIGHTS, AND NEITHER THE THESIS NOR EXTENSIVE EXTRACTS FROM IT MAY BE PRINTED OR OTHERWISE REPRODUCED WITHOUT THE AUTHOR'S WRITTEN PERMISSION.

THE AUTHOR ATTESTS THAT PERMISSION HAS BEEN OBTAINED FOR THE USE OF ANY COPYRIGHTED MATERIAL APPEARING IN THIS THESIS (OTHER THAN BRIEF EXCERPTS REQUIRING ONLY PROPER ACKNOWLEDGEMENT IN SCHOLARLY WRITING) AND THAT ALL SUCH USE IS CLEARLY ACKNOWLEDGED.

ABSTRACT

The 2,500 km long Himalayan-Tibetan orogen is characterized by areas of low seismicity known as seismic gaps. One potential seismic gap is that of the Bhutan Himalaya, where seismicity is more than four times less than the mean seismicity of the HSB. Different hypotheses have been proposed as to the cause of the putative seismic gap, but almost all are directly related to the Shillong Plateau of eastern India. This uplifted pop-up structure of the eastern Himalaya is bounded by two reverse faults, the Oldham and Dauki. The 1897 Mw~8.1 Great Assam earthquake occurred along the Oldham fault and is thought to have altered the stress environment, potentially resulting in the formation of a stress shadow contributing to the seismic gap of the Bhutan Himalaya to the north.

This study attempts to model the 1897 Great Assam earthquake using Coulomb 3.3, a graphic-rich deformation and stress-change software. The goal is to model the potential Coulomb stress change that resulted from the earthquake using known geologic and seismic parameters. Determining the Coulomb stress change imparted to nearby receiver faults as a result of slip along the Oldham fault is the most important aspect of this research study, as nearby faults in the region could pose a future threat for seismic hazards.

This topic of research is of the utmost importance as stress taken up by nearby receiver faults could be released in the near future through seismic events. Seismic hazards pose a serious threat to the region, as population and population density is very large in the Brahmaputra valley to the north of the Shillong Plateau, and especially that of Bangladesh to the south. Furthermore, infrastructure is not well equipped to handle such seismic hazards. Therefore, it is crucial to investigate the Coulomb stress change that occurred as a result of the earthquake in order to determine the future location of possible seismic events.

Results suggest that Coulomb stress change, as a result of the 1897 Great Assam earthquake, did contribute to the formation of a stress shadow that coincides with part of the putative seismic gap along the Bhutan Himalaya. The resulting stress shadow coincides with the frontal ramp of the MFT south of the Bhutan Himalaya. The drop in Coulomb stress could have had a potentially significant effect on seismicity along the seismogenic detachment in the area. The lack of seismicity due to a drop in Coulomb stress would result in less stress transfer to the basal detachment segment of the MFT leading to prolonged stress and strain accumulation, in turn contributing to lower seismicity levels. Furthermore, Coulomb stress change was imparted to nearby strike-slip faults in the region with the majority incurring a small decrease in Coulomb stress. Large increases in Coulomb stress were imparted to the Dauki fault making it the highest risk for a future seismic event. Future work and research should be aimed at determining a time frame for the recurrence of seismic events, especially along the Dauki fault.

KEYWORDS

- 1) Coulomb envelope:** The linear failure envelope predicted by the Coulomb fracture criterion
- 2) Shear fracture:** Fracture with detectable wall-parallel displacement. Different from faults in that it only consists of a single fracture, while faults are composed of a number of linked fractures
- 3) Extension fracture:** Fracture formed by extension perpendicular to the fracture walls
- 4) Shear stress:** Stress acting parallel to a plane of reference
- 5) Normal stress:** Stress or stress component acting perpendicular to the surface of reference
- 6) Brittle Deformation:** Deformation by fracturing (discontinuous deformation)
- 7) Seismogenic Zone:** The zone of frequent earthquakes in the crust, which is the middle and lower part of the brittle crust, where the crust is the strongest
- 8) Mohr Circle:** Circle in the Mohr diagram that describes the normal and shear stress acting on planes of all possible orientations through a point in the rock

TABLE OF CONTENTS

<u>Table of Figures</u>	6
<u>Table of Tables</u>	8
<u>Acknowledgments</u>	9
<u>1.0 Introduction</u>	10
<u>2.0 Geologic Setting</u>	14
<u>2.1 Himalayan Orogen</u>	<u>15</u>
<u>2.2 Shillong Plateau</u>	<u>19</u>
<u>2.3 1897 Great Assam Earthquake</u>	<u>24</u>
<u>2.4 Plate Convergence and Himalayan Contraction Rates</u>	<u>25</u>
<u>2.5 Himalayan Seismic Belt and Seismic Gaps</u>	<u>29</u>
<u>2.6 Open Geological Questions – Seismic Hazards in the Eastern Himalaya</u>	<u>33</u>
<u>3.0 Methodology</u>	35
<u>3.1 Coulomb Fracture Criterion</u>	<u>36</u>
<u>3.2 Coulomb Stress Change and Transfer</u>	<u>42</u>
<u>3.3 Coulomb 3.3</u>	<u>51</u>
<u>3.4 Model Formulations and Parameters</u>	<u>59</u>
<u>4.0 Results</u>	66
<u>4.1 Map View Coulomb Stress Change Patterns</u>	<u>67</u>

<u>4.2 Cross Section Coulomb Stress Change Patterns</u>	<u>71</u>
<u>4.3 Optimally Oriented Coulomb Stress Change</u>	<u>76</u>
<u>4.3.1 Coulomb Stress Change Pattern along the Oldham Fault</u>	<u>79</u>
<u>4.3.2 Coulomb Stress Change Pattern along the Dauki Fault</u>	<u>81</u>
<u>4.3.3 Coulomb Stress Change Pattern along the MFT</u>	<u>82</u>
<u>4.3.4 Coulomb Stress Change Pattern along Strike-Slip Faults</u>	<u>83</u>
<u>4.4 Differences in Coulomb Stress Change Pattern Between Regional Stress Values</u>	<u>84</u>
<u>5.0 Discussion</u>	<u>86</u>
<u>5.1 Coulomb Stress Change on Receiver Faults</u>	<u>87</u>
<u>5.1.1 Coulomb Stress Change on all Receiver Faults</u>	<u>88</u>
<u>5.1.2 Coulomb Stress Change on the Dauki Fault</u>	<u>90</u>
<u>5.1.3 Coulomb Stress Change on the Kopili Fault</u>	<u>95</u>
<u>5.1.4 Coulomb Stress Change on the Frontal Ramp of the MFT</u>	<u>97</u>
<u>5.1.5 Coulomb Stress Change on the Sakteng Fault</u>	<u>99</u>
<u>5.1.6 Coulomb Stress Change on the Tista Fault</u>	<u>101</u>
<u>5.2 Cause of the Seismic Gap in the Bhutan Himalaya</u>	<u>103</u>
<u>6.0 Conclusion</u>	<u>105</u>
<u>6.1 Recommendations for Future Research</u>	<u>112</u>
<u>7.0 References</u>	<u>113</u>
<u>8.0 Appendix</u>	<u>119</u>

TABLE OF FIGURES

<u>Figure 2.1 – Cross-section of the Himalayan-Tibetan orogen</u>	<u>17</u>
<u>Figure 2.2 – Southern Bhutan and the Shillong Plateau</u>	<u>19</u>
<u>Figure 2.3 – Bilham and England model of the Shillong Plateau</u>	<u>20</u>
<u>Figure 2.4 – Biswas et al. model of the Shillong Plateau</u>	<u>21</u>
<u>Figure 2.5 – Clark and Bilham model of the Shillong Plateau</u>	<u>23</u>
<u>Figure 2.6 – Area affected by 1897 Great Assam Earthquake</u>	<u>24</u>
<u>Figure 2.7 – Convergence rates of NW and NE India</u>	<u>25</u>
<u>Figure 2.8 – Reconstructed convergence positioning of India</u>	<u>26</u>
<u>Figure 2.9 – Deformation across northern India and the Himalaya</u>	<u>27</u>
<u>Figure 2.10 – Seismicity of the HSB</u>	<u>31</u>
<u>Figure 2.11 – Stress shadow along the Bhutan Himalaya</u>	<u>33</u>
<u>Figure 3.1 – Coulomb Fracture Criterion</u>	<u>37</u>
<u>Figure 3.2 – Shear Strength vs. Depth</u>	<u>38</u>
<u>Figure 3.3 – Confining Pressure vs. Differential Stress</u>	<u>38</u>
<u>Figure 3.4 – Criterion for Frictional Sliding</u>	<u>39</u>
<u>Figure 3.5 – Mohr Circles in Space</u>	<u>40</u>
<u>Figure 3.6 – Coulomb, Griffith, and Von Mises Criteria in Mohr Space</u>	<u>41</u>
<u>Figure 3.7 – Coulomb stress change for Specified Receiver Faults</u>	<u>43</u>
<u>Figure 3.8 – Coulomb stress change for Optimally Oriented Receiver Faults</u>	<u>44</u>
<u>Figure 3.9 – Coulomb stress change as a function of fault length</u>	<u>46</u>
<u>Figure 3.10 – Coulomb stress change along thrust faults</u>	<u>48</u>
<u>Figure 3.11 – Coulomb stress change imparted as a function of fault length</u>	<u>50</u>

<u>Figure 3.12 – Aki and Richards 1980 Convention for Fault Geometry</u>	52
<u>Figure 3.13 – Orientation of Optimal Planes based on Regional Stress</u>	57
<u>Figure 3.14 – Effects of Regional Stress and Effective Friction</u>	58
<u>Figure 4.1 – Map View Coulomb Stress-Change Patterns</u>	68-70
<u>Figure 4.2 – Cross Section Coulomb Stress-Change Pattern – East</u>	72
<u>Figure 4.3 – Cross Section Coulomb Stress-Change Pattern – Central</u>	73
<u>Figure 4.4 – Cross Section Coulomb Stress-Change Pattern – West</u>	74
<u>Figure 4.5 – Cross Section Coulomb Stress-Change Pattern – Perpendicular</u>	75
<u>Figure 5.1 – Coulomb Stress Change on all Receiver Faults</u>	89
<u>Figure 5.2 – Coulomb Stress Change on the Dauki Fault (± 10 bar)</u>	91
<u>Figure 5.3 – Coulomb Stress Change on the Dauki Fault ($\pm 10, 50, 99$ bar)</u>	93
<u>Figure 5.4 – Coulomb Stress Change on the Kopili Fault</u>	96
<u>Figure 5.5 – Coulomb Stress Change on the Frontal Ramp of the MFT</u>	98
<u>Figure 5.6 – Coulomb Stress Change on the Sakteng Fault</u>	100
<u>Figure 5.7 – Coulomb Stress Change on the Tista Fault</u>	102
<u>Figure 6.1 – Seismicity of the Shillong Plateau</u>	107
<u>Figure 6.2 – Seismicity of the Kopili Fault</u>	109

TABLE OF TABLES

Table 3.1 – Fault Parameters **61**

Table 3.2 – Regional Stress Values **61**

ACKNOWLEDGEMENTS

First and foremost, I would like to thank my supervisor Dr. Djordje Grujic for giving me the opportunity and pleasure of working with him on my honours thesis. Dr. Grujic has been a professor of mine for the past several years and having the chance to work with him on such an interesting and extensive project is truly an honour and has been a wonderful experience from beginning to end. The geology of the Himalaya was something I was not familiar with at first, but with the help of my supervisor's excellent teaching, world-class knowledge, and superb guidance I have learned more about the geology of the Himalaya than I thought I ever would in such a short time period.

I would also like to thank Dr. Martin Gibling for his tremendous effort in coordinating the EARTH 4200 course and helping me with the writing and editing process. Your effort in these matters was crucial to a sound and coherent thesis. This research study would also not have been possible without the help of Dr. Ross Stein of the USGS. His support and guidance with the use of Coulomb 3.3 was invaluable. Furthermore, I would like to thank Dr. Keith Loudon for his input in modeling and for being one of my co-readers. I would also like to thank John Thibodeau for his technical support in the lab. Lastly, I would like to thank the Earth Science Department for giving me the opportunity to learn from a group of experienced, well-trained, and knowledgeable professionals in a wonderful academic environment.

1.0 INTRODUCTION

The Himalaya and Tibetan Plateau are amongst the most seismically active intra-continental regions in the world. Earthquakes occur as small-, medium-, and large-scale events, but seismicity appears to be non-uniform in geographic occurrence and distribution (Bilham, 2004). Seismicity is both shallow and deep in the Tibetan Plateau and along the Himalayan front, but is generally deeper in the latter (Drukpa et al., 2006). Seismicity occurs on normal, reverse, thrust, and strike-slip faults. The seismic events along the Himalayan front are predominantly associated with thrust faults, whereas strike-slip faulting dominates in the eastern Himalaya (De and Kayal, 2003; Drukpa et al., 2006).

Deformation and earthquakes are localized, and generally occur along plate boundaries. This is evident in that the majority of earthquakes in the region have occurred along the northern boundary of the Indian subcontinent, where the Indian plate is thrust underneath Eurasia. However, intraplate deformation does occur and can lead to the occurrence of earthquakes, including those of large magnitude. Three of the largest recorded intraplate earthquakes have occurred within the Indian subcontinent (Bilham, 2004; Banerjee et al., 2008). Within India, the largest earthquakes have occurred in the Gujarat region to the west, and more importantly for this study in northeastern India near the Shillong Plateau (Bilham, 2004; Banerjee et al., 2008).

Unlike the central and western regions of the Himalaya, the seismotectonics and seismic history of the Bhutan Himalaya are relatively unknown. Furthermore the Bhutan Himalaya have been characterized as a low-seismicity region, also

known as a seismic gap (Gahalaut et al., 2011). Velasco et al. (2007) showed that a high amount of micro-seismicity occurs in southern Bhutan, but relatively little or no seismicity in northern Bhutan and southern Tibet directly to the north. Moderate-sized earthquakes have occurred in the region, but it has been proposed that the Bhutan Himalaya have been inactive at the >6.5 Mw level for the last sixty years (Drukpa et al., 2006). There are several hypotheses for why this area has been relatively inactive, despite being located in a region of highly active seismicity. One of the leading hypotheses for the lack of seismicity in the Bhutan Himalaya is the stress shadow that was potentially created as a result of the 1897 Mw ~ 8.1 Great Assam earthquake (Bilham and England, 2001; Banerjee et al., 2008; Gahalaut et al., 2011).

The Mw ~ 8.1 earthquake occurred along the Oldham fault on June 12th, 1897 and was one of the largest recorded intraplate earthquakes (Bilham and England, 2001; Banerjee et al., 2008). The Oldham fault is one of two bounding faults of the Shillong Plateau, the other being the Dauki fault (Bilham and England, 2001). Both faults are reverse faults, but several strike-slip faults are associated with them (Bilham and England, 2001; De and Kayal, 2003; Velasco et al., 2007; Bhattacharya et al., 2008; Mukul et al., 2014). It has been proposed that such an enormous release of stress energy associated with the earthquake has resulted in a stress shadow (Gahalaut et al., 2011).

Research on this topic is crucial because the 1897 Great Assam earthquake may have resulted in stress accumulation along nearby faults, which can result in future earthquakes of significant magnitude or may have decreased the stress level

thereby increasing the inter-seismic period (Gahalaut et al., 2011). Analyzing seismic hazard risk in this region is of utmost importance due to the immense population density in the Brahmaputra valley to the north of the Shillong Plateau, and especially that of Bangladesh to the south. Following the 1897 Great Assam earthquake local reports indicated that all stone and masonry buildings were destroyed within a region comparable to the size of England, and aftershocks were felt within an even greater range (Oldham, 1899 in Bilham and England, 2001). Casualties were relatively low, but given the extreme increase in population and population density that has occurred in the area since 1897, an earthquake of similar magnitude today would result in far more damage and loss of life.

My thesis topic is centered on Coulomb stress change in the area of the Shillong Plateau, and how it may have influenced the seismicity of the Bhutan Himalaya. The goal is to determine the degree of Coulomb stress change that has occurred as a result of the 1897 Great Assam earthquake, and how and where stress is being partitioned through the various faults in the area. Using software developed by the USGS I performed numerical modeling to determine potential scenarios of Coulomb stress change. The initial step of research was to replicate the 1897 Great Assam earthquake through numerical modeling. This allowed me to infer where and how Coulomb stress had changed. Subsequently, I modeled various scenarios of stress transfer using different faults present in the region. The primary goal of this research study was to determine where stress is being built up and through which faults stress is currently being transferred. I hope this work will help

determine the location of future seismic events that may occur, and their recurrence interval.

2.0 GEOLOGIC SETTING

The Himalaya span approximately 2,500 km from northwest to southeast from Pakistan to India, and are also present in Bhutan and Nepal. The orogen is home to the tallest mountains in the world with over 100 peaks reaching 7,200 m and 14 reaching 8,000 m above sea level, with Mt. Everest being the highest peak at 8,848 m (Hodges, 2000).

2.1 HIMALAYAN OROGEN

The Himalaya are the result of continent-continent collision and ongoing convergence between the Eurasian and Indian plates (Hodges, 2000; Drukpa et al., 2006). The plate boundary is known as the Indus-Tsangpo suture zone (Hodges, 2000). The Himalayan arc is anchored by two syntaxes: Namche Barwa to the east and Nanga Parbat to the west, which are named after major mountain peaks (Hodges, 2000). The Tibetan Plateau is intimately associated with the Himalayan arc and together they are referred to as the Himalayan-Tibetan orogen. The Tibetan Plateau is composed of a high central region with very low relief and an average elevation of >5,000 m above sea level (Fielding et al., 1994). The precursor of the Tibetan Plateau formed during the Mesozoic Era through the accretion of several exotic terranes to Eurasia (Kapp et al., 2005). Since collision, there has been an estimated 1,800 km of shortening between India and Eurasia in the western section of the orogenic system (Clark, 2012). In the eastern section there has been up to 2,750 km of shortening, with the greater amount due to the counter-clockwise rotation of the Indian Plate (Hodges, 2000). Such contraction has been accommodated by shortening throughout the Himalaya and Tibet, but the removal of lithosphere through subduction and extrusion also played a role (Tapponnier et al., 1982; Tapponnier et al., 2001).

The tectonic history of the Himalayan-Tibetan orogen has been divided into three phases of deformation, which are distinguished by transitions in the style of deformation. They are, from oldest to most recent, the Protohimalayan, Eohimalayan, and Neohimalayan Phases (Hodges, 2000). The Protohimalayan

Phase occurred from the Late Cretaceous to Early Eocene. This phase occurred prior to the collision between the Indian and Eurasian plates and includes deformation that affected the Transhimalayan and Tibetan zones and Indus-Tsangpo suture zone (Hodges, 2000). The most prominent structure from this phase is the south- to southwest-directed fold and thrust belt of the Transhimalayan zone.

The India-Eurasia collision, and subsequent deformation that occurred from the Middle Eocene to Late Oligocene, is defined as the Eohimalayan Phase (Hodges, 2000). The collision is estimated to have occurred between 54-50 Ma (Searle et al., 1997; Najman et al., 2010). High and ultra-high pressure rocks of the Tibetan Zone are evidence of Indian plate subduction during this period (Pognante et al., 1991; Guillot et al., 1995). The main structures include fold-and-thrust nappes in eastern Ladakh and the southward-directed Gangdese thrust.

Tectonics of the Himalayan-Tibetan orogen from the Early Miocene to the present day are represented by the Neohimalayan Phase (Hodges, 2000). The related structures are present throughout the entire orogen and its tectonostratigraphic zones. Most important of these structures are the south-vergent thrusts and a north-vergent low angle detachment. These sub-parallel, crustal-scale shear zones separate the Tethyan sedimentary sequence (TSS), Greater Himalayan sequence (GHS), Lesser Himalayan sequence (LHS), Subhimalayan zone, and the Quaternary foreland from one another (Hodges, 2000) (Figure 2.1). The South Tibetan detachment system (STD) consists of a low-angle, north-dipping, normal-geometry ductile shear zone and steeper brittle normal faults (Kellet and

Grujic, 2012). The north-dipping Main Central Thrust (MCT) is structurally the highest and oldest of all the fault systems. It separates the Greater Himalayas from the Lesser Himalayas (Searle et al. 2008). It is a ductile shear zone that ranges from hundreds of meters to several kilometers in thickness. The MCT mylonites are derived from both GHS and LHS units and the onset of shearing is estimated to have been at 23 Ma (Hodges, 2000).

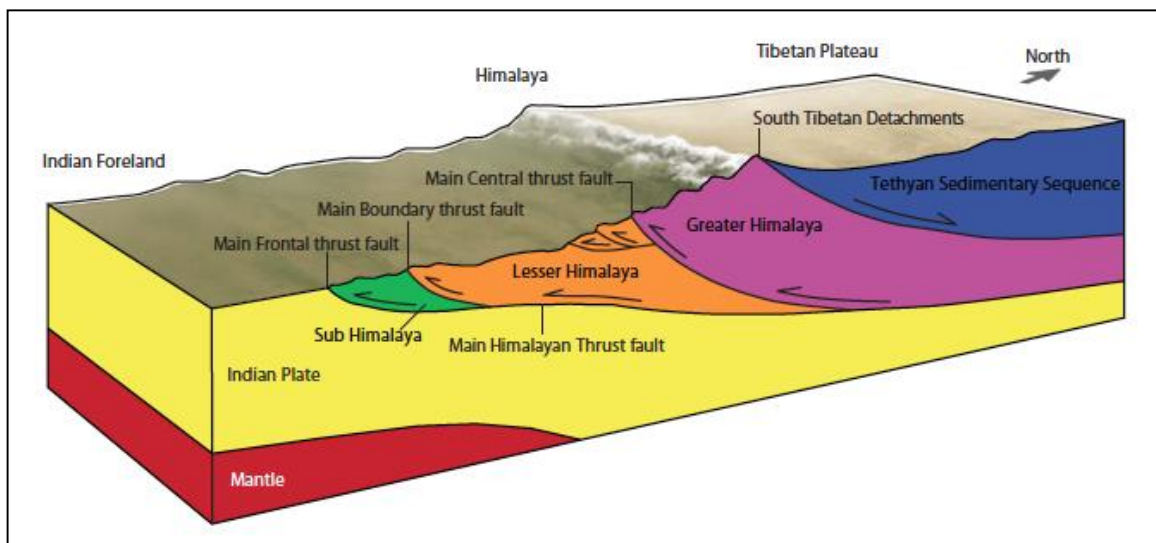


Figure 2.1: Schematic cross-section and block diagram of the Himalayan-Tibetan Orogen showing major faults (Hirschmiller, 2013).

The Main Boundary Thrust (MBT) is the tectonic boundary between the Lesser Himalayan and Subhimalayan zone (Hodges, 2000). Sedimentation patterns in the Subhimalayan zone have placed an age of 11-9 Ma on the MBT (Meigs et al., 1995). The MBT consists of a series of north-dipping thrusts, with a narrow ~100 m wide brittle-ductile shear zone. The Main Frontal Thrust (MFT) separates the Subhimalayan zone from the Indo-Gangetic Plain (Hodges, 2000). It is perceived to be a décollement. Movement along the MFT began $2.5 \text{ Ma} \pm 0.5 \text{ Ma}$ (van der Beek et al., 2006). All three thrust systems, the MCT, MBT, and the MFT are splays of the

main décollement system known as the Main Himalayan Thrust (MHT) (Nelson et al., 2006) (Figure 2.1).

The Himalayan-Tibetan orogen can be divided into several kinematic domains (Andronicos et al., 2007). The various kinematic domains of the Himalayan-Tibetan orogen are characterized by their topography and reflect mechanical transitions in the deformation and stress environment (Andronicos et al., 2007).

2.2 SHILLONG PLATEAU

South of the Bhutan Himalaya, the Shillong Plateau stretches east-west for ca. 400 km. It is the only elevated area and only active structure in the southern foreland basin of the Himalaya. The plateau is bounded by two reverse faults, the Dauki and Oldham (Figure 2.2). The Dauki fault is the surface-exposed southern bounding fault and the longer of the two. It is ~194 km long and dips 50° N with a strike of 270° (Biswas and Grasemann, 2005). The Oldham fault is the northern bounding fault and the location of the 1897 Great Assam earthquake (Mw ~8.1) (Bilham and England, 2001). The Oldham fault is blind, ~110 km long, and dips 57° SSW with a strike of 113° (Bilham and England, 2001). The 1897 Great Assam earthquake occurred along the Oldham fault with a rake of 76° between 9-45 km depth, resulting in 16 m of net slip (Bilham and England, 2001).

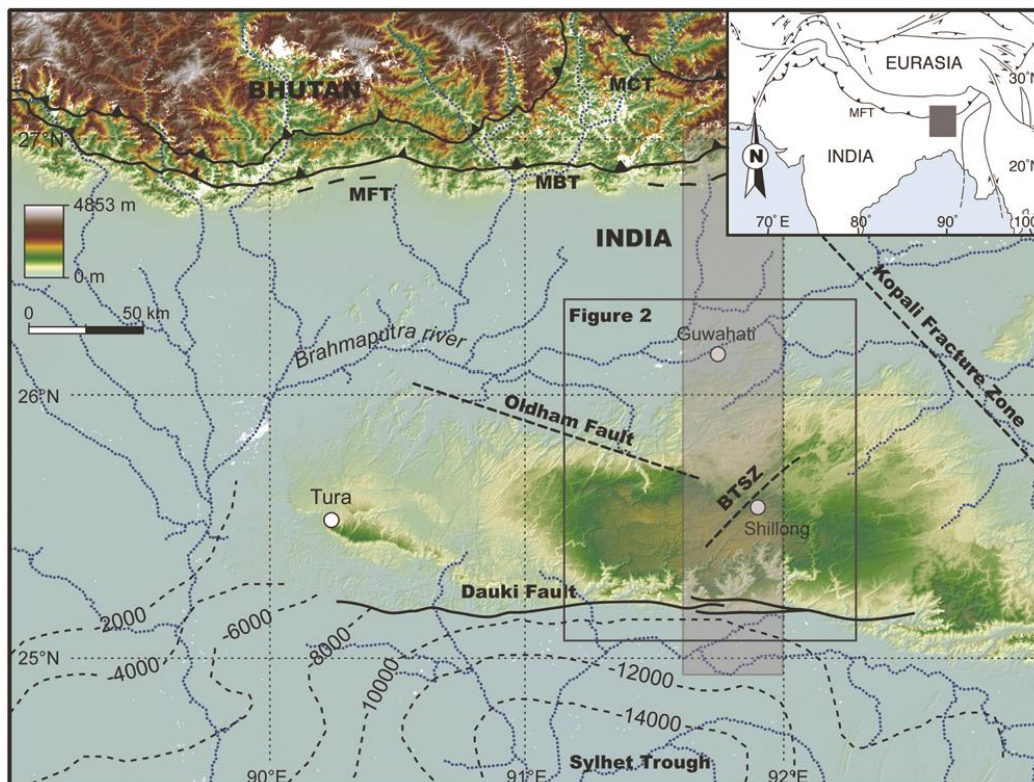


Figure 2.2: Major structural features of southern Bhutan and the Shillong Plateau overlain on digital topography (Biswas et al., 2007).

There are several theories as to what sustains the uplift of the Shillong Plateau. According to the first, the north-dipping Dauki and south-dipping Oldham faults form a pop-up structure that incorporates the Shillong Plateau (Bilham and England, 2001). Equal rates of displacement along a set of conjugate reverse faults dipping at 50° allow for an evenly uplifting pop-up structure (Bilham and England, 2001) (Figure 2.3). Bilham and England (2001) estimated a vertical displacement rate of 2.5 ± 1 mm/yr along each fault and a combined horizontal shortening rate of

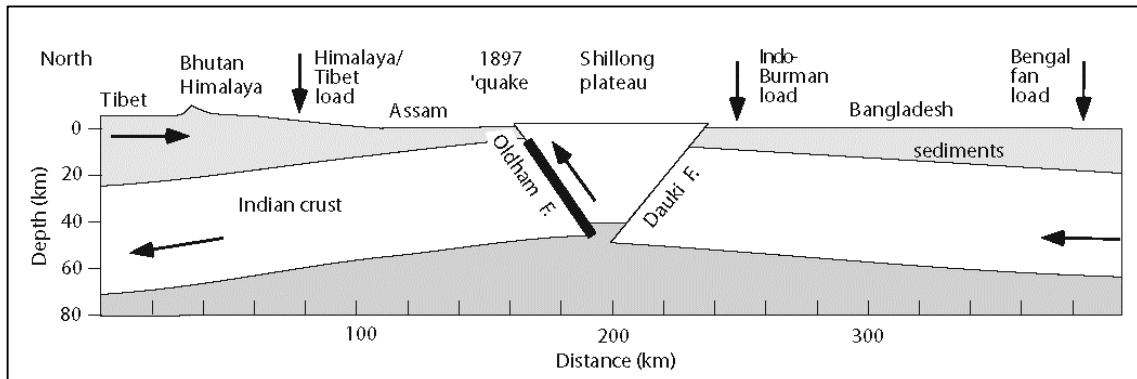


Figure 2.3: North-south cross-section from Tibet to the Bay of Bengal showing the pop-up structure of the Shillong Plateau (Bilham and England, 2001).

4 ± 2 mm/yr. Bilham and England (2001) noted that in-plane compressional stress from continued plate convergence is the main driving force of uplift. Initiation and sustained uplift of the plateau may also be due to flexure and bending of the Indian Plate because of the Himalaya in the north and Bengal fan sediments up to 23 km thick to the south and east of the region. The third source of crustal load is the westward overthrust of Indo-Burman ranges. Furthermore, the Dauki fault was a strike-slip fault during the Miocene, but transitioned to a reverse fault during the

Pliocene allowing for dip-slip movement, therefore contributing to the uplift and pop-up nature of the plateau (Bilham and England, 2001).

Biswas et al. (2007) showed that exhumation of plateau basement rock began at approximately 9-15 Ma, whereas surface uplift of the plateau started at approximately 3-4 Ma. Based on the calculated depth of burial by the now eroded Tertiary sediments and cooling rates, the Dauki fault was estimated to have a vertical displacement rate of 0.77-1.25 mm/yr and the Oldham fault a rate of 0-0.68 mm/yr. The faster displacement rate along the Dauki fault has contributed to a 2-3° northward tilting of the Shillong Plateau surface, which may have been exacerbated by northward tilting of Indian crust as a result of flexure due to tectonic loading by the Himalayan orogen (Figure 2.4). The surface uplift rate of the plateau was

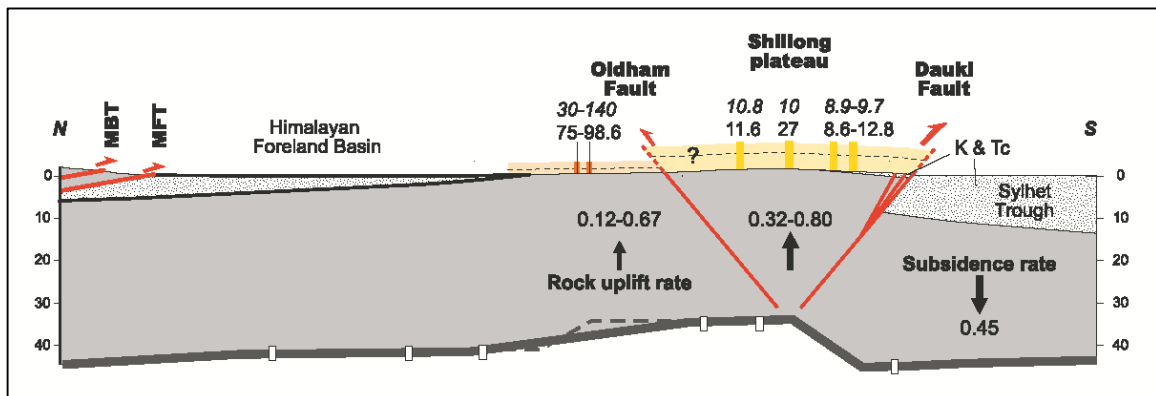


Figure 2.4: North-south cross-section from the Himalayan foreland basin to the Sylhet Trough showing the Shillong Plateau. Red lines represent major faults and yellow bars correspond to maximum thickness of sedimentary cover. Rock uplift rates of the Oldham and Dauki faults are shown and the subsidence rate of the Dauki footwall (Sylhet Trough) is also given. The position of the Moho is shown with white boxes (Biswas et al., 2007).

estimated to have been 0-0.57 mm/yr during the last 9-15 Ma, but accelerated to 0.4-0.53 mm/yr during the last 3-4 Ma as a result of erosion and removal of Late Cretaceous-Tertiary sedimentary cover. Lastly, the cumulative horizontal shortening rate has been estimated at 0.65-2.3 mm/yr, which represents only 10-

15% of the Himalayan contraction rate. Their results suggest that India-Eurasia convergence partitioning between the Shillong Plateau and Himalaya is minor and that tectonic development of the plateau did not affect rates of shortening and uplift in the Bhutan Himalaya since onset of exhumation of the basement of the Shillong Plateau at approximately 9-15 Ma (Biswas et al., 2007).

Clark and Bilham (2008) have proposed that the Shillong Plateau is a structural wedge. They hypothesize a blind, north-dipping, master fault that bifurcates into a north-dipping fold axial plane (Dauki fault) and a south-dipping backthrust (Oldham fault) that forms a topographic step (Figure 2.5). In their model, the Dauki fault is a northward-migrating fold axis that propagates from the master fault, which dips at $\sim 53^\circ$. The fold axis migrates northward as the structure grows over time. Their model assumes that faulting and fold growth began approximately 8-14 Ma. Clark and Bilham (2008) proposed an average vertical fault slip rate of 0.7-1.4 mm/yr and an average horizontal slip rate of 1.0-2.0 mm/yr, similar to the values proposed by Biswas et al. (2007).

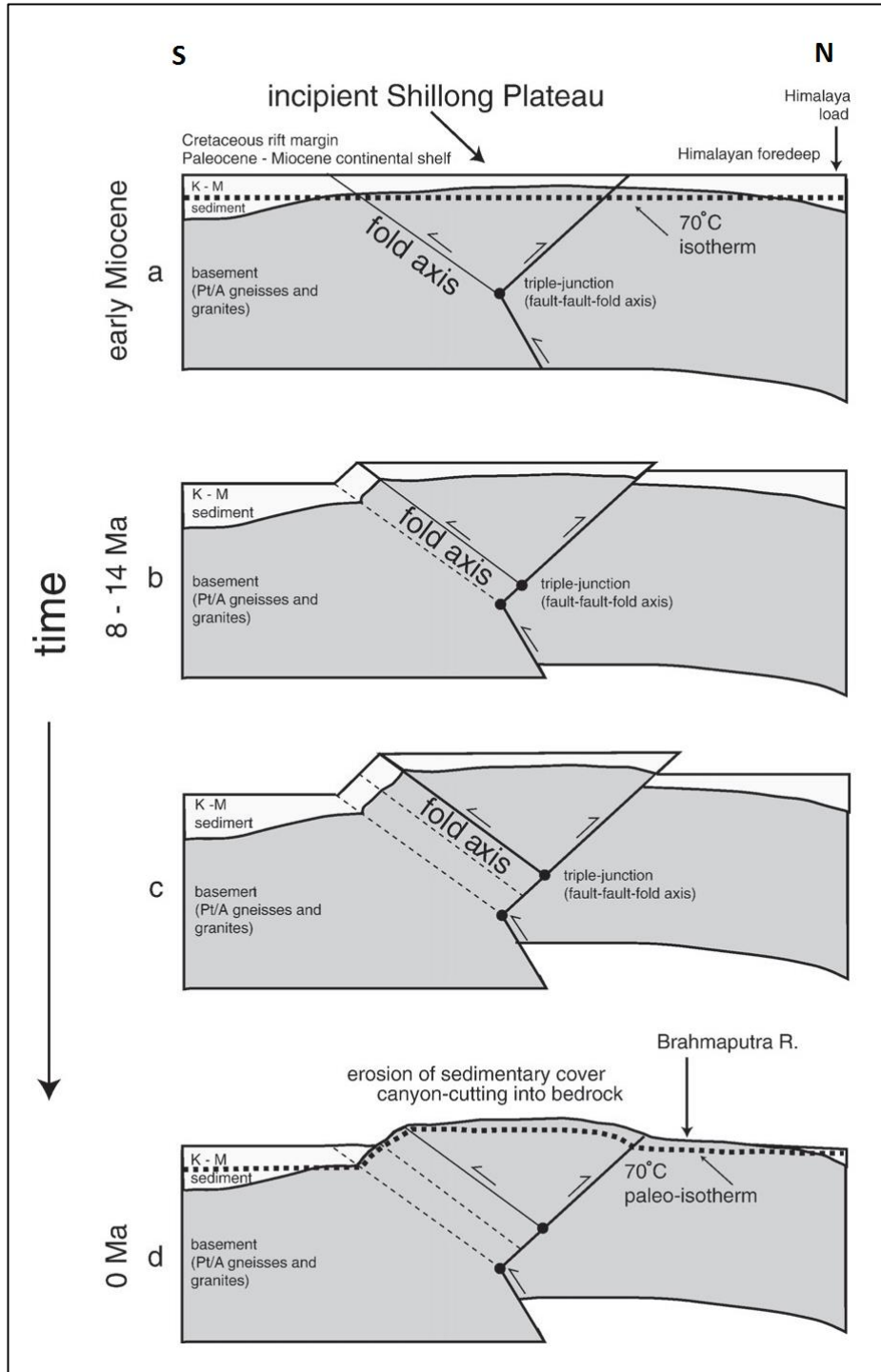


Figure 2.5: North-south cross-section from the Himalayan foredeep to the Sylhet Trough showing the structural evolution of the Shillong Plateau. Motion along the master deep fault initiates the folding of basement rocks above the southern boundary and development of the backthrust to the north. Sedimentary cover is eroded with progressive upward movement. The thick dashed line represents the partial retention zone (PRZ). Modified from (Clark and Bilham, 2008).

2.3. 1897 GREAT ASSAM EARTHQUAKE

Most earthquakes of the Shillong Plateau occur at depths between 30-50 km (Bilham and England, 2001). Bilham and England (2001) calculated that the 1897 Great Assam earthquake rupture extended to a depth of at least 35 km and possibly

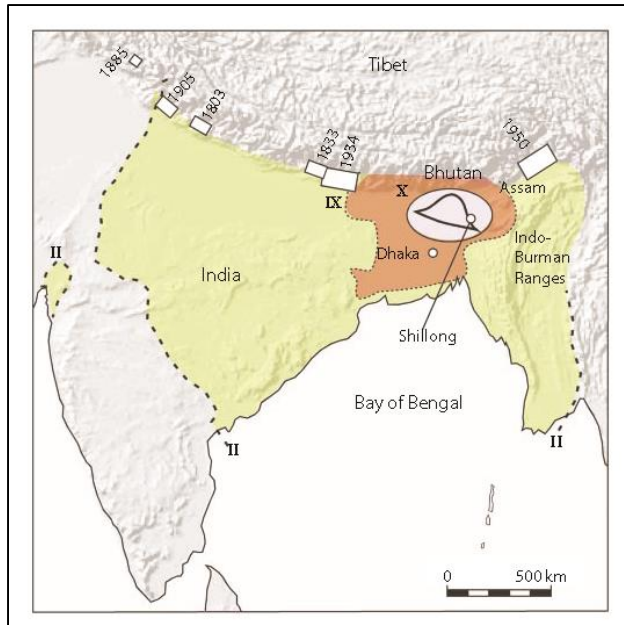


Figure 2.6: Area affected by the 1897 Great Assam earthquake. All buildings within the orange-colored region were damaged, whereas those within the ellipse were destroyed. The earthquake was felt within the green-colored region (Bilham and England, 2001).

penetrated the entire crust, the base of which lies at a depth of 43-46 km at the location of the earthquake. However, the depth of the Moho boundary varies greatly in the surrounding area (Biswas et al., 2007) (Figure 2.4). The 1897 Great Assam earthquake caused the northern edge of the Shillong Plateau to rise by an estimated 11 m and resulted in serious widespread

structural damage to buildings in the region (Figure 2.6). Bilham and England (2001) modeled the $M_w \sim 8.1$ earthquake as occurring along a slip plane at a depth between 9-45 km along the south-dipping Oldham fault, with a net slip of 16 m. They inferred that the slip occurred with a rake of 76° making the Oldham fault oblique with sinistral-reverse displacement. Bilham and England (2001) estimated a recurrence interval for earthquakes of similar magnitude to that of the 1897 event at approximately 3,000 to 8,000 years.

2.4. PLATE CONVERGENCE AND HIMALAYAN CONTRACTION RATES

The rate of Indian plate convergence with Eurasia was not constant before nor after collision, and has slowed continually since collision (Molnar and Stock, 2009; Clark, 2012). The rate of convergence has been slower in western and northwestern India (Molnar and Stock, 2009) (Figure 2.7). Specifically, northeastern India experienced a ~30% drop in convergence rate from 118 to 83 mm/yr at ~40-45 Ma (Molnar and Stock, 2009). Northwestern India experienced a ~45% drop in convergence rate from 109 to 59 mm/yr during the same period. Both northeastern and northwestern India experienced a ~45% drop in

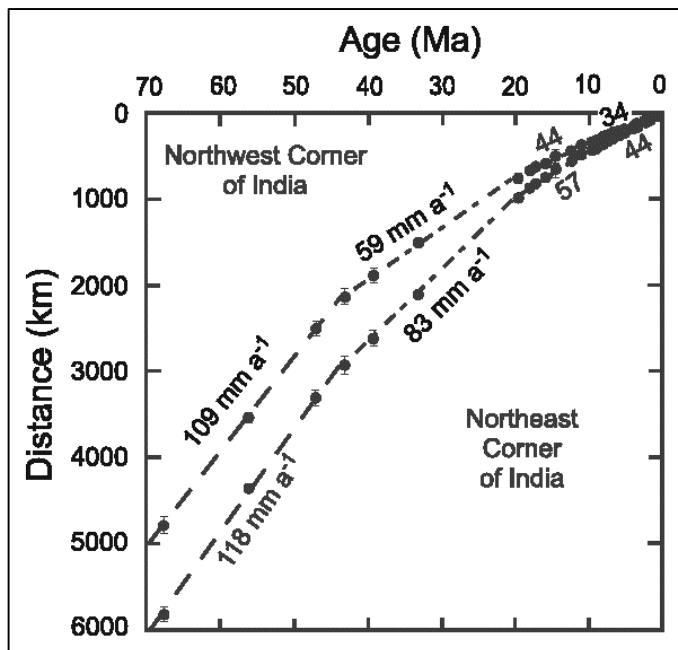


Figure 2.7: Average convergence rates between northwest and northeast India with Eurasia over time. The graph shows average convergence rates during different time intervals and a progressive slowing of convergence (Molnar and Stock, 2009).

convergence rate from 59 to 34 and 83 to 44 mm/yr, respectively, between 10 and 20 Ma (Molnar and Stock, 2009) (Figure 2.7). This second phase of decreased convergence rate may have occurred gradually or in steps, but is assumed to have occurred due to increased growth and elevation of the Tibetan Plateau

which began approximately 20 Ma (Molnar and Stock, 2009). In contrast, Clark (2012) suggested that the decrease in convergence was exponential but progressive, rather than stepwise as suggested by Molnar and Stock (2009).

The greater decrease in convergence rate in northwestern India is due to the angle of collision that affected the existing counter-clockwise convergence path. Initially the Indian sub-continent converged upon Eurasia at an angle such that the

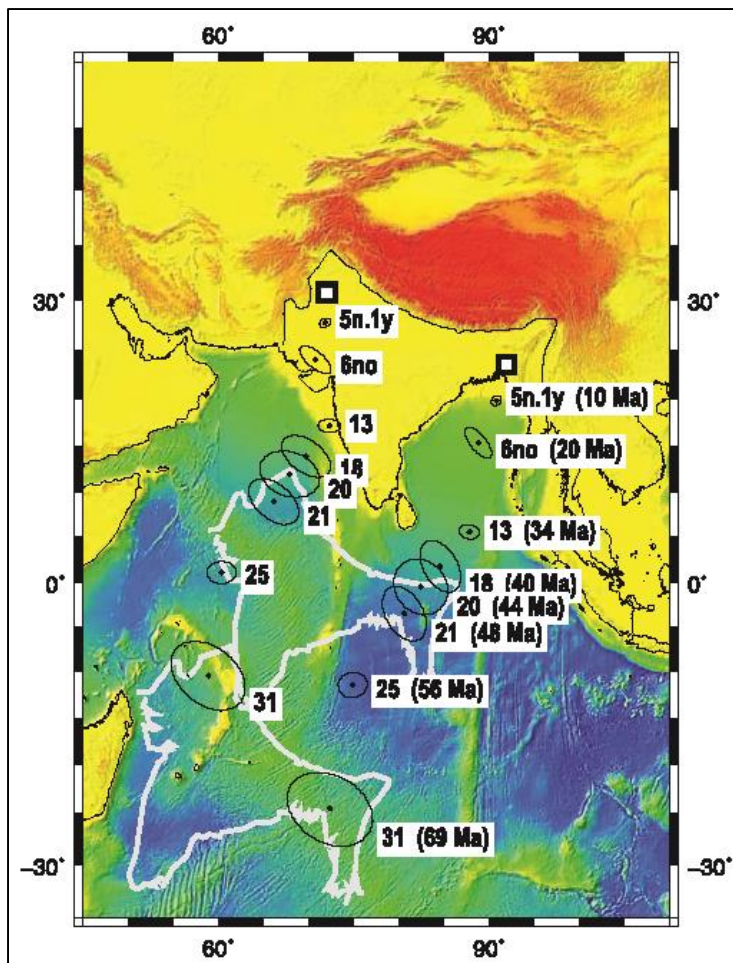


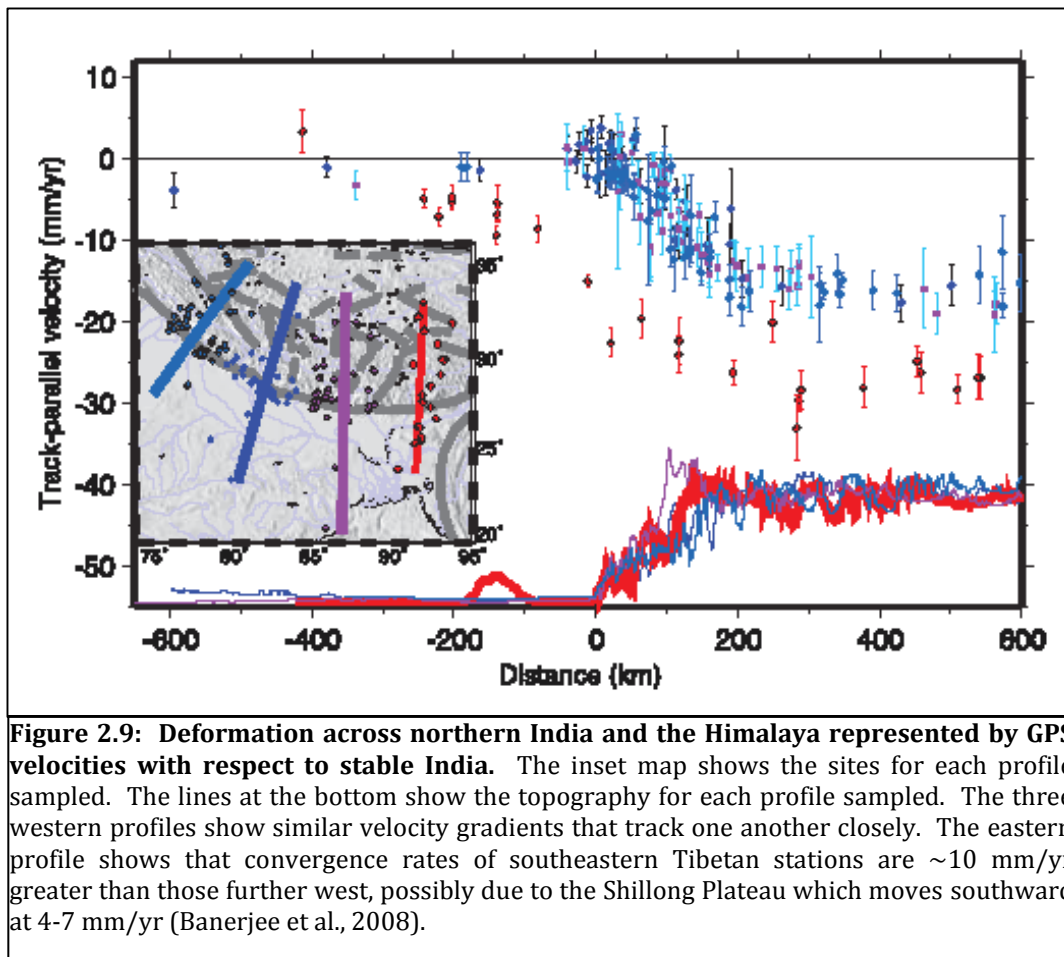
Figure 2.8: Map showing the reconstructed position of two points on the Indian plate with respect to Eurasia at different times. The present position of the points (white squares) is reconstructed to the black dots with 95% uncertainty ellipses. The outline of the Indian plate shows its position at 47 and 68 Ma (Molnar and Stock, 2009).

northwestern corner of India made first contact, thereby resulting in decreased convergence (Figure 2.8). Currently, the convergence rate between southern and northern India is ~2 mm/yr (Banerjee et al., 2008) and GPS measurements have shown that there is approximately 2-4 mm/yr of convergence

between the northern and southern edge of the Shillong Plateau (Jade et al.,

2007). Convergence between the Indian and Eurasian Plates is partitioned into contraction throughout the Himalayas, Tibetan Plateau, and Shillong Plateau.

Present-day contraction between India and Tibet across the Greater Himalaya from northwestern India to eastern Nepal was estimated at approximately 17 mm/yr, whereas, contraction across the easternmost Himalaya is most rapid with rates varying between 15-20 mm/yr (Banerjee et al., 2008) (Figure 2.9). Banerjee et al. (2008) showed that contraction across the Bhutan Himalaya is on the order of 2 cm/yr. GPS measurements have shown that convergence in Bhutan is



directed northeast-southwest (Drukpa et al., 2006). Furthermore, south-directed movements of 4-7 mm/yr of the Shillong Plateau with respect to stable India

indicate contraction across its southern edge (Banerjee et al., 2008) (Figure 2.9). Banerjee et al. (2008) calculated a slip rate of approximately 11 mm/yr for an optimally oriented Dauki fault model.

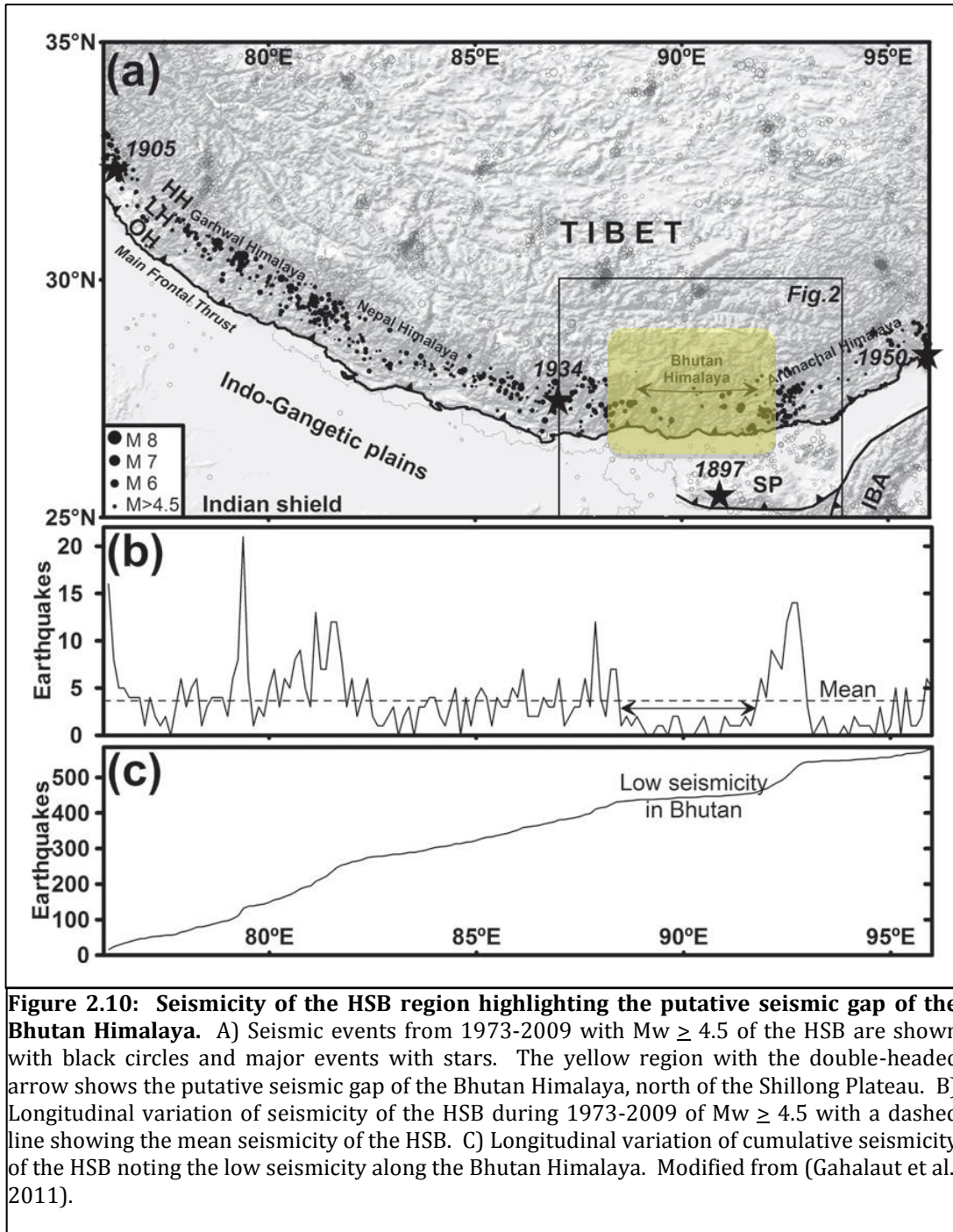
Together, these rates show that partitioning of convergence between India and Eurasia into the Shillong Plateau and MFT in Bhutan Himalaya is balanced by an increased net convergence rate between India and southern Tibet (Molnar and Stock, 2009) and eastward increase of contraction across the Himalaya (Banerjee et al., 2008; Burgess et al., 2012). In other words, the Bhutan Himalaya is not undergoing less contraction than other segments of the Himalaya, but rather the same amount or more (Figure 2.9).

2.5. HIMALAYAN SEISMIC BELT AND SEISMIC GAPS

The majority of seismic events within the Himalayan-Tibetan orogen occur along the Himalayan Seismic Belt (HSB), which is ca. 150 km north of the surface trace of the MFT (Cattin and Avouac, 2000; Avouac, 2004) (Figure 2.10). Seismic events occur along the MHT, where the overriding Himalayan rocks thrust over the Indian basement rocks (Gahalaut et al., 2011). The MHT is seismically active beneath the Outer and Lesser Himalayas where displacement occurs in a stick-slip manner as a result of elastic strain (Gahalaut et al., 2011). However, further north in the region of the Higher and Tethys Himalayas the MHT is aseismic (Gahalaut et al., 2011) because contraction results in ductile deformation such as folding and thickening, but may also include slow aseismic slip known as creep (Bilham and Ambraseys, 2004). Therefore, the down-dip edge of the seismogenic detachment is where small to moderate earthquakes are localized, whereas major earthquakes occur along the detachment under the Outer and Lesser Himalayas (Gahalaut et al., 2011).

Within the HSB, some regions are less active than others and are referred to as seismic gaps (Figure 2.10). Bilham (2004) noted that almost two-thirds of the Himalaya have not been disturbed by recent earthquakes and that no major earthquake has occurred for 53 years in relation to the date of publication. This suggests the possibility that many seismic gaps are currently present throughout the region. The lack of significant seismicity over the past 200 years in the Bhutan Himalaya north of the Shillong Plateau is evidence for one such seismic gap (Gahalaut et al., 2011). During this period no major or great earthquake has

occurred in the region. Furthermore, the absence of a well-documented seismic history has made it impossible to determine a proper recurrence interval for earthquakes along the Himalayan arc, especially for areas that have experienced major historic seismic events (Bilham and Ambraseys, 2004).



Bilham and Ambraseys (2004) re-evaluated earthquake magnitudes since 1500 to derive the convergence rate between India and Tibet. They found that the derived rate (~ 5 mm/yr) was less than one-third of the observed GPS measurement

of 18 mm/yr. They concluded that either the Himalayas are overdue for at least four $M_w > 8$ earthquakes, or plate convergence is being accommodated for in other ways. They noted that aseismic processes may account for a large fraction of plate convergence and that moderate earthquakes may also release substantial amounts of plate boundary slip. Furthermore, there is the possibility that great earthquakes are not essential features of plate-boundary slip and that plate convergence can be accommodated through smaller seismic events. Hence seismic gaps may not be zones of inactivity, but rather they may represent activity in ways that do not necessarily involve stick-slip displacement.

2.6. OPEN GEOLOGICAL QUESTIONS - SEISMIC HAZARDS IN THE EASTERN HIMALAYA

South of the Bhutan Himalaya, the Shillong Plateau was the location of the 1897 Great Assam earthquake. Gahalaut et al. (2011) proposed that the earthquake resulted in static stress change that produced a stress shadow, which overlies part of Bhutan Himalaya (Figure 2.11) and is therefore a possible cause of the putative seismic gap. It is a plausible reason for the low seismicity of the Bhutan Himalaya, which is more than four times less than the mean seismicity of the HSB (Gahalaut et

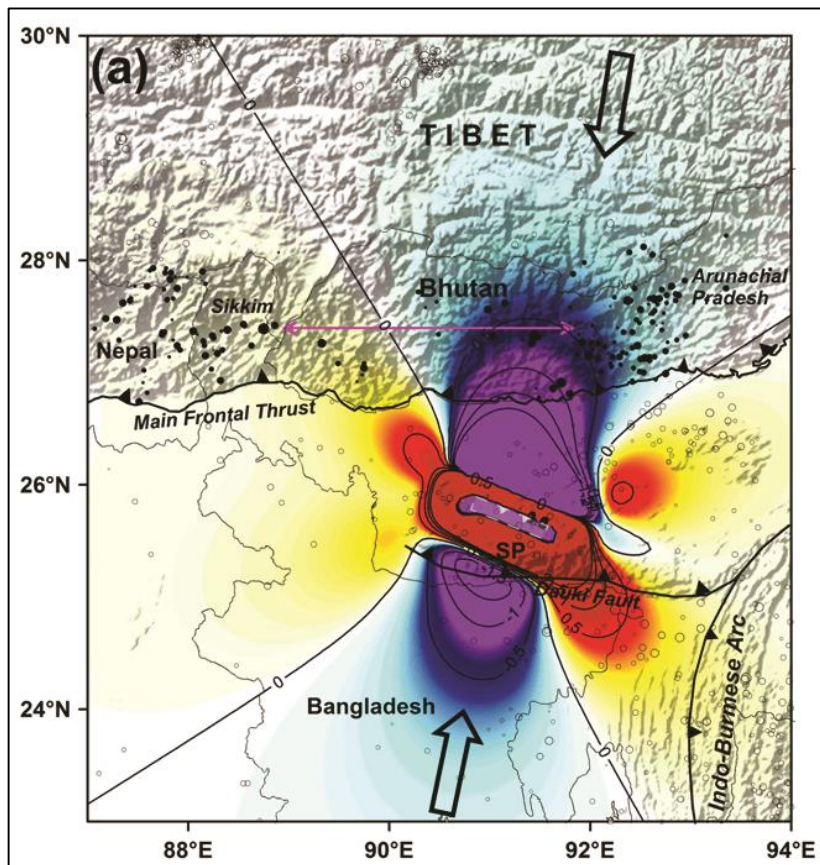


Figure 2.11: Figure 4A from Gahalaut et al. (2011) showing their model results. Gahalaut et al. (2011) showed that static stress change as a result of the 1897 Great Assam earthquake resulted in the formation of a stress shadow that coincides with part of the putative seismic gap of the Bhutan Himalaya. Arrows show the direction of maximum principal stress (Gahalaut et al., 2011).

al., 2011).

Additional factors must be considered however. Strike-slip faulting may have a potential effect on seismicity in the Bhutan Himalaya (Drukpa et al., 2006). Velasco et al. (2007) showed that strike-

slip faulting near the Shillong Plateau and Bhutan Himalaya is

contributing to brittle deformation in the crust under southern Bhutan. Similarly to the west of Bhutan, the Indian state Sikkim is dominated by strike-slip faulting (De and Kayal, 2003; De and Kayal, 2004). Furthermore Gahalaut et al. (2011) only investigated stress change as a result of slip along the Oldham fault, but did not take into account the stress change imparted to major faults in the region, several of them being fairly seismically active (Bhattacharya et al., 2008; Kayal et al., 2012).

I will attempt to determine what effect the 1897 Great Assam earthquake had on stress levels along major active faults in the Shillong Plateau and Bhutan Himalaya, and how potential strike-slip faulting is contributing to the current stress load field in the surrounding area. Key questions that I will investigate are the following: 1) What effect did the 1897 Great Assam earthquake have on stress loading in the Bhutan Himalaya? 2) Was a stress shadow created as a result of the large earthquake? 3) Where is stress being transferred and what effect does nearby strike-slip faulting (Gish, Kopili, Lingshi, Sakteng, and Tista) have on the current stress load? 4) Is the putative seismic gap of the Bhutan Himalaya caused by a stress shadow or is the gap due to partitioning of stresses into strike-slip faults? 5) Where are likely seismic events going to occur in the future and at what time interval will they occur?

3.0 METHODOLOGY

For my research I utilized the principals of Coulomb stress transfer and its application to studies of seismic hazards. I used various rates of convergence, shortening, and fault-block movement and applied them in a variety of stress-transfer scenarios using numerical modeling. In my research I used a methodology approach similar to that of Lin and Stein (2004), who investigated stress triggering for thrust and subduction earthquakes along the southern San Andreas fault. The program I used for modeling is Coulomb 3.3 (Lin and Stein, 2004; Toda et al., 2005), a graphic-rich deformation and stress-change software. In the following section I explain the principles of the Coulomb fracture criterion and how I will specifically use the theory of stress transfer for my research and analysis. Next, I outline and explain Coulomb stress change as it applies to various types of seismic events. Lastly, I describe and summarize the modeling program, Coulomb 3.3, and explain parameters I used in my model.

3.1 COULOMB FRACTURE CRITERION

The theory of Coulomb stress transfer is a fundamental aspect of seismotectonics. Faults and joints result from brittle deformation and form through fracturing whereby there is an instantaneous loss of cohesion or renewed slip along a pre-existing plane (Fossen, 2010). These structures form in areas where effective differential stress has built up to a level that exceeds the rupture strength of the host rock. Similarly, existing fractures may be reactivated under conditions where the effective differential stress has reached the conditions for frictional sliding. The theory of the Coulomb fracture criterion predicts the state of stress at which a host rock under compression is critically stressed, or at the verge of failure (Fossen, 2010). Therefore, the criterion predicts the critical state of stress required for a shear fracture to form in the compressive regime.

The Coulomb fracture criterion is one of three fracture criteria used to describe the full range of possible stress states in the Mohr failure envelope, which describes critical states of stress over a range of differential stress (Fossen, 2010). The Coulomb fracture criterion predicts the critical stress condition at which a shear fracture will form, whereas the Griffith fracture criterion and Von Mises criterion predict stress conditions for tensile fractures and ductile deformation respectively (Fossen, 2010). The Coulomb fracture criterion takes into consideration the critical shear stress (σ_s) and normal stress (σ_n) acting on a potential fracture plane in the rock at the moment of failure (Figure 3.1). The two stress components are related to one another by the constant $\tan\phi$, where ϕ is the angle of internal friction. Their

relation is expressed by: $\sigma_s = \sigma_n \tan \phi$, where $\tan \phi$ is commonly referred to as the coefficient of internal friction (μ). μ has a value between 0.47-0.7 for rocks, but generally a value of 0.6 is used for calculations (Fossen, 2010).

The angle between σ_1 and the fracture ($90^\circ - \theta$) is related to the orientation of the fracture, which is expressed in terms of the angle of internal friction (ϕ) and the orientation of the fracture (θ) by the following: $\theta = 45^\circ + \phi/2$ (Fossen, 2010). Therefore, if $\mu \approx 0.6$ most rocks have $\phi \approx 30^\circ$, which implies that the angle between σ_1 and the fracture is approximately 30° . The constant C represents the internal or

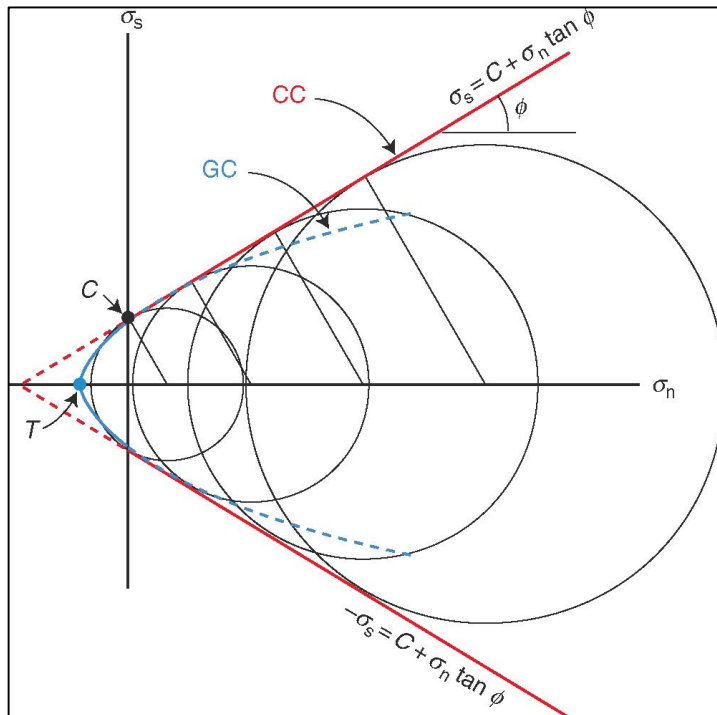


Figure 3.1: The Coulomb fracture criterion is shown as two red lines in the Mohr diagram. The blue line represents the Griffith criterion. Mohr circles represent examples of critical states of stress. The cohesive strength (C) and tensile strength (T) of the rock are also shown (Fossen, 2010).

cohesive strength of the rock and the value of critical shear stress across a surface where $\sigma_n=0$. Therefore, the complete Coulomb fracture criterion is expressed by the equation: $\sigma_s = C + \sigma_n \tan \phi = C + \sigma_n \mu$ (Fossen, 2010) (Figure

3.1).

A reaction to stress will depend on the level of stress or amount of accumulated elastic strain, but also depends on factors such as anisotropy, temperature, strain rate, pore fluid pressure,

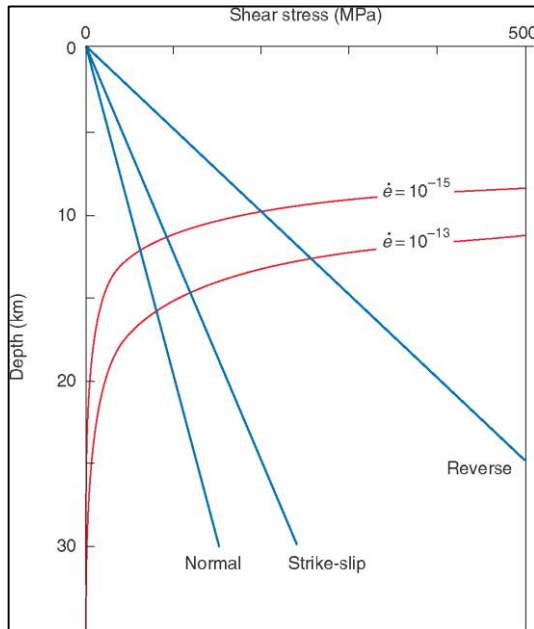


Figure 3.2: Strength vs. Depth. Shear resistance increases with depth through brittle crust until the temperature is high enough to activate plastic flow. The intersection of brittle (blue) and plastic (red) strength profiles defines the brittle-plastic transition. The three different stress regimes shown in blue represent the different stress level required for each (Fossen, 2010).

and confining pressure (Fossen, 2010). In the brittle or frictional regime, a rock under stress accumulates elastic strain before it fractures at a critical stress level. If the stress is removed prior to fracturing then the elastic strain will disappear, as it is recoverable in nature. However, for a rock under constant temperature and pressure the potential for fracturing depends on the differential stress and mean stress (Fossen, 2010). Differential stress is the difference between the largest and smallest principal stresses, $\sigma_D = (\sigma_1 -$

$\sigma_3)$, and the mean stress is the average of the principal stresses, $\sigma_M = (\sigma_1 + \sigma_2 + \sigma_3/3)$ (Fossen, 2010). Fracturing requires a differential stress that exceeds the rupture strength of the local host rock. In turn, the strength of a rock depends on the confining pressure or depth of burial, whereby strength is lowest near the surface and increases with depth (Figure 3.2). Therefore, with an increase

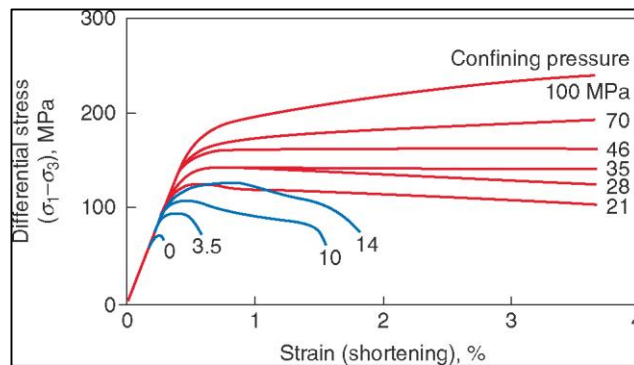


Figure 3.3: Stress-strain curves for a range of confining pressures. Increasing levels of confining pressure increase the differential stress that the rock can sustain before failure (blue curves). Above a critical confining pressure the rock retains its strength as it deforms plastically (red curves) (Fossen, 2010).

in confining pressure there is an increase in differential stress for fracturing to occur (Figure 3.3).

The Coulomb fracture criterion predicts the state of stress required for failure and only applies up until failure occurs within the rock (Fossen, 2010). Once failure occurs and a fracture has formed, a plane of weakness is present that may be reactivated by renewed stress build-up over time. This is because at low confining

pressure lower levels of stress are required to reactivate existing fractures than to form new ones from natural microscopic pores, cracks, and flaws within the rock known as Griffith cracks (Fossen, 2010) (Figure 3.4). The

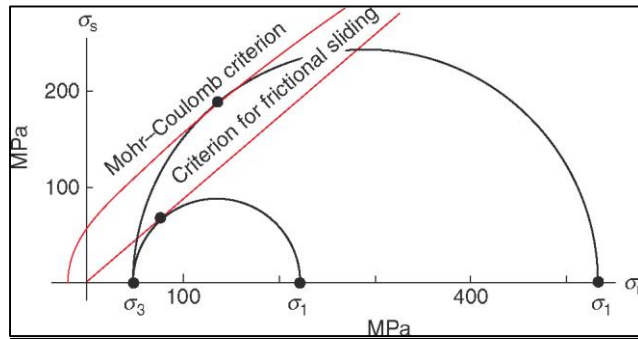


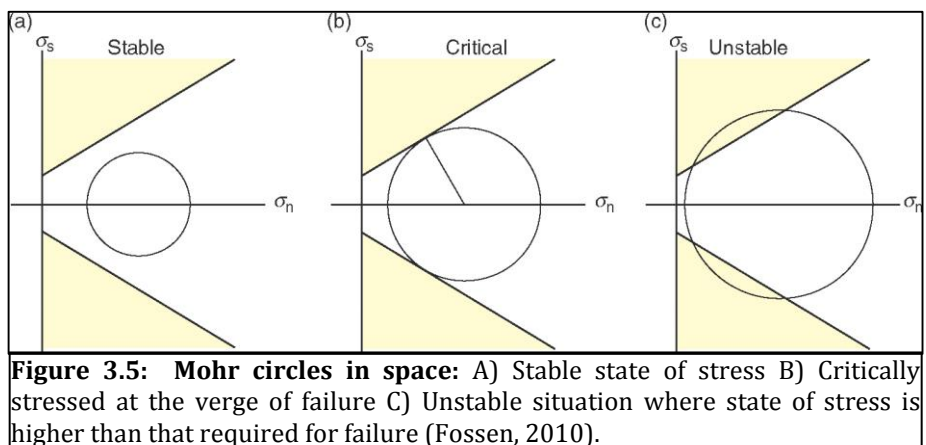
Figure 3.4: Reactivation of a preexisting fracture in the Mohr diagram. The criterion for frictional sliding shows that a much smaller differential stress is required to reactivate a preexisting fracture than is required to generate a new fracture in a rock according to the Mohr-Coulomb criterion (Fossen, 2010).

reactivation of existing fractures is a prerequisite for major faults or faults with significant displacement to develop whereby the orientation of the fracture, its coefficient of sliding friction (μ_f), and existing stress field are the most important parameters for reactivation to occur (Fossen, 2010).

The orientation of the fracture will determine the resolved normal and shear stresses on its surface. If the combination of resolved normal and shear stress on a preexisting fault does not lie on the criterion for frictional sliding the fracture is stable (Figure 3.4). μ_f is the limiting constraint on fracture reactivation, whereby

friction is equal to the shear stress required to activate slip divided by the normal stress acting across the fracture ($\mu_f = \sigma_s/\sigma_n$). At moderate to high levels of confining pressure μ_f is similar for most rocks, whereas at low confining pressure it may vary due to surface roughness along the fracture or fault asperities that can hinder reactivation (Fossen, 2010). However, faults with large cumulative slip (transform faults, subduction zones), faults lubricated by hot gasses and fluids, and creeping faults with significant gouge development tend to have low values of μ_f in the range of 0.0 to 0.3 (Ross Stein; personal comm. 2014). Young faults and reactivated faults such as many continental thrust and normal faults tend to have higher values in the range of 0.5 to 0.8 (Ross Stein; personal comm. 2014).

In the Mohr diagram the Coulomb fracture criterion is represented by two straight lines known as the Coulomb failure envelope (Figure 3.1). If a Mohr circle does not touch the envelope then it represents a stable state of stress, but if it is touching the envelope then it represents a critical state of stress and a material on the verge of failure (Fossen, 2010) (Figure 3.5). Following this, the Mohr failure

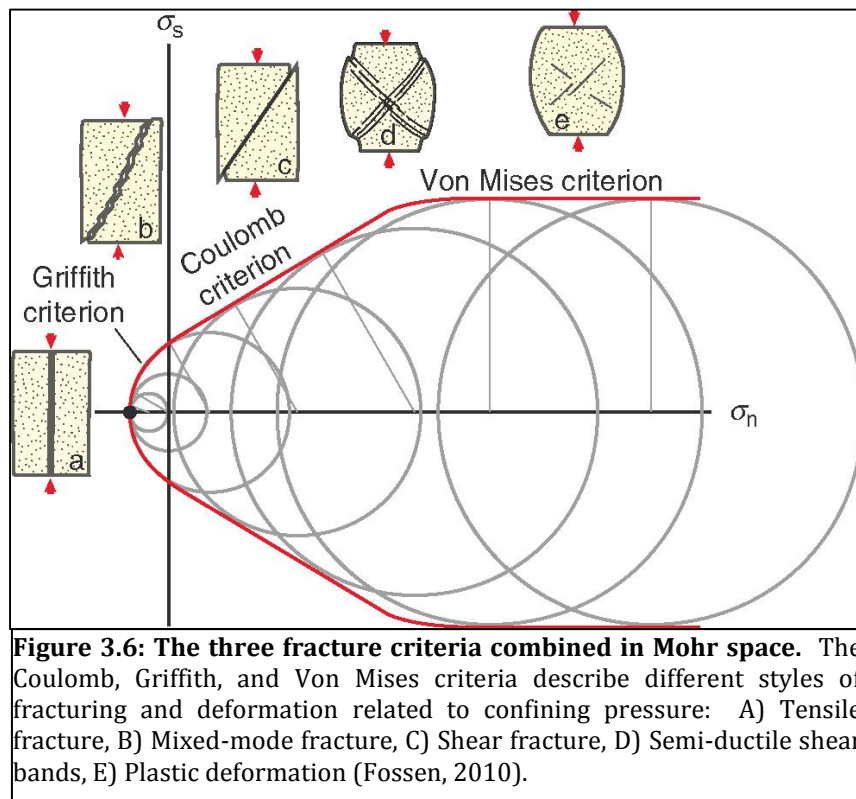


envelope describes critical states of stress over a range of differential

stress. At low confining and negative stresses the envelope curves and becomes

parabolic representing the Griffith fracture criterion in the tensile field, whereas at high confining pressure it becomes horizontal representing plastic deformation according to the Von Mises criterion (Fossen, 2010) (Figure 3.6). The Griffith fracture criterion is represented in the Mohr diagram by a parabola where its intersection with the abscissa is defined by T , the critical tensile strength (Fossen, 2010). The constant T represents the stress at which tensile fractures start to form and the value of critical normal stress across a surface where $\sigma_s=0$ (Figure 3.1).

Each rock type has its own physical properties, and in turn their own failure envelopes have been determined through laboratory experiments. The different makeup of rocks and various stress load environments make it impossible for one criterion, or envelope, to correctly predict the stress regime in which different types of failure will occur (Figure 3.6).



3.2 COULOMB STRESS CHANGE AND TRANSFER

The theory of Coulomb stress change can be used to determine the interaction between faults, seismic events, and how failure occurs in a given rock. The main criterion (or condition) used in stress change is that of the Coulomb fracture criterion, which requires that “both shear and normal stress on an incipient plane satisfy conditions analogous to those of friction on a preexisting surface” (King et al., 1994). The criterion predicts that failure will occur along a plane when the Coulomb stress (σ_f) exceeds a specific value (King et al., 1994). There is no specific threshold value, but rather the larger the ΔCFF the greater the probability of triggering a seismic event. A ΔCFF of 0.1 bar has been shown to cause significant changes to seismicity rates, while in the rare case a ΔCFF of 0.01 bar has been shown to register a seismicity response (Ross Stein; personal comm. 2014).

The Coulomb fracture criterion is two-dimensional, whereby the intermediate stress (σ_2) does not play a role (King et al., 1994). Coulomb stress change may be defined as $\Delta CFF = \Delta\sigma_s + \mu\Delta\sigma_n$ where ΔCFF is the change in the Coulomb failure function, $\Delta\sigma_s$ is the change in shear stress (positive in the slip direction), $\Delta\sigma_n$ is the change in normal stress (positive when the fault is unclamped), and μ is the apparent friction coefficient after accounting for the pore fluid pressure effect (Lin and Stein, 2004). The term unclamped means the stress acting to keep the two faces of a fault in contact has been reduced, while clamped means the stress increased (Ross Stein; personal comm. 2014).

The pattern of stress transfer does not vary greatly with depth in strike-slip faults, and as such they are well understood in predicting the distribution of off-fault stress changes (Lin and Stein, 2004). Figure 3.7 displays features common to all stress-change scenarios in strike-slip faults. The figure displays the shear, normal,

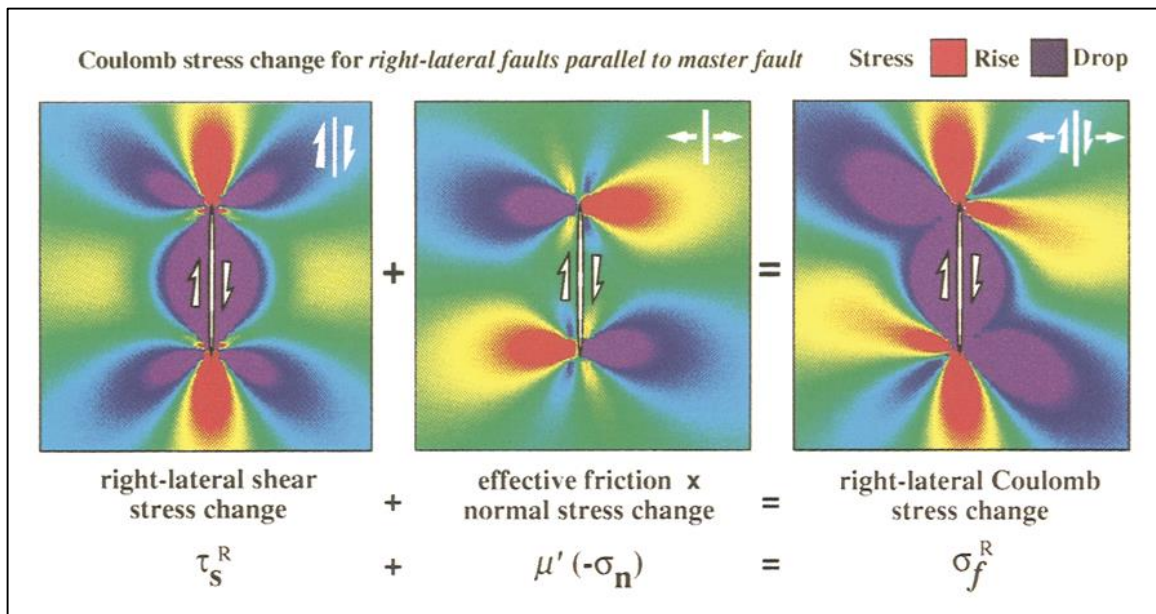


Figure 3.7: Coulomb stress change for specified right-lateral faults parallel to a right-lateral source fault embedded in elastic half-space. Coulomb stress changes are depicted with graded colors: blue represents a decrease, red represents an increase, and green represents no change. The contributions of the shear and normal components to the failure condition, and the resulting Coulomb stress change, are shown in separate panels. The calculation represents the change in Coulomb stress on specified right-lateral fault planes as a result of slip along the right-lateral source fault (King et al., 1994).

and Coulomb stress change on infinitesimal specified receiver faults parallel to a right-lateral source fault. Shear stress is increased at the source fault tips, while it is decreased along the source fault and along oblique fault-tips (Figure 3.7). In turn, this increases the tendency for along-fault failure at the fault tips. The shear stress pattern is symmetrical in Figure 3.7 due to the fact that regional stress is not taken into account. Normal stress change lobes are perpendicular to the source fault and asymmetrically distributed such that lobes of stress increase and decrease are on

opposite sides and ends of the source fault. Hence, normal stress change increase and decrease fields are anti-symmetrically distributed across the source fault (Figure 3.7), thereby increasing the tendency for off-fault failure (King et al., 1994). When shear and normal stress-change components are added together the final Coulomb stress change is produced (Figure 3.7).

Figure 3.8 displays the shear, normal, and Coulomb stress change for optimally oriented receiver faults associated with a right-lateral source fault in a 007° regional compressive stress of 100 bar. The shear stress change shows a

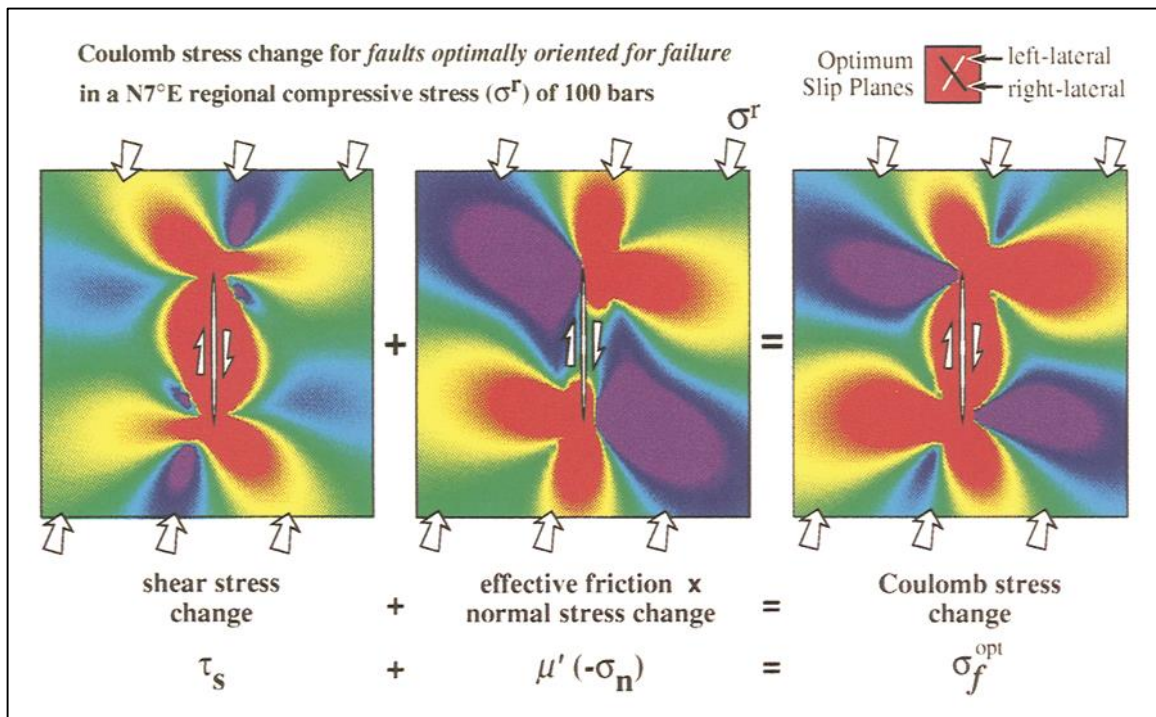


Figure 3.8: Coulomb stress change for optimally oriented left- and right-lateral faults in a 007° regional compressive stress of 100 bar with a right-lateral source fault embedded in elastic half-space. Slip along the source fault is the same as in Figure 3.7. Coulomb stress changes are depicted with graded colors: blue represents a decrease, red represents an increase, and green represents no change. White lines indicate optimal left-lateral orientations, while black lines indicate optimal right-lateral orientations. The contributions of the shear and normal components to the failure condition, and the resulting Coulomb stress change, are shown in separate panels. The optimal orientations are calculated from the total stress after the earthquake, and the Coulomb stress changes caused by the earthquake stress changes are resolved onto these planes (King et al., 1994).

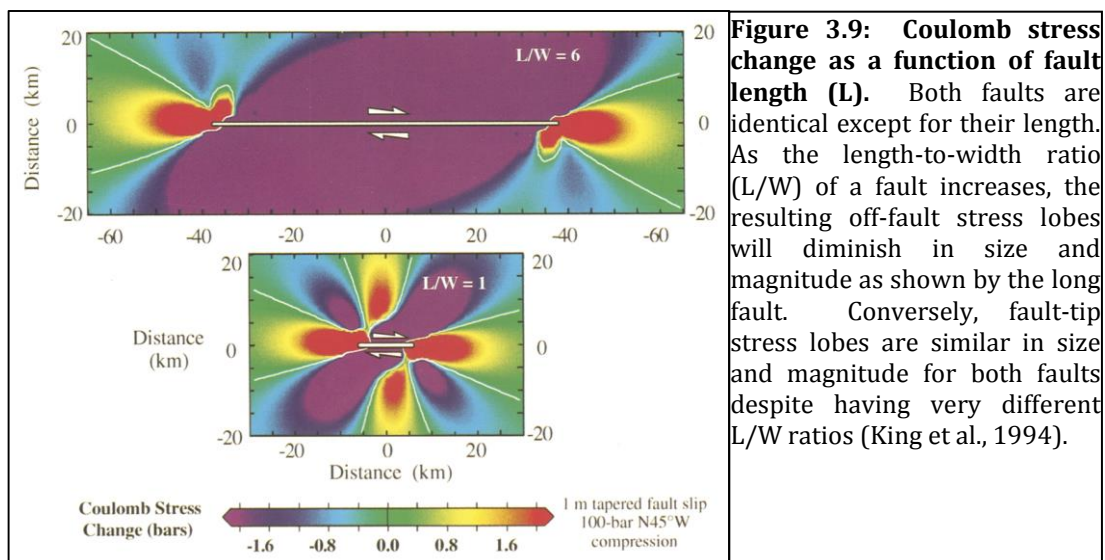
similar pattern as in Figure 3.7, except that stress increases along the fault as well as

at the fault tip. The stress-increase lobes at the fault tips are not parallel to the source fault as in Figure 3.7, but are oblique to it. There are also stress-decrease lobes located off the fault tip that are oblique to the source fault. The pattern of shear stress change for Figure 3.8 is anti-symmetric. The normal stress change in Figure 3.8 is asymmetric as in Figure 3.7 and similar in pattern. However, the alignment of stress-decrease lobes is oblique to the source fault as opposed to Figure 3.7, where lobe alignment is perpendicular. This is due to the influence of regional stress. The lobes of stress increase are perpendicular to the source fault as in Figure 3.7, but there are additional stress-increase lobes parallel to the fault tips. Therefore, the normal stress change increase and decrease fields are distributed anti-symmetrically in Figure 3.8. When combined, the Coulomb stress change for Figure 3.8 shows an overlapping between the shear and normal stress changes. The Coulomb stress change is similar to Figure 3.7 except that there is an increase in stress along the fault as opposed to a decrease, and the oblique fault-tip stress-increase lobes are much larger for Figure 3.8. Lobes of normal and Coulomb stress are larger in Figure 3.8 due to the influence of regional stress and the associated orientation of principal stress axes.

Specifically, because Figure 3.8 is an example of Coulomb stress change resolved on optimally oriented receiver faults, the ΔCFF will be larger than the ΔCFF on specified receiver faults at every point. This is because at every point the plane is found on which ΔCFF is optimized (most positive). Both situations show a Coulomb stress-change pattern that is anti-symmetric. Lastly, all Coulomb stress-change

patterns for strike-slip source faults show four lobes of Coulomb stress increase and four lobes of Coulomb stress decrease (King et al., 1994) (Figures 3.7/3.8).

These two examples are two-dimensional because the x- and y-axes are horizontal, as is the fault displacement, while the fault planes are vertical. However, for three-dimensional cases dip-slip and strike-slip components exist, whereby the relative magnitude of horizontal to vertical stresses determines the nature of the seismic event (King et al., 1994). It is the ratio of vertical to horizontal stresses that determines whether strike-slip or dip-slip faulting occurs. Furthermore, where two principal stresses are roughly equal, the resulting distribution of Coulomb stress change for strike-slip and dip-slip faulting is similar (King et al., 1994). Coulomb stress change takes into account the length of the fault, whereby the length-to-width ratio (L/W) has profound impacts on seismicity. Given two faults with the same width, depth, and seismic slip, the shorter the fault the greater the size and magnitude of the oblique off-fault stress lobes (King et al., 1994) (Figure 3.9). Off-fault stress lobes will diminish in size and magnitude with increasing fault length. However, fault-tip stress lobes will remain fairly similar in size and magnitude regardless of fault length (Figure 3.9).



Dip-slip faulting is more complicated than strike-slip faulting as stress transfer varies considerably with depth and unlike most strike-slip faults, dip-slip faults are often blind (Lin and Stein, 2004). Seismic events that occur along surface-cutting thrust faults relieve stress over a large area along their cross-sectional area on both sides of the fault (Lin and Stein, 2004). This results in a drop in Coulomb stress, which inhibits failure along nearby fault planes. In this situation the stress drop occurs along the fault plane above and below it on both fault blocks, but there is an increase in Coulomb stress at the bottom down-dip tip of the fault along both fault blocks as well (Figure 3.10A). Conversely, seismic events along blind thrust faults will increase stress over a large area thereby increasing the chance of failure along nearby fault planes. This results in the potential for blind thrusts to initiate off-fault seismicity (Lin and Stein, 2004). In this situation stress drops along the fault plane on both sides, but is increased at the upper and lower tips of the fault plane on both fault blocks (Figure 3.10B). Furthermore, if there is a secondary surface-cutting fault above a blind thrust fault, the Coulomb stress increase along the upper tip of the blind fault may be relieved by the surface-cutting secondary fault in an aftershock (Figure 3.10C)

Stress change that results from thrust faulting is further transferred along strike, but the resulting distribution of Coulomb stress increase beyond the tips of the fault is not strongly influenced by the nature of the source fault (whether it is blind or surface-cutting) (Figure 3.10D-F). Fault-tip stress lobes are similar in size and magnitude in faults with the same width, slip, and depth despite the fact their lengths may be substantially different (Figure 3.9). Lastly, the size and magnitude of

Coulomb stress increase and decrease is dependent on the fault geometry, amount of seismic slip, and regional stress in the case of optimally oriented receiver faults.

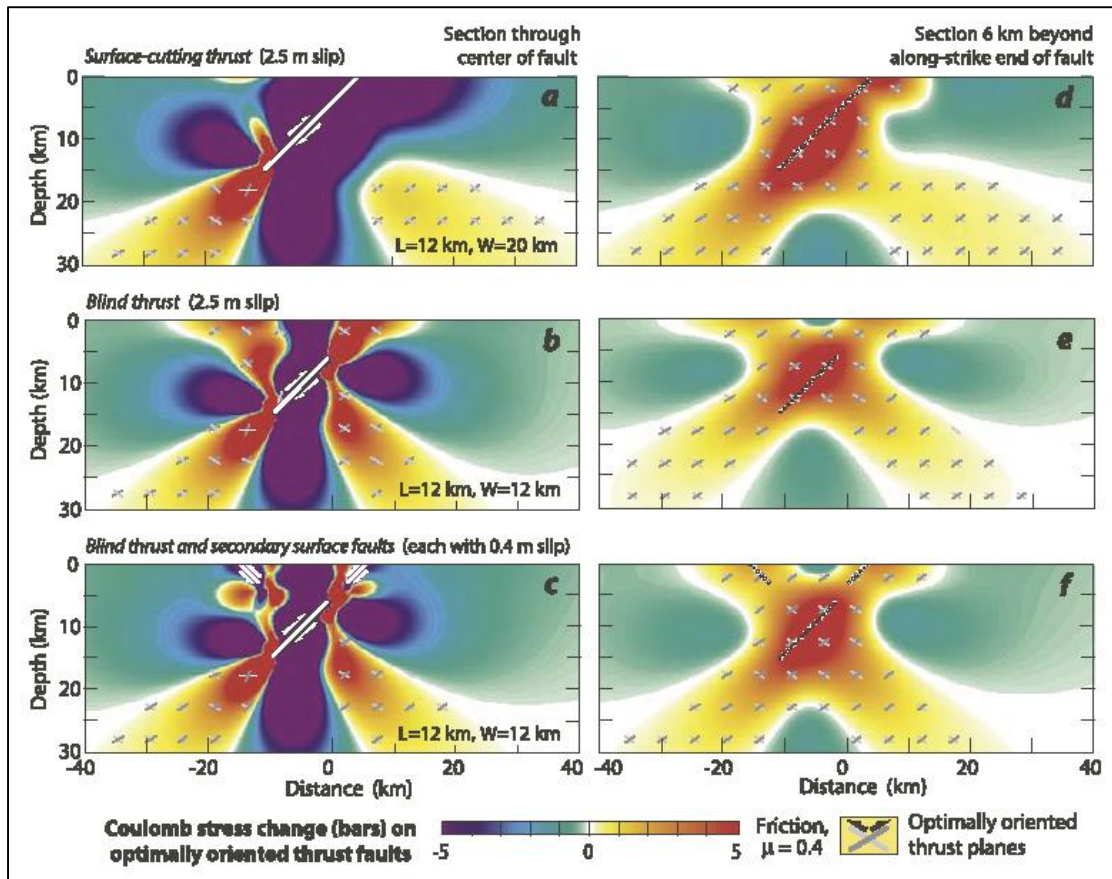


Figure 3.10: Cross sections through thrust faults at different orientations showing the resulting Coulomb stress change pattern on optimally oriented thrust faults as a result of slip along the source thrust fault: A) Surface-cutting thrust fault decreases stress in the upper crust, B) Blind thrust fault increases stress in the upper crust, C) Near-surface stress increase due to a blind thrust fault may be relieved by secondary surface faulting, D-F) Distribution of Coulomb stress at fault tips is relatively insensitive to the nature of the thrust fault (whether it is surface-cutting or blind (Lin and Stein, 2004).

The slip zone of large thrust earthquakes ($M \geq 7$) tend to become longer along strike than they are wide down-dip due to the finite depth of brittle-elastic crust thereby increasing their L/W ratio, which in turn has profound effects on seismicity and stress change (Lin and Stein, 2004). One effect of this is that the Coulomb stress-drop perpendicular to strike becomes much larger, while the Coulomb stress

increase at the fault tips tends to stay fairly constant regardless of the L/W ratio (Figure 3.9). However, stress transfer to adjacent areas is also affected. Faults with lower L/W ratios transfer stress to a greater area of the adjacent patch along fault tips than faults with larger L/W ratios. It follows that thrust faults with low L/W ratios are more effective at triggering aftershock earthquakes along strike. Conversely, the zone of decreased Coulomb stress, or stress shadow, is much larger for faults with large L/W ratios due to the broad perpendicular Coulomb stress decrease along strike. Therefore, thrust faults with large L/W ratios are more effective at inhibiting aftershock earthquakes in the region perpendicular to strike. Lastly, the pattern of Coulomb stress change imparted to strike-slip receiver faults varies drastically depending on the L/W ratio of the source thrust fault (Figure 3.11C-D), whereas the Coulomb stress change imparted to reverse receiver faults is less variable and not as affected by the L/W ratio of the source thrust fault (Figure 3.11A-B).

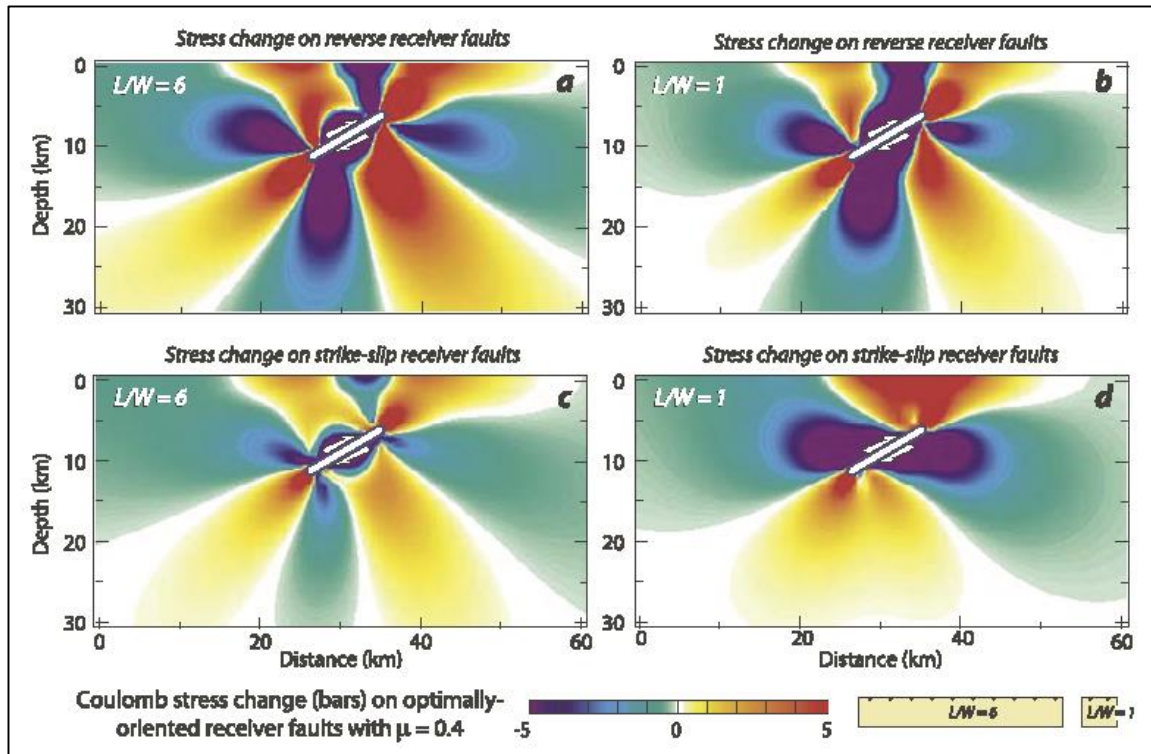


Figure 3.11: Cross-sections along the midpoint of a 30°-dipping blind source thrust fault showing the resulting Coulomb stress change imparted to optimally oriented (A,B) reverse and (C,D) strike-slip receiver faults. The Coulomb stress change pattern on optimally oriented reverse faults is similar regardless if the source fault has a large (A) or small (B) L/W ratio. Conversely, the resulting Coulomb stress change pattern on optimally oriented strike-slip faults is very different depending on whether the source fault has a large (C) or small (D) L/W ratio (Lin and Stein, 2004).

3.3 COULOMB 3.3

Coulomb 3.3 is a graphic-rich, deformation and stress-change software I used for numerical modeling in order to determine the stress change regime in the study area. In Coulomb 3.3, there are four methods of resolving the Coulomb stress change on receiver faults due to nearby seismic events along source faults. The first method involves resolving Coulomb stress change on particular planes with a defined geometry, known as specified receiver faults (Figure 3.7). These faults have a defined strike, dip, and rake (slip direction along the fault plane) (Figure 3.12). The second method is used to determine the correspondence between earthquake stress change and resulting aftershocks. This is done using optimally oriented receiver faults, in which the plane with the greatest Coulomb stress increase at every point in space is found (Figure 3.8). Optimally oriented receiver faults can be selected so as to reflect thrust, normal, or strike-slip receiver faults. With this method the regional stress is taken into account while regional stress is not taken into account using specified receiver faults. The other two methods are receiver faults with geometry set in the input file, and focal mechanism files that always have two orthogonal fault planes.

Receiver faults are specified with their strike, dip, and rake, and stresses are imparted to them by source faults with defined geometry that have a slip component. The normal and shear stress components of Coulomb stress change are resolved onto receiver fault planes. The shear-stress component is dependent on the position, geometry, and slip of the source fault and on the position and geometry of the receiver fault, while the normal stress component is independent of the

receiver fault rake. Fault rake is determined according to the Aki and Richards (1980) convention (Figure 3.12). This convention defines the following parameters: $0^\circ \leq \text{STRIKE} < 360^\circ$, $0^\circ < \text{DIP} \leq 90^\circ$, and $-180^\circ \leq \text{RAKE} \leq 180^\circ$. Strike and dip are

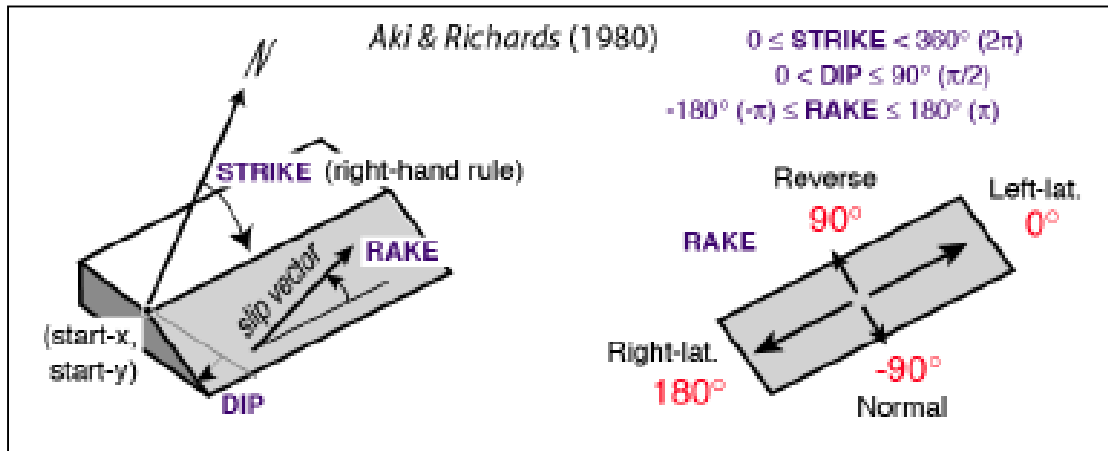


Figure 3.12: Aki and Richards 1980 convention for resolving stress and focal mechanisms. Fault geometry and kinematics in Coulomb 3.3 is set according to this convention (Lin et al., 2011).

determined according to the right-hand rule whereby a 0° rake parallel to strike corresponds to pure left-lateral slip. Conversely, a 180° or -180° rake is the opposite orientation and corresponds to pure right-lateral slip. A rake of 90° corresponds to pure reverse slip, while -90° corresponds to pure normal slip. All other rake values correspond to oblique-slip displacement with dip-slip and lateral-slip components. It is important to note that all rake values are set in reference to the displacement and movement of the hanging-wall fault block.

The Coulomb failure criterion is used and defined as $\Delta\sigma_f = \Delta\sigma_s + \mu' \Delta\sigma_n$, where $\Delta\sigma_f$ is the change in failure stress on the receiver fault caused by slip on the source fault, $\Delta\sigma_s$ is the change in shear stress, $\Delta\sigma_n$ is the change in normal stress, and μ' is the effective coefficient of friction along the fault. The change in shear stress is considered positive when shear occurs in the direction of the fault slip, while change

in normal stress is positive if the fault is unclamped. Failure along a receiver fault is promoted when the Coulomb stress change is positive. Conversely, failure along a receiver fault is hindered when the Coulomb stress change is negative.

The Coulomb stress change function calculates shear stress and normal stress and then combines them to display the overall Coulomb stress change. The resulting image is effectively the Coulomb stress drop and increase, as a result of slip along a source fault. The Coulomb stress change pattern shown in map view and cross-section view displays this Coulomb stress drop and increase. In all cases receiver faults have no slip. A receiver fault is not taken into account when the function is run regardless of whether it is present in the grid of the input file. The function takes into consideration only receiver faults in the four available methods of resolving Coulomb stress. When using optimally oriented receiver faults, four options are available to the user: optimally oriented strike-slip, normal, thrust, and faults. This last option, optimally-oriented faults, is a slow search over the entire focal sphere for receiver planes at every grid point. When using the “Specified faults” option the user manually enters fault geometry parameters, which are then used by the function. It is very important to understand that a user-made receiver fault within the grid of the input file is separate from optimally oriented and specified receiver faults used to calculate the Coulomb stress change, which are only within the function when it is calculated.

There are two types of input file in Coulomb 3.3 that allow the user to model a variety of stress-change scenarios. The first type is an .inp file, which allows the user to model source faults and their slip. The second type is an .inr file, which

allows the user to model both source faults with slip and receiver faults with resulting stress change. Both types of input file require basic fault parameter information such as their geographic location, length, width, depth, strike, dip, and magnitude (only for source faults with slip). However, different parameters are used to define their fault geometry. All faults in Coulomb 3.3 use the Aki and Richards (1980) convention for fault geometry and slip (Figure 3.12), but it is applied differently depending on what type of input file is being used. .inp input files can only model source faults and their slip component is defined by setting the numerical amount of lateral slip and dip slip. Conversely, .inr input files can model both source faults and receivers faults and their geometry is defined by setting the individual rake for each fault. For source faults the user also sets a net slip value. The rake value gives the fault its kinematics (i.e. normal, reverse, thrust, strike slip, or oblique), and the net slip is partitioned accordingly into both lateral and dip-slip components according to the rake. For receiver faults with no slip the rake defines the kinematics of the fault, and therefore the type of displacement that would occur along its plane. This is very useful because the user can model stress change on faults according to their individual rake in the grid of an input file. This option is not available using .inp input files.

However, despite the fact that rake is not assigned the Aki and Richards (1980) convention still applies to .inp files with regard to fault geometry and the type of fault displacement. For example, the user can create a rake of 45° for .inp source faults, but would have to set the correct amount of dip-slip and lateral-slip components in order to achieve such a rake. It is very important to note that when

creating a fault in Coulomb 3.3 the starting point that is set is the reference point for determining its orientation. This is such that when looking across the strike of the fault from the starting point towards the finishing point, the hanging wall will always be on the right side. This is crucial in creating a properly designed fault.

Input files are first made without setting a specific type (.inr/.inp). The user first defines the study area, or geographic grid, using either Cartesian coordinates (x , y , z) or latitude and longitude. If using latitude and longitude the user also sets a (0,0) reference point. Once the grid has been set, the user is free to add as many faults as desired. Faults must be laid out before the input file parameters are set, unless using the "Trace and put faults into input" option, which is only available after the input file has been built. Once the file has been built and the user is satisfied with their fault layout they may begin running various stress and strain functions. Furthermore, they can also change regional stress values as they so choose in order to run specific functions. Furthermore, fault parameters may be changed within the input file after they have been made if needed. All input file parameters can also be viewed and changed using text readers, such as Text Editor. This allows the user to manually change the encryption coding for any input file.

A variety of functions and calculations can be run using Coulomb 3.3 including those pertaining to stress, strain/deformation, earthquake locations and overlays, and magmatic sources. For my research I only utilized functions and calculations related to stress, specifically "Coulomb stress change," "Calc. stress on faults," and "Calc. stress at a point." The "Coulomb stress change" function was used to determine the pattern of Coulomb stress change as a result of slip along the

Oldham fault. This function provides the Coulomb stress increase and decrease pattern as a result of slip along the source fault. The “Calc. stress on faults” function was used to determine the Coulomb stress change imparted to receiver faults by the source fault according to their individual rake. The “Calc. stress at a point” function was used to precisely determine the Coulomb stress change at any point along a fault. The “Coulomb stress change” and “Calc. stress at a point” functions utilize regional stress values, whereas the “Calc. stress on faults” function does not.

In my model I utilized optimally oriented receiver faults when calculating the Coulomb stress change. This method is based on the assumption that a sufficient number of faults with various orientations exist and that those optimally oriented for failure will be most likely to fail as a result of slip along a source fault (King et al., 1994). Optimal orientation is a function of both stress change due to slip on the source fault and pre-existing regional stress. In Coulomb 3.3, Coulomb stress change for optimally oriented receiver faults is calculated after the earthquake whereby the optimum orientations are calculated from the total stress after the seismic event (King et al., 1994). The Coulomb stress change caused by stress changes associated with the seismic event are resolved onto optimally oriented planes.

The optimal orientation of receiver faults is determined by the regional stress, but this may not be the case close to the source fault because the magnitude of Coulomb stress change caused by the seismic event may be comparable to the regional stress (King et al., 1994) (Figure 3.13). The determining factor in this case is the ratio between earthquake stress drop ($\Delta\tau$), and the regional stress (σ^r). If the

two are roughly equal, and the earthquake relieves all of the regional stress, then the optimal planes rotate near the source fault (King et al., 1994) (Figure 3.13). In

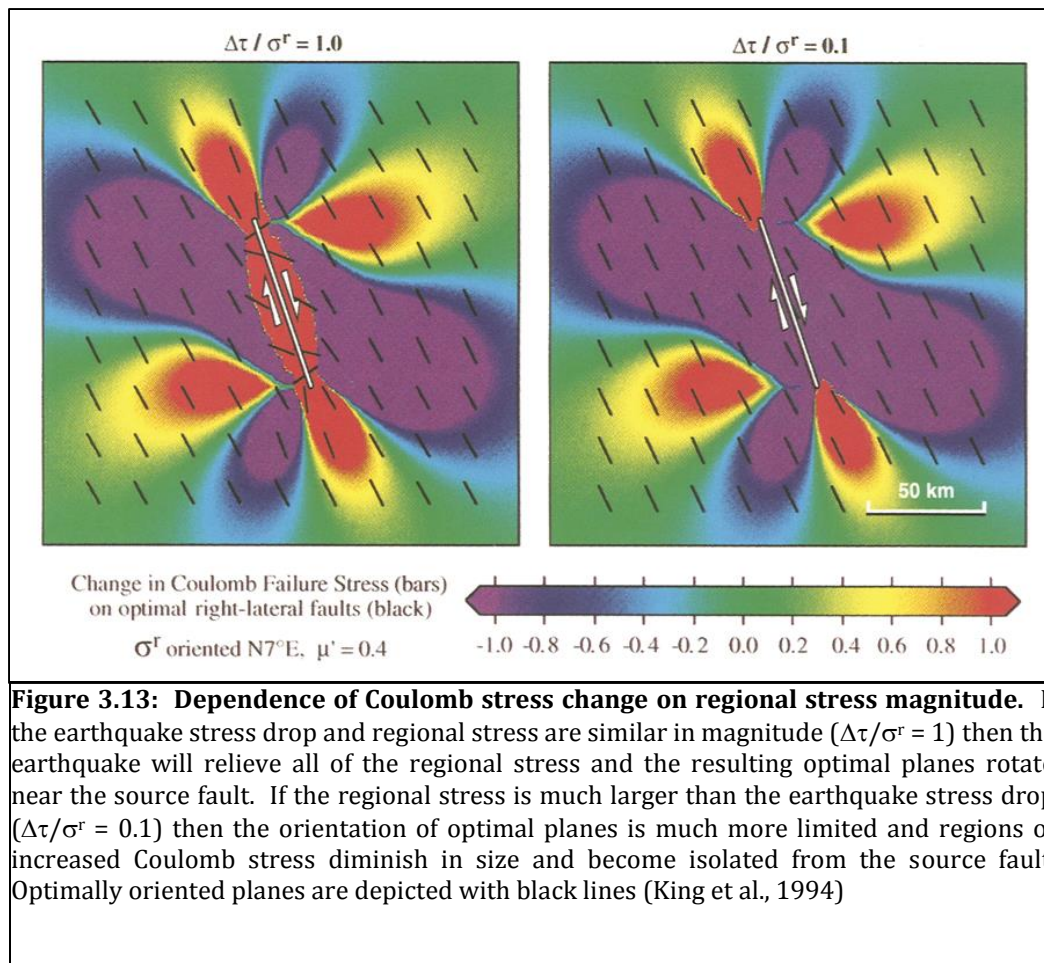


Figure 3.13: Dependence of Coulomb stress change on regional stress magnitude. If the earthquake stress drop and regional stress are similar in magnitude ($\Delta\tau/\sigma^r = 1$) then the earthquake will relieve all of the regional stress and the resulting optimal planes rotate near the source fault. If the regional stress is much larger than the earthquake stress drop ($\Delta\tau/\sigma^r = 0.1$) then the orientation of optimal planes is much more limited and regions of increased Coulomb stress diminish in size and become isolated from the source fault. Optimally oriented planes are depicted with black lines (King et al., 1994)

this case, Coulomb stress increases along the source fault. If the regional stress is much larger than the earthquake stress drop, then the optimal planes are limited in orientation and are more or less the same throughout the region (King et al., 1994) (Figure 3.13). In this case, regions of increased Coulomb stress diminish in size and become isolated away from the source fault.

Given a fixed source fault geometry and slip, the orientation of the regional stress field has the biggest effect on the size of Coulomb stress-change lobes, while changes to the coefficient of effective friction control the influence of normal stress

change on failure (King et al., 1994) (Figure 3.14). Only the deviatoric part of regional stress determines the orientation of principal stress axes, therefore regional stress can be applied as a single uniaxial compression or extension in Coulomb 3.3 (King et al., 1994).

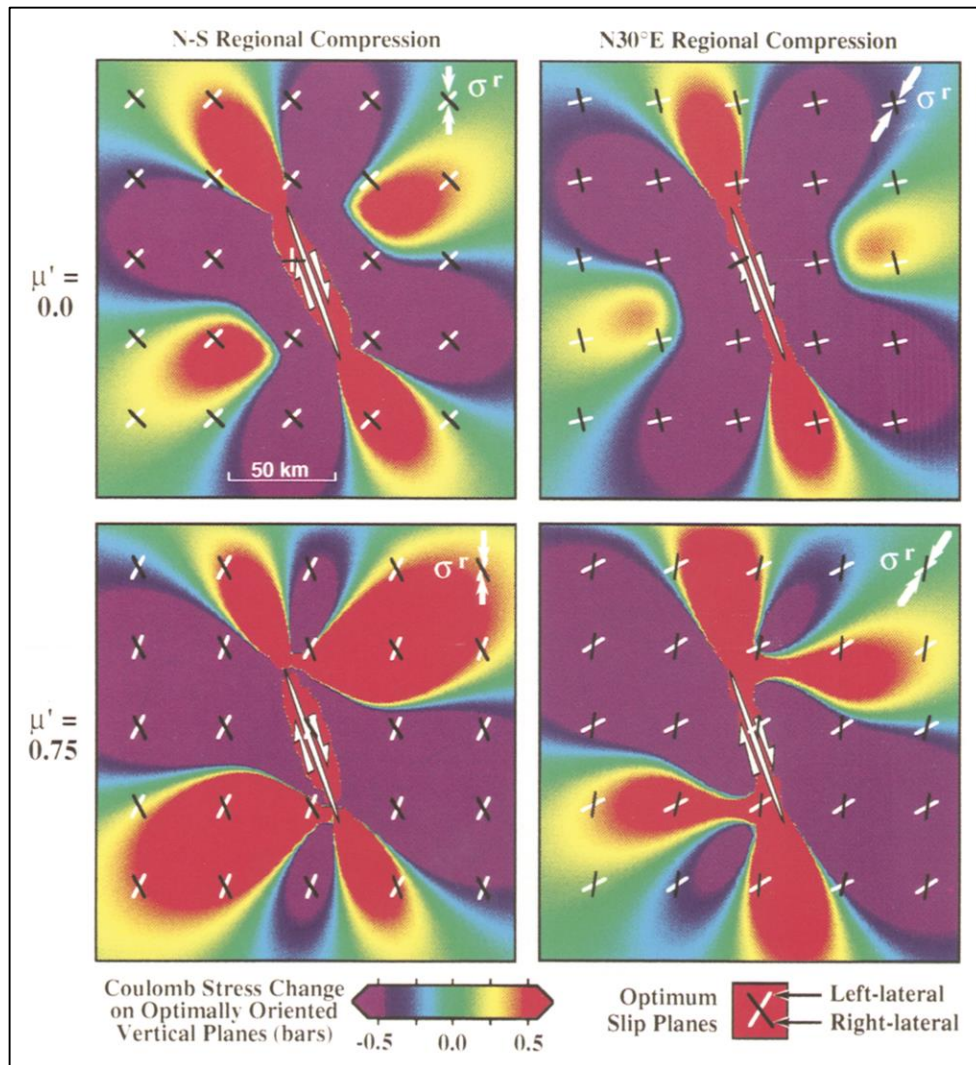


Figure 3.14: The effect of changing the regional stress orientation (Left vs Right) and the effective coefficient of friction (Top vs Bottom). The regional stress orientation controls the size of off-fault to fault-end stress lobes. Conversely, friction controls the internal angle between right- and left-lateral slip planes and the influence of normal stress change on failure (King et al., 1994).

3.4 MODEL FORMULATIONS AND PARAMETERS

I used Coulomb 3.3 for numerical modeling of Coulomb stress change that resulted from the 1897 Great Assam earthquake. The model included one source fault, which represented the Oldham fault along which the earthquake occurred. I modeled the resulting Coulomb stress change on eight separate receiver faults. They are the following: Dauki, Gish, Kopili, Lingshi, MFT (frontal ramp), MFT (basal detachment), Sakteng, and Tista (Figure 5.1). For my model I only utilized .inr input files in order to better represent the rake of the faults. This was especially important for receiver faults as their individual rakes were used in the “Calc. stress on faults” function, from which I gathered the most significant data.

The first step was to determine the study area, and therefore the geographic coordinates of the input file grid. I chose to use the geographic boundaries of Figure 4A from Gahalaut et al. (2011) as the study area for several reasons (Figure 2.11). First, I chose to replicate their Coulomb stress change study as a starting point for my own research and to familiarize myself with the software. Gahalaut et al. (2011) also investigated Coulomb stress change that resulted from the 1897 Great Assam earthquake and therefore their results were a useful source of comparison for my own. Secondly, the geographic boundaries they used contained all of the faults of interest.

The study area grid coordinates are the following: 23°N to 30° N and 87°E to 94°E with a reference point of (26.5°N, 90.5°E). I chose to build the input file from latitude and longitude coordinates, but Coulomb 3.3 automatically calculates the Cartesian grid in kilometers as well. This corresponds to a grid of -348.28 km to

348.28 km from x-start to x-finish and -389.18 km to 389.18 km from y-start to y-finish. After the study area was implemented in the input file, I then built each fault according to the parameters listed in Table 3.1. I obtained fault parameters and regional stress values from literature. Both the study area and faults are created from the “Build input from CMT or focal mech. data” calculator that is accessed by the following command: **Input > Build input file from lon. & lat. map.**

Fault Name	Start X (long)	Start Y (lat)	Finish X (long)	Finish Y (lat)	Length (km)	Width (km)	Strike	Dip	Rake	Depth (km)	Net Slip (m)	Mw
Oldham	90.7462	25.9992	91.7495	25.6218	108	43	113	57	76	9 to 45	16	8.1
Dauki	92.0522	25.1477	90.108	25.1702	193	46	271	50	90	0 to 35	0	0
Lingshi	89.2855	27.7183	89.8272	28.2961	84	45	040	85	-10	5 to 50	0	0
Gish	88.6324	26.9161	88.8722	27.3764	56	45	025	90	-5	5 to 50	0	0
MFT (Frontal Ramp)	93.6304	26.8967	87.9259	26.7184	568	16	268	40	90	0 to 10	0	0
MFT (Basal Detachment)	93.6211	27.0084	87.9166	26.8301	568	100	268	4	90	10 to 17	0	0
Kopili	93.7433	24.7514	91.4723	27.6539	394	45	325	88	-170	5 to 50	0	0
Sakteng	92.1644	27.3869	91.2301	27.032	101	32	247	70	-10	10 to 40	0	0
Tista	89.9772	25.2456	87.9512	27.7411	343	45	324	90	175	5 to 50	0	0

Table 3.1: Fault parameters used for numerical modeling in Coulomb 3.3.

Regional Stress	S1 - Azimuth	S1 - Plunge	S2 - Azimuth	S2 - Plunge	S3 - Azimuth	S3 - Plunge
Tista, Kopili, and Dauki:	10	0	10	-90	100	0
Lingshi, Gish, Sakteng, and MFT:	165	0	165	-90	75	0

Table 3.2: Regional stress values used for optimally oriented receiver fault calculations in Coulomb 3.3.

The first phase of research was to model all faults together in one input file and then run Coulomb stress-change calculations in order to see the resulting Coulomb stress-change pattern. For all Coulomb stress functions I used a friction coefficient of 0.4, the default coefficient for Coulomb stress-change calculations. In Coulomb 3.3 the friction coefficient represents μ_f . All calculations were also run with the same net slip amount of 16 m along the Oldham fault (Bilham and England, 2001). I ran the first Coulomb stress change function with the following command: **Functions > Stress > Coulomb stress change**. I then utilized optimally oriented receiver faults, of which I chose optimal thrusts. I chose to use optimal thrusts because the most important receiver faults were the Dauki fault, a reverse fault that is adjacent to the Oldham fault, and the Main Frontal Thrust (MFT). However, most of the other receiver faults are strike-slip.

The optimally oriented receiver faults option requires regional stress values, of which I used two sets. One set of regional stress values applies to the Dauki, Kopili, and Tista faults, while the other set applies to the Gish, Lingshi, MFT, and Sakteng faults. These values are listed in Table 3.2. I modeled Coulomb stress-change calculations for both sets of regional stress values at depths of 10, 20, 30, and 40 km. In addition to this, I also sampled four cross-sections at the same orientation for each set of regional stress values. Three of the cross-sections were perpendicular to the eastern, western, and central segments of the Oldham fault, while the fourth was oblique to the Oldham and perpendicular to the Kopili faults. These Coulomb stress-change calculations provided me with one pseudo-3D Coulomb stress-change pattern associated with the 1897 Great Assam earthquake.

It also allowed me to determine where the greatest increase and decrease in Coulomb stress occurred in relation to the receiver faults. It is important to note that many patterns of Coulomb stress change are possible depending on the regional stress values used, type of optimal receiver fault chosen, or fault geometry used with respect to specified receiver faults.

The second phase of the model was to investigate individual Coulomb stress change on those receiver faults affected by the source fault. The initial Coulomb stress-change calculation provided one potential Coulomb stress-change pattern, which allowed me to see Coulomb stress change proximal to the receiver faults. Following this I ran a second Coulomb stress-change calculation called “Calc. stress on faults.” This is done with the following command: **Functions > Stress > Calc. stress on faults**. This function allows the user to resolve the stress imparted to receiver faults by a source fault. This function does not use regional stress values regardless of whether they are included in the user’s input file. When the command is run a “Stress on faults control panel” opens, which allows the user to select the stress component that will be resolved on receiver faults. When using .inr input files, the user has the option of selecting the “Coulomb for individual rake” option in the panel, which resolves Coulomb stress on receiver faults according to their individual rake. This is the main reason I chose to use .inr input files so that I could better represent and model the rake of faults and therefore their natural displacement. With this function I was able to see specifically which receiver faults were affected and the magnitude of stress change along their surface.

The “Calc. stress on faults” function was useful for determining general Coulomb stress changes, however I needed to resolve stress imparted to receiver faults more precisely. Therefore, for the third phase of the model I chose those faults that experienced substantial Coulomb stress change and modeled them individually with the source fault. I ran five separate models with individual receiver faults. Those faults were the following: Dauki, Kopili, MFT (frontal ramp), Tista, and Sakteng. Those five faults all experienced a change in Coulomb stress according to the “Calc. stress on faults” calculation.

In order to resolve imparted stress more precisely I split the receiver faults into patches. This is done by right-clicking on them in the grid and selecting the “Splitting” option in the “Element input panel.” This option allows the user to split any fault into any amount of patches by choosing the number of fault divisions along strike and dip. I chose my divisions based on each receiver fault’s length and width in order for the patches to be as close to squares in dimension as possible. The greater the number of patches, the greater the resolution for each receiver fault. Therefore, when running the “Calc. stress on faults” function again for each individual fault, Coulomb 3.3 calculates the Coulomb stress change for each individual patch. This allows the user to precisely determine the Coulomb stress change across the entire receiver fault and where the greatest increase and decrease in Coulomb stress has occurred as a result of slip along a source fault. This permits a much better interpretation of the resulting Coulomb stress-change pattern. The effects of the 1897 Great Assam earthquake on regional seismotectonics were assessed based on Coulomb stress-change calculations on individual receiver faults,

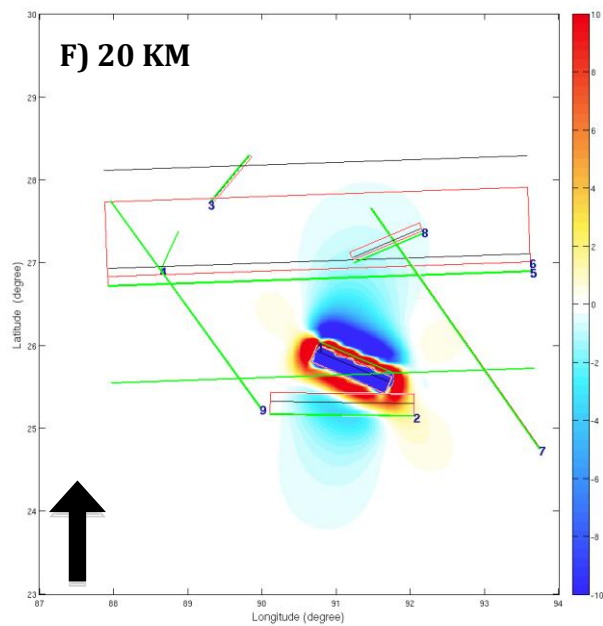
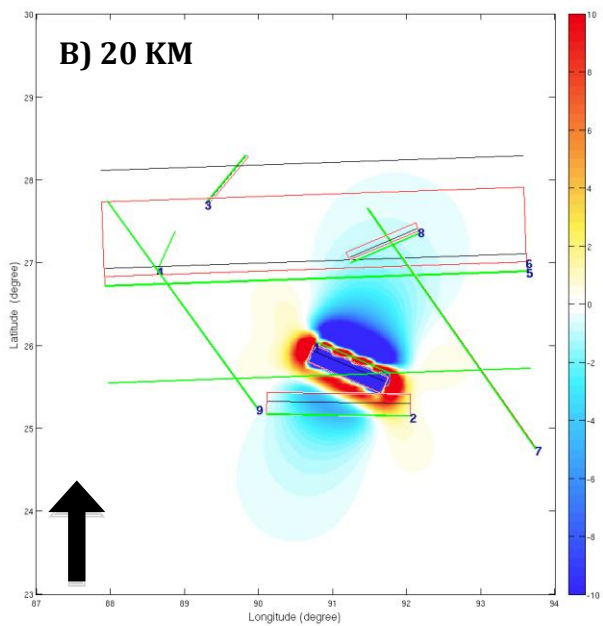
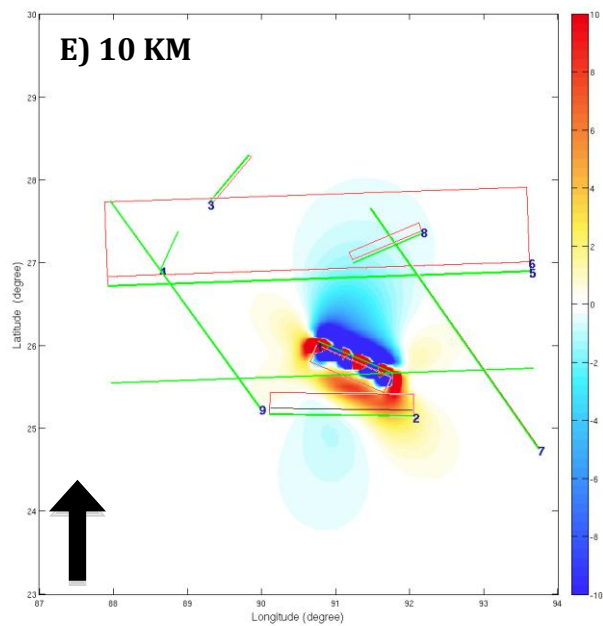
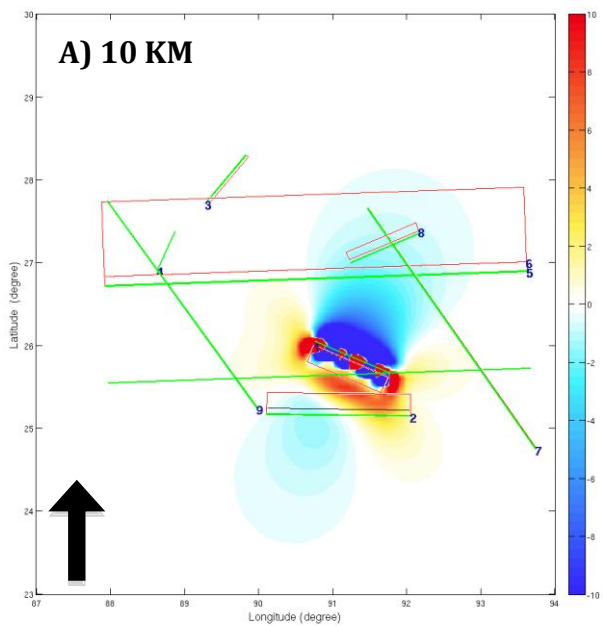
coupled with map view and cross-section optimally oriented Coulomb stress-change calculations.

4.0 RESULTS

This chapter presents results produced from numerical modeling related to Coulomb stress change due to the 1897 Great Assam earthquake. Inference and analysis on Coulomb stress-change calculations is included. Two sets of results are presented in this chapter, and a third in the following. The first set is map view images derived from Coulomb stress-change calculations at various depths using optimally oriented receiver faults. The second set is cross-section images derived from Coulomb stress-change calculations using optimally oriented receiver faults. Both sets of results have been produced from the same Coulomb stress-change function. Both sets of calculations show a similar Coulomb stress-change pattern with a stress decrease along the source fault and accompanying stress increase proximal to the fault.

4.1 MAP VIEW COULOMB STRESS CHANGE PATTERNS

The first set of Coulomb stress-change calculations were modeled using optimally oriented thrust faults. One sub-set of map-view images corresponds to regional stress values for the Dauki, Kopili, and Tista faults, while the other sub-set corresponds to the Gish, Lingshi, MFT, and Sakteng faults.



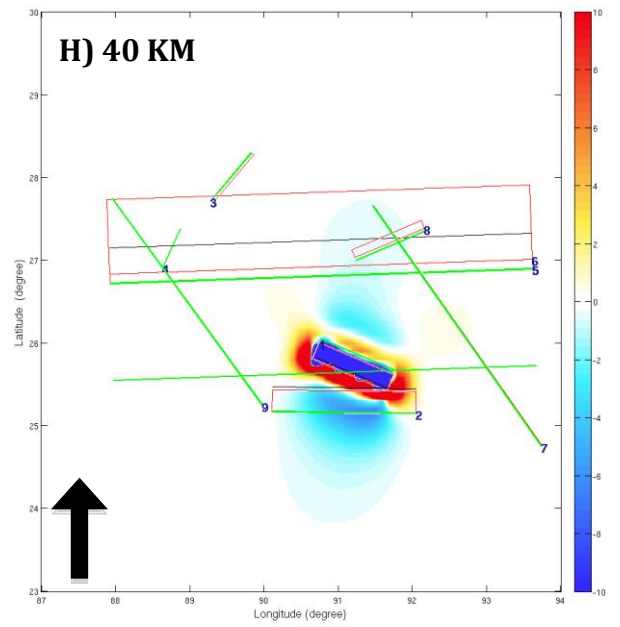
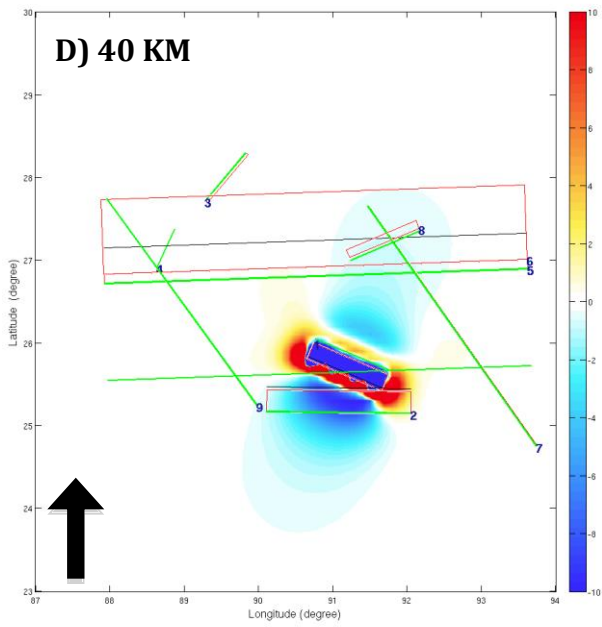
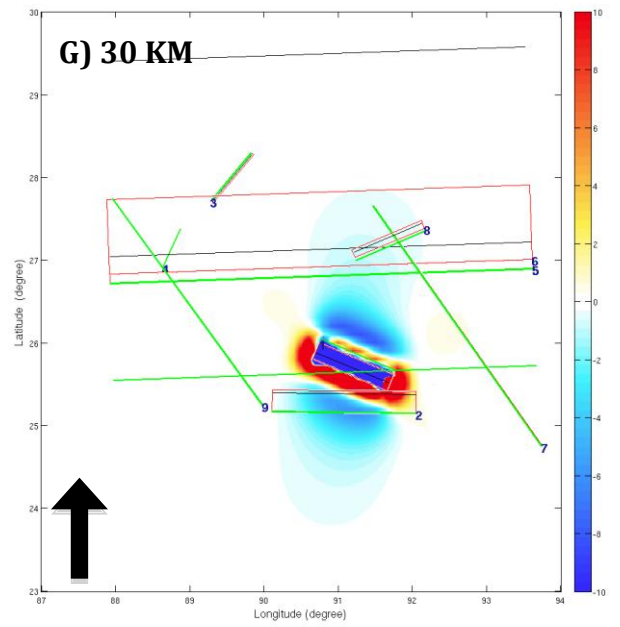
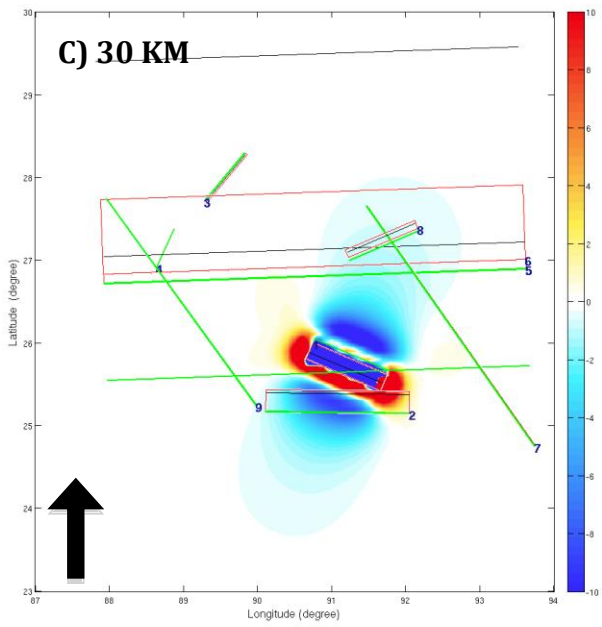


Figure 4.1: Coulomb stress-change pattern in map view. A-D) Coulomb stress-change pattern shown at 10, 20, 30, and 40 km depth intervals corresponding to regional stress values for the Dauki, Kopili, and Tista faults. E-H) Coulomb stress-change pattern shown at 10, 20, 30, and 40 km depth intervals corresponding to regional stress values for the Gish, Lingshi, MFT, and Sakteng faults. Blue-colored regions indicate areas that have experienced a decrease in Coulomb stress. Red-colored regions indicate areas that have experienced an increase in Coulomb stress. White-color regions indicate areas that have experienced no change in Coulomb stress. Fault boundaries are shown with a red-colored outline. The intersection of a fault with the depth interval is shown with a black line. If the sampling depth is at a level in which the fault does not exist, the projected intersection is still displayed, which is a function of the fault's dip. The surface projection of a fault is depicted with a green line. Vertical faults with a 90° dip only appear as a green line because the outline of the fault cannot be seen in map view. All faults are numbered in the following order: 1) Oldham 2) Dauki 3) Lingshi 4) Gish 5) MFT (frontal ramp) 6) MFT (basal detachment) 7) Kopili 8) Sakteng and 9) Tista. For all images the color saturation index is -10 to 10 bar and is depicted with the legend on the right hand side. The grid shown for each image is the entire study grid used in the model, with longitude along the x-axis and latitude along the y-axis. Total distance along the x-axis is ~697 km and ~778 km along the y-axis. The black arrow indicates north for each image.

4.2 CROSS-SECTION COULOMB STRESS CHANGE PATTERNS

This second set of Coulomb stress-change results is the same as obtained in the first set, but is presented in cross-section view. One sub-set of cross-sections corresponds to regional stress values for the Dauki, Kopili, and Tista faults, while the other sub-set corresponds to the Gish, Lingshi, MFT, and Sakteng faults. For both sub-sets the same geographic orientation for cross-sections were used.

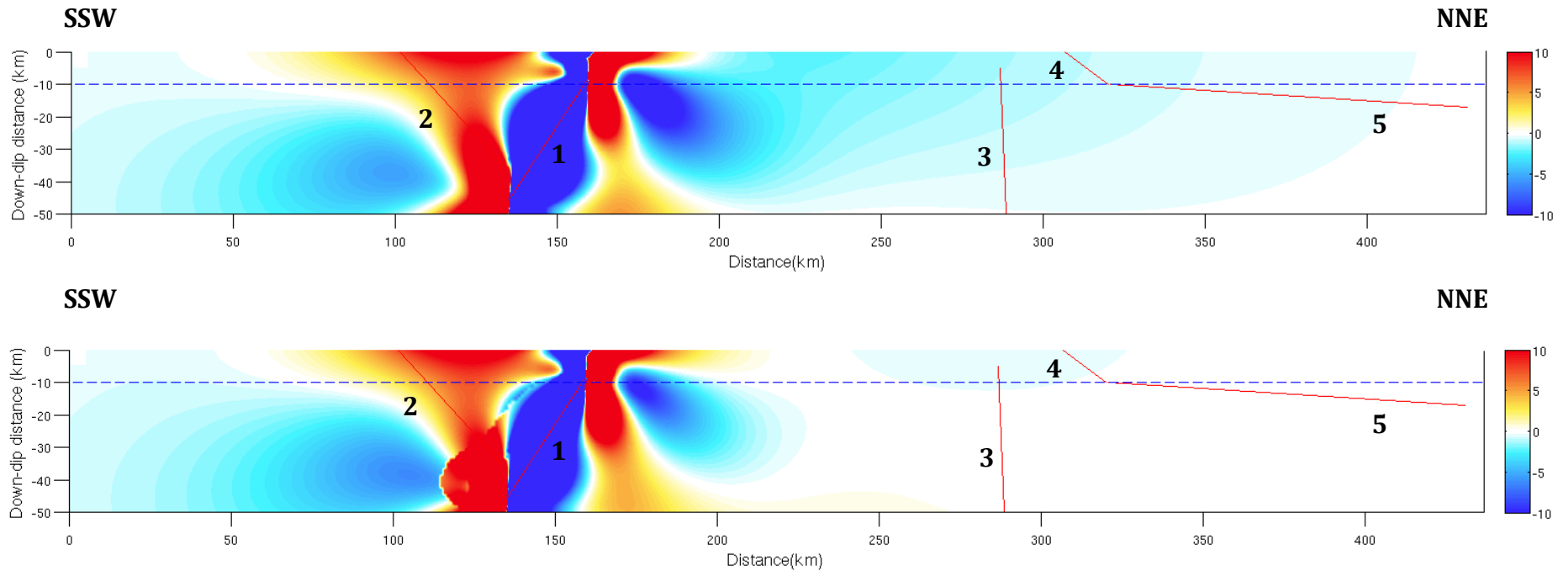


Figure 4.2: Cross-section of Coulomb stress-change pattern perpendicular to the eastern-end of the Oldham fault. The upper cross-section corresponds to regional stress values for the Dauki, Kopili, and Tista faults. The lower cross-section corresponds to regional stress values for the Gish, Lingshi, MFT, and Sakteng faults. Blue-colored regions indicate areas that experienced a decrease in Coulomb stress. Red-colored regions indicate areas that experienced an increase in Coulomb stress. White-colored regions indicate areas that experienced no change in Coulomb stress. Faults are shown with red-colored lines. The dashed line corresponds to the depth interval that the original map view image was modeled at. Faults are numbered in the following order: 1)Oldham 2)Dauki 3)Kopili 4)MFT (frontal ramp) 5)MFT (basal detachment). The cross-section is sampled from 0 to 50 km depth and modeled with a color saturation index of -10 to 10 bar depicted by the legend at the right-hand side of the figure. The geographic orientation of cross-sections is from SSW to NNE from (24.31°N, 91.11°E) to (27.93°N, 92.81°E).

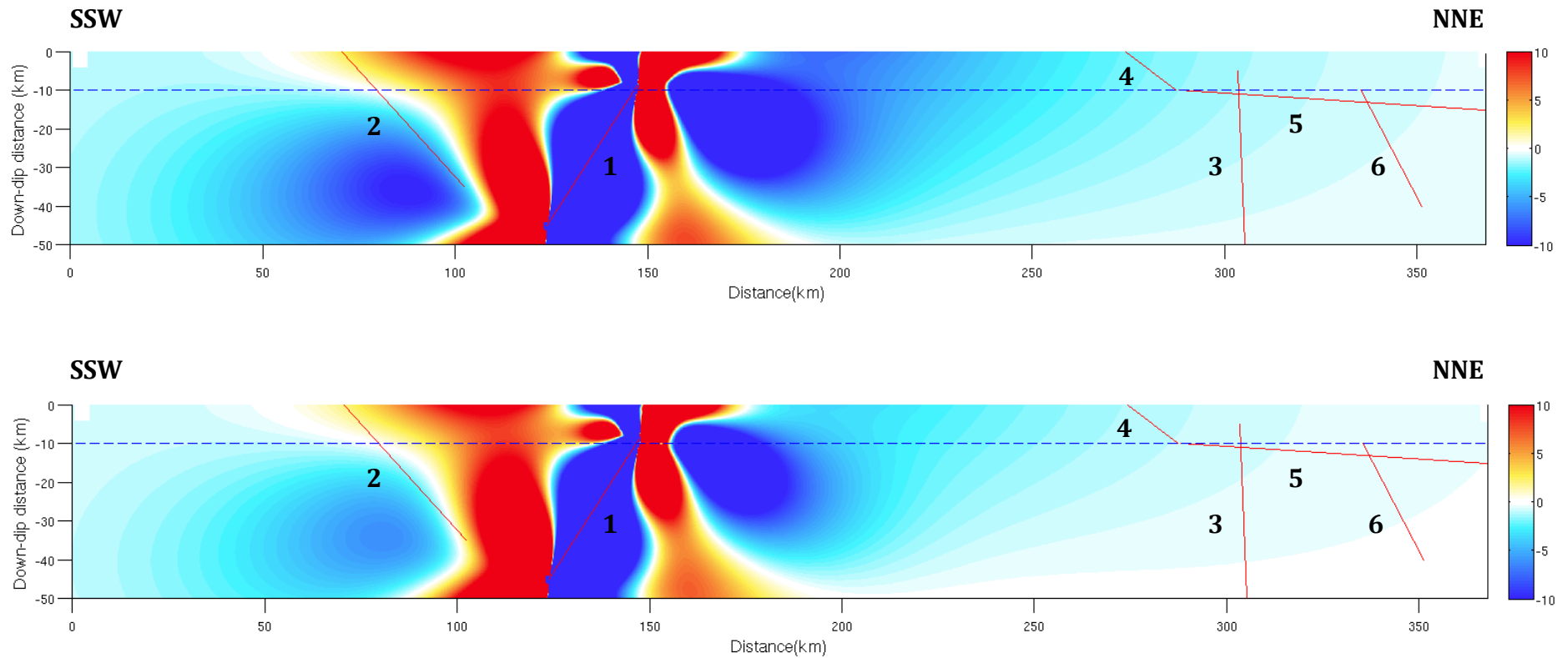


Figure 4.3: Cross-section of Coulomb stress-change pattern perpendicular to the central-segment of the Oldham fault. The upper cross-section corresponds to regional stress values for the Dauki, Kopili, and Tista faults. The lower cross-section corresponds to regional stress values for the Gish, Lingshi, MFT, and Sakteng faults. Blue-colored regions indicate areas that experienced a decrease in Coulomb stress. Red-colored regions indicate areas that experienced an increase in Coulomb stress. White-colored regions indicate areas that experienced no change in Coulomb stress. Faults are shown with red-colored lines. The dashed line corresponds to the depth interval that the original map view image was modeled at. Faults are numbered in the following order: 1)Oldham 2)Dauki 3)Kopili 4)MFT (frontal ramp) 5)MFT (basal detachment) 6)Sakteng. The cross-section is sampled from 0 to 50 km depth and modeled with a color saturation index of -10 to 10 bar depicted by the legend at the right-hand side of the figure. The geographic orientation of cross-sections is from SSW to NNE from (24.58°N, 90.70°E) to (27.61°N, 92.18°E).

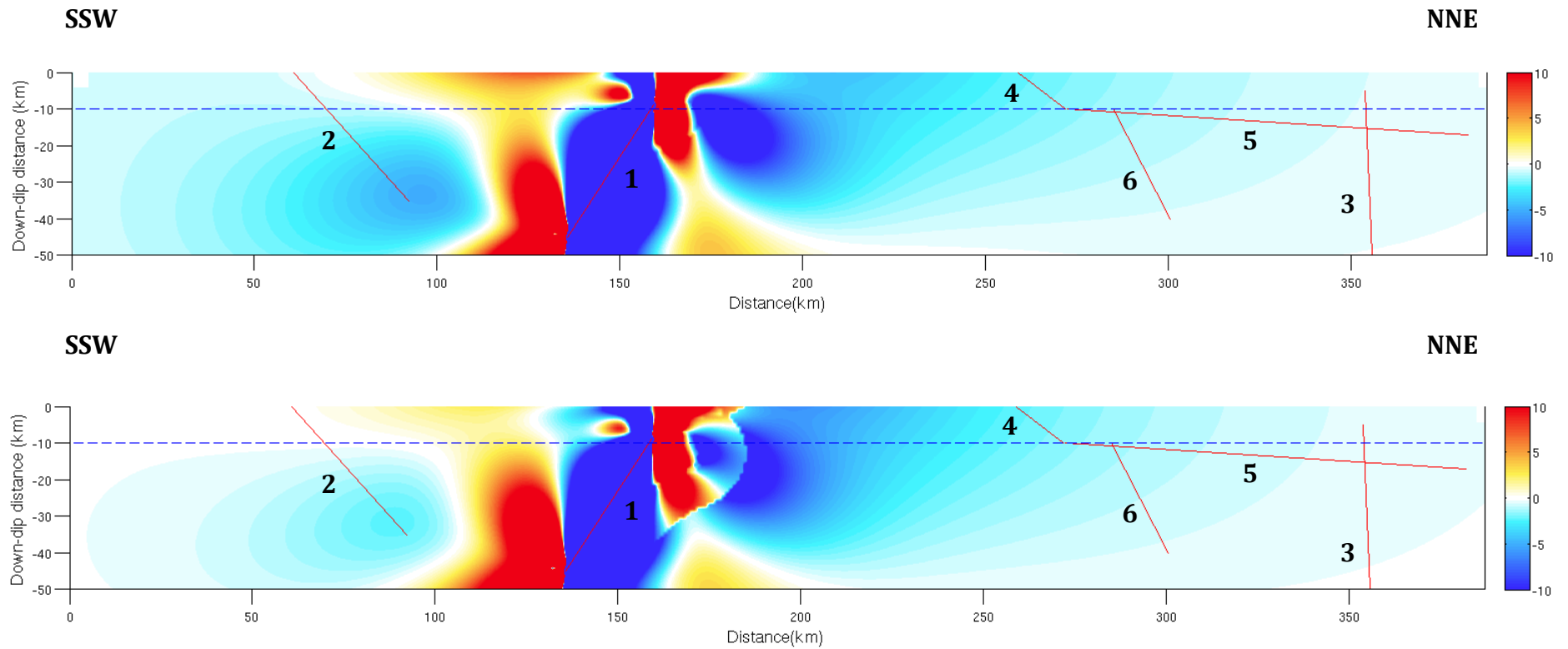


Figure 4.4: Cross-section of Coulomb stress-change pattern perpendicular to the western-end of the Oldham fault. The upper cross-section corresponds to regional stress values for the Dauki, Kopili, and Tista faults. The lower cross-section corresponds to regional stress values for the Gish, Lingshi, MFT, and Sakteng faults. Blue-colored regions indicate areas that experienced a decrease in Coulomb stress. Red-colored regions indicate areas that experienced an increase in Coulomb stress. White-colored regions indicate areas that experienced no change in Coulomb stress. Faults are shown with red-colored lines. The dashed line corresponds to the depth interval that the original map view image was modeled at. Faults are numbered in the following order: 1)Oldham 2)Dauki 3)Kopili 4)MFT (frontal ramp) 5)MFT (basal detachment) 6)Sakteng. The cross-section is sampled from 0 to 50 km depth and modeled with a color saturation index of -10 to 10 bar depicted by the legend at the right-hand side of the figure. The geographic orientation of cross-sections is from SSW to NNE from (24.66°N, 90.18°E) to (27.89°N, 91.63°E).

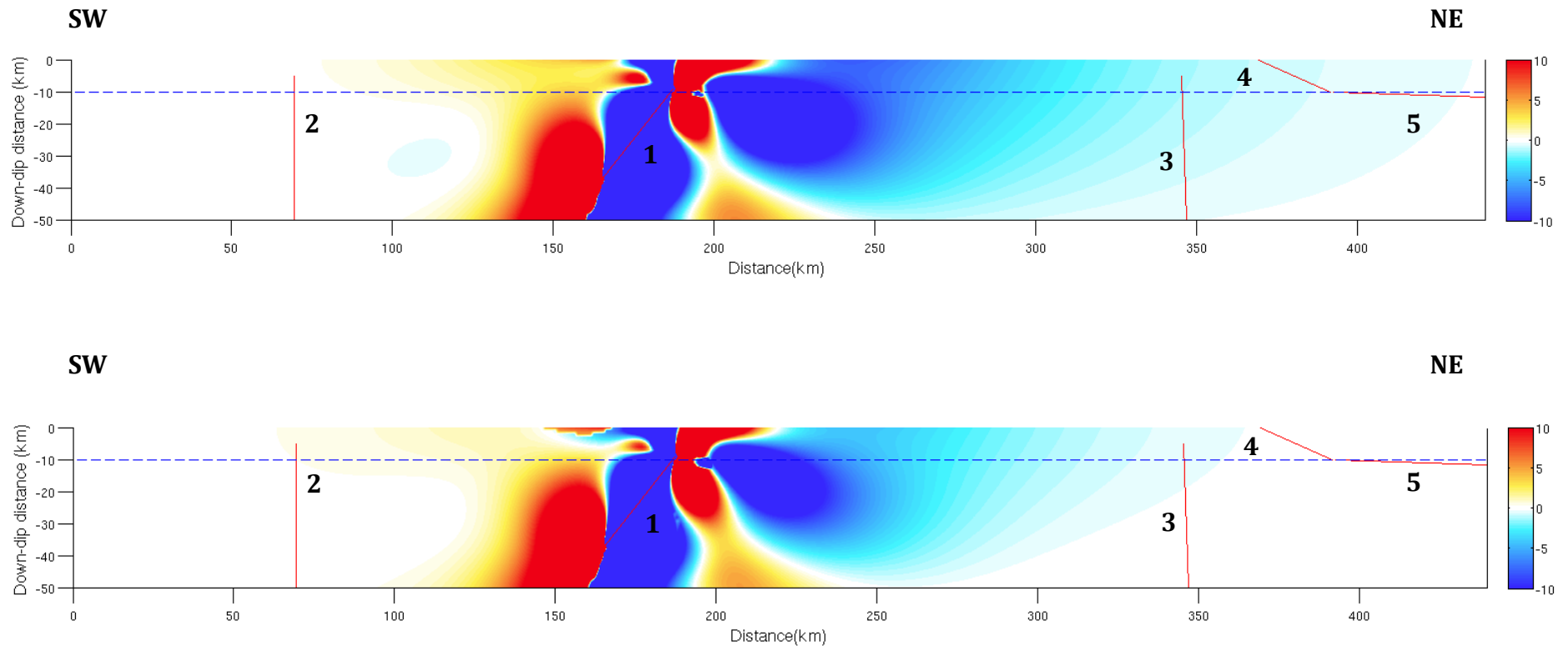


Figure 4.5: Cross-section of Coulomb stress-change pattern oblique to the Oldham fault and perpendicular to the Kopili and Tista faults. The upper cross-section corresponds to regional stress values for the Dauki, Kopili, and Tista faults. The lower cross-section corresponds to regional stress values for the Gish, Lingshi, MFT, and Sakteng faults. Blue-colored regions indicate areas that experienced a decrease in Coulomb stress. Red-colored regions indicate areas that experienced an increase in Coulomb stress. White-colored regions indicate areas that experienced no change in Coulomb stress. Faults are shown with red-colored lines. The dashed line corresponds to the depth interval that the original map view image was modeled at. Faults are numbered in the following order: 1)Oldham 2)Tista 3)Kopili 4)MFT (frontal ramp) 5)MFT (basal detachment). The cross-section is sampled from 0 to 50 km depth and modeled with a color saturation index of -10 to 10 bar depicted by the legend at the right-hand side of the figure. The geographic orientation of cross-sections is from SW to NE from (25.03°N, 89.29°E) to (27.21°N, 92.98°E).

4.3 OPTIMALLY ORIENTED COULOMB STRESS CHANGE

The first sub-set of map-view Coulomb stress-change patterns are mostly symmetric along a NE-SW axis and at all depths (Figure 4.1A-D), whereas the second sub-set is not as symmetric (Figure 4.1E-H). In cross-section, there is a drop in Coulomb stress along the Oldham fault and the area proximal to it on both fault blocks (Figures 4.2-4.5). However, in map view there is an increase in Coulomb stress proximal to the red-colored outline of the Oldham fault (Figure 4.1A-H). Generally, positive and negative Coulomb stress changes become greater with increasing depth (Figure 4.1A-H).

Outside of the red-colored fault outline, there are stress decrease lobes perpendicular to the strike of the Oldham fault. These zones of stress decrease are known as stress shadows and are larger for source faults with greater L/W ratios because the area of stress decrease grows broader along the strike of the rupture as the L/W ratio increases (Lin and Stein, 2004). Conversely, the amount of stress increase along the ends of a short and long fault are similar, but different faults transfer different amounts of stress to an adjacent patch of similar size (Lin and Stein, 2004). In the model the Oldham fault has a $L/W = \sim 2.5$, a low to moderate ratio. Therefore, the areal extent of stress decrease perpendicular to the strike of the fault should be significantly larger than the stress increase at the fault tips. This is indeed the case as the stress shadows perpendicular to the strike of the Oldham fault are approximately twice the size of stress increase lobes beyond the tips of the fault. This is apparent for both the first sub-set (Figure 4.1A-D) and second sub-set (Figure 4.1E-H) of optimally oriented Coulomb stress-change calculations.

At shallower depths of 10 and 20 km, the stress shadow lobe north of the Oldham fault is larger and greater in magnitude (Figure 4.1A-B/E-F). However, with increasing depth the southern stress shadow lobe increases in size and magnitude, to the point where it is almost equal to the northern lobe at 30km (Figure 4.1C/G). At greater depth the southern stress shadow lobe becomes larger and greater in magnitude than the northern lobe (Figure 4.1D/H). Furthermore, this same pattern is observed for lobes of Coulomb stress increase. At shallower depths, lobes of Coulomb stress increase are larger and greater in magnitude north of the Oldham fault, while at greater depth lobes of Coulomb stress increase are larger and greater in magnitude south of the fault. This pattern for Coulomb stress increase is better observed in cross-section, where it is present in all orientations sampled (Figures 4.2-4.5).

The areal extent of the entire Coulomb stress-change pattern is from approximately 23.5°N to 28°N and 89.5°E to 93°E (Figure 4.1). However, Coulomb stress magnitude decreases rapidly away from the Oldham fault, from $> \pm 90$ bar along the Oldham fault to ± 1 bar in the area from 25°N to 26.5°N and 90.5°E to 92°E (Figure 4.1). It is almost certain that some areas experienced an increase or decrease in excess of ± 100 bar, but Coulomb 3.3 only calculates Coulomb stress magnitude up to a maximum of ± 99 bar.

With regards to the effect on nearby receiver faults, it is evident that the Dauki fault is the most affected. The entire Dauki fault is within the Coulomb stress-change field. The eastern segment of the Dauki fault experienced a very large increase in Coulomb stress, while the western segment experienced a low-to-

moderate decrease in Coulomb stress. The Kopili, MFT, and Sakteng faults are also within the Coulomb stress change field, but experienced much lower magnitudes of Coulomb stress change. Only the central segment of the MFT and northern half of the Kopili fault appear to be affected (Figure 4.1), whereas the entire Sakteng fault is within the northern stress shadow lobe (Figures 4.1/4.3/4.4). The southern half of the Tista fault is also within the fringes of the southern extent of the Coulomb stress-change field where it experienced low Coulomb stress increase and decrease (Figure 4.1A-D). The Gish and Lingshi faults appear to be unaffected by slip along the Oldham fault. In the following sub-sections the optimally oriented Coulomb stress change of receiver faults is discussed.

4.3.1 COULOMB STRESS CHANGE PATTERN ALONG THE OLDHAM FAULT

There is a large drop in Coulomb stress along the Oldham fault, in which the drop in Coulomb stress occurs on both fault blocks above and below the Oldham Fault across its entire width for all 50 km of depth sampled (Figures 4.2-4.5). There is also a drop in Coulomb stress above the fault's upper tip, but it narrows towards the surface and then widens again along the surface, which is to be expected for blind thrust faults (Lin and Stein, 2004). There is also a drop in Coulomb stress below the bottom tip of the fault but it narrows towards the bottom in cross-section. However, the largest Coulomb stress decrease is still in the area along the fault's width and length (Figures 4.1-4.5). It is important to note that although the drop in Coulomb stress is present across all 50 km of depth sampled, the size and magnitude of Coulomb stress change varies with depth. Specifically, the areal extent of Coulomb stress decrease is greatest from 15 to 40 km and the magnitude of Coulomb stress decrease is greatest along the fault and decreases with distance (Figures 4.2-4.5). Along the Oldham fault, the Coulomb stress decrease is likely in excess of -100 bar.

On both sides of this inner Coulomb stress decrease are two lobes of Coulomb stress increase. The southern stress lobe is deeper while the northern stress lobe is shallower because it is a south-dipping thrust, but both lobes are present across all 50 km of depth sampled (Figures 4.2-4.5). The magnitude of stress increase is larger at greater depth for the southern lobe while the magnitude of stress increase is larger at shallower depth for the northern lobe. Because it is a south-dipping thrust, there is a greater stress increase at shallow depths from 5 km

going toward the surface for approximately 25 km north of the Oldham fault (Figures 4.2-4.5). However, cross-sections show that the southern stress increase lobe is greater in areal extent along the surface south of the Oldham fault, but the magnitude of Coulomb stress increase is significantly lower than that of the northern stress increase lobe (Figures 4.2-4.5).

4.3.2 COULOMB STRESS CHANGE PATTERN ALONG THE DAUKI FAULT

Slip along the Oldham fault resulted in a large increase in Coulomb stress along the eastern segment of the Dauki fault (Figure 4.1A-C, Figure 4.2). The increase in Coulomb stress varies between 0 and ~60 bar and the largest increase occurred from 20 to 35 km depth. The upper 10 km of the Dauki fault experienced a minor increase in Coulomb stress between 0 and ~5 bar. The remainder of the Dauki fault experienced a drop in Coulomb stress between 0 and ~ -8 bar (Figures 4.3-4.4).

4.3.3 COULOMB STRESS CHANGE PATTERN ALONG THE MFT

The frontal ramp and basal detachment of the MFT both experienced a decrease in Coulomb stress (Figures 4.1E-F, Figures 4.2-4.4). However, the decrease in Coulomb stress along the basal detachment was negligible, whereas the frontal ramp segment experienced a low to moderate decrease in Coulomb stress between 0 and ~ -3 bar. Specifically, the eastern-central segment of the frontal ramp north of the Oldham fault experienced the largest decrease in Coulomb stress (Figure 4.4).

4.3.4 COULOMB STRESS CHANGE PATTERN ALONG STRIKE-SLIP FAULTS

The northern half of the Kopili fault experienced a decrease in Coulomb stress between 0 and ~ -3 bar along its entire surface (Figure 4.1A-D, Figures 4.2-4.4). The entire Sakteng fault experienced a decrease in Coulomb stress of the same magnitude along its entire surface (Figure 4.1E-H, Figures 4.3-4.4). The Tista fault was shown to run along the southern fringes of the Coulomb stress-change pattern (Figure 4.1A-D, 4.5). The change in Coulomb stress is negligible based on these calculations. The Lingshi and Gish faults experienced no change in Coulomb stress (Figure 4.1E-H).

4.4 DIFFERENCES IN COULOMB STRESS CHANGE PATTERN BETWEEN REGIONAL STRESS VALUES

Coulomb stress-change calculations were produced using optimally oriented thrust faults with two sets of regional stress values. Both sets of regional stress values produced similar results, especially with regards to Coulomb stress-change patterns and the resulting stress change to receiver faults. However, there were noticeable differences between results produced by the two sets of regional stress values. The most noticeable difference is the lack of symmetry in the Coulomb stress-change pattern seen in map view (Figure 4.1). The first set of regional stress values produced a fairly symmetrical pattern along a NE-SW axis, in which stress shadow lobes are perpendicular to the strike of the Oldham fault (Figure 4.1A-D). However, in the Coulomb stress-change pattern for the second set the stress shadow lobes are not oriented as symmetrically. Specifically, the stress shadow lobes are not perpendicular to the strike of the Oldham fault, but are slightly oblique to it (Figure 4.1E-H). The northern stress shadow lobe extends to the northwest while the southern stress shadow lobe extends to the southeast.

In addition to this, the size of stress shadow lobes and their magnitude is smaller in the second set of regional stress values (Figure 4.1E-H) than in the first set (Figure 4.1A-D). Another major difference is the discrepancy in Coulomb stress drop between the northern and southern stress shadow lobes. In the first set (Figure 4.1A-D) the Coulomb stress drop was greater north of the Oldham fault, but with increasing depth the Coulomb stress drop became greater south of the Oldham fault especially at depths >30 km. This pattern of Coulomb stress drop with

increasing depth is still present in the second set of regional stress values (Figure 4.1E-H), but the resulting magnitude of stress drop is less significant. In both sets the magnitude of Coulomb stress drop north of the Oldham fault at 40 km depth is roughly similar, although the size of the lobe is larger in the first set (Figure 4.1D/H). However, the magnitude of Coulomb stress drop south of the Oldham fault at 30 and 40 km depth is not similar. Specifically, the magnitude of the southern stress shadow lobe for the second set of regional stress values (Figure 4.1G/H) is significantly lower than that of the first set (Figure 4.1C/D).

The cross sections show that the resulting Coulomb stress-change pattern on nearby receiver faults of interest is similar between both sets, especially for that of the Dauki fault.

5.0 DISCUSSION

This chapter presents a third set of results produced from Coulomb stress-change calculations on individual receiver faults. Inference and analysis of the resulting Coulomb stress change is discussed. This includes the size and magnitude of Coulomb stress change that receiver faults experienced and how this may affect future seismicity. Calculations were made using various color saturation indexes in order to better display Coulomb stress change.

5.1 COULOMB STRESS CHANGE ON RECEIVER FAULTS

The Coulomb stress-change calculations produced using optimally oriented receiver faults were useful in order to determine a general Coulomb stress-change pattern and to see the effect on nearby receiver faults. However, in order to precisely determine the effect of the 1897 Great Assam earthquake on receiver faults it was necessary to calculate the Coulomb stress change imparted to them individually. In order to do this, I first modeled all receiver faults together to determine the general Coulomb stress change imparted to them. I then modeled each receiver fault of interest separately with the Oldham fault to obtain a precise Coulomb stress-change pattern along the receiver fault surface. In turn, this information can be used to help predict the location of the next potential seismic event and explain the putative seismic gap as a result of Coulomb stress change.

5.1.1 COULOMB STRESS CHANGE ON ALL RECEIVER FAULTS

The Coulomb stress change for all receiver faults according to their individual rake is shown. This initial calculation was useful for a general overview of the resulting Coulomb stress change from slip along the Oldham fault. Furthermore, receiver faults that experienced a change in Coulomb stress generally matched the resulting Coulomb stress-change pattern seen in optimally oriented stress-change calculations. However, the information provided is not very precise because the user cannot determine where the largest increase or decrease in Coulomb stress occurred along a fault. Instead the user can only determine if there was mostly decrease or increase along a fault and the average magnitude of such a change in Coulomb stress. This is why I chose to investigate those faults that showed a substantial change in Coulomb stress individually. This included splitting receiver faults into patches so that I could determine where exactly each fault was experiencing a change in Coulomb stress.

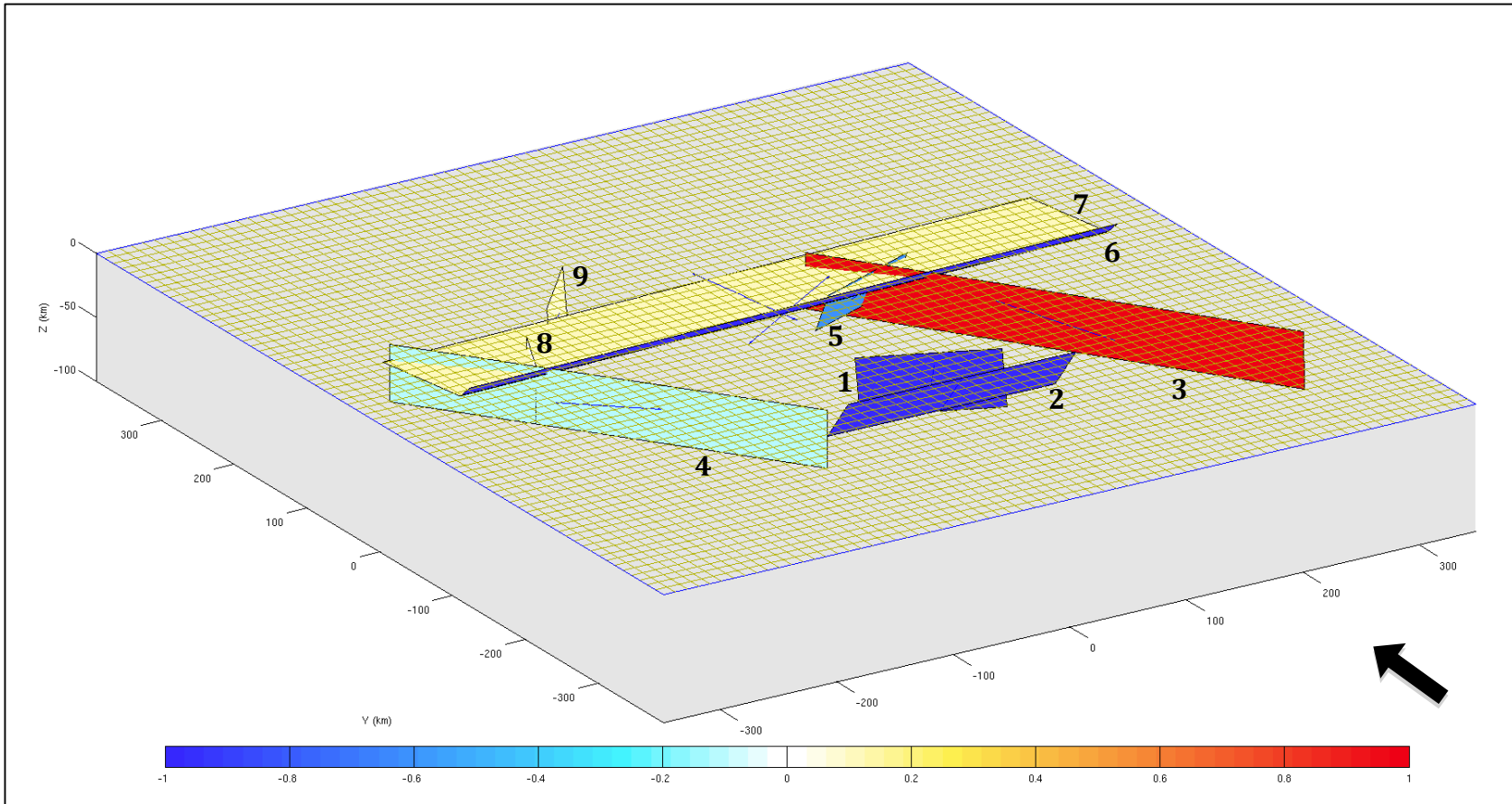


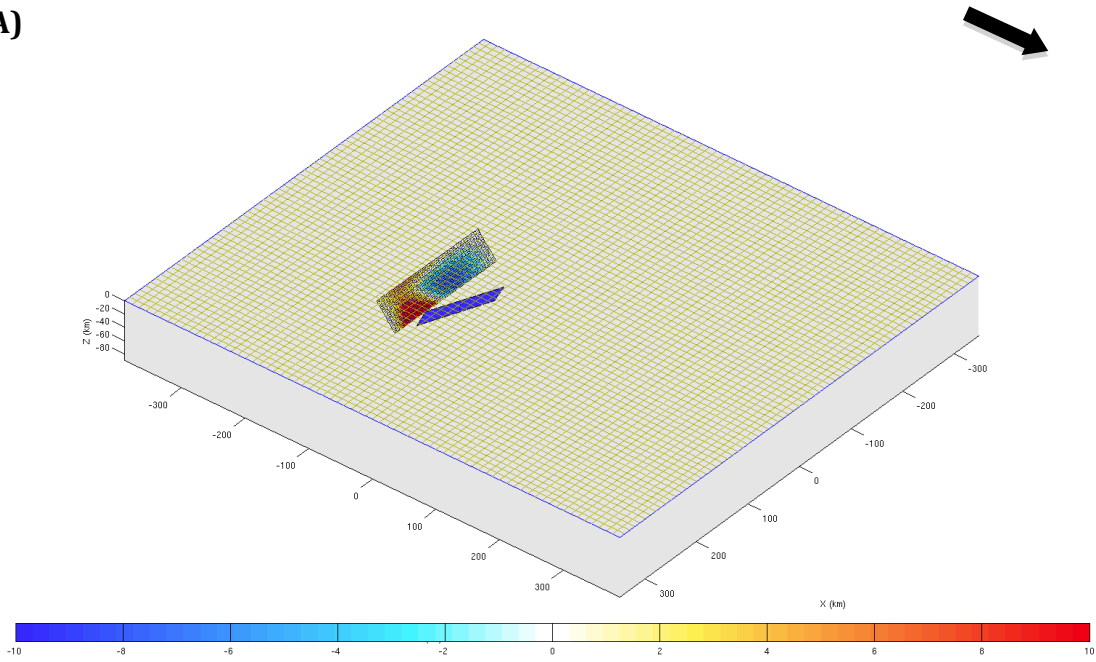
Figure 5.1: Coulomb stress change on all receiver faults according to individual rake. The figure shows Coulomb stress change imparted to all receiver faults as a result of slip along the Oldham fault. Coulomb stress change is calculated for each receiver fault based on the fault's individual rake. The rake of each fault is shown with thin black arrows. Coulomb stress change was calculated with a color saturation index of -1 to 1 bar according to the legend. A small index value allows for an intense color display of even minor changes in Coulomb stress, thereby showing faults that experienced appreciable changes in Coulomb stress that would need to be investigated more thoroughly. Faults that show little change in color likely experienced negligible amounts of Coulomb stress change. Blue-colored regions indicate areas that experienced a decrease in Coulomb stress. Red-colored regions indicate areas that experienced an increase in Coulomb stress. White-colored regions indicate areas that experienced no change in Coulomb stress. Faults are numbered in the following order: 1)Oldham 2)Dauki 3)Kopili 4)Tista 5)Sakteng 6)MFT (frontal ramp) 7)MFT (basal detachment) 8)Gish and 9)Lingshi. The thick black arrow indicates north. The unit of spacing along the x- and y-axes is 100 km as shown by the hash marks.

5.1.2 COULOMB STRESS CHANGE ON THE DAUKI FAULT

The Dauki fault was the primary receiver fault of interest for several reasons. First, it is the principal fault causing the uplift of the Shillong Plateau, along with the Oldham fault. Second, it was the most affected receiver fault as shown by initial Coulomb stress-change calculations. It was the only receiver fault within lobes of significant Coulomb stress increase. Third, the Dauki fault is known to be seismically active (Banerjee et al., 2008; Kayal et al., 2012). Therefore it is important to determine the Coulomb stress change on this fault due to a previous seismic event because it could induce future seismic activity.

The Dauki fault was modeled with the highest resolution because it was the primary receiver fault of interest. Splitting in Coulomb 3.3 is done according to intervals along length by width. I chose to use a 42 by 10 splitting pattern that resulted in 420 individual fault patches. The length of the Dauki fault is 193.5 km and the width is 45.7 km, giving each fault patch a length of 4.6 km and a width of 4.6 km. Thus, each fault patch had an area of $\sim 21.1 \text{ km}^2$.

A)



B)

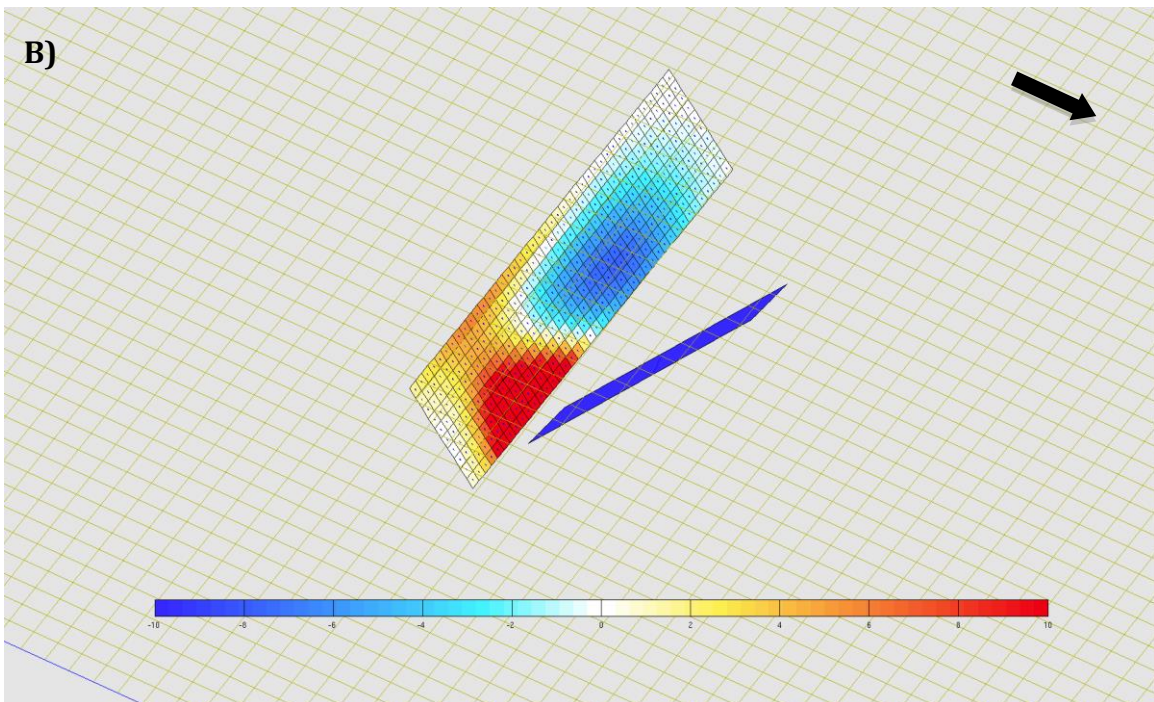


Figure 5.2: Coulomb stress change along the Dauki fault according to individual rake. A) Overview of the Dauki and Oldham faults. **B)** Close-up view of Coulomb stress change along the split Dauki fault. In both A) and B) the Oldham fault is solid blue. The resulting Coulomb stress-change pattern seen along the split Dauki fault closely matches initial optimally oriented Coulomb stress change calculations. Both A) and B) are modeled with a color saturation index of -10 to 10 bar according to the legend shown along the bottom. In A) the unit spacing along both x- and y-axes is 100 km as shown by the hash marks, while in B) one grid unit is ~10 km along each side. Thick black arrows indicate north.

The resolution obtained by using this splitting pattern provided excellent results graphically and allowed for precise determination of Coulomb stress change. In order to better determine the range of Coulomb stress-change magnitude, I modeled individual Coulomb stress change on the Dauki fault with several different color saturation indexes. Initially I used a ± 10 bar index to show a comprehensive overview of the resulting Coulomb stress-change pattern and where Coulomb stress change had occurred (Figure 5.2). The figures show that the majority of the Dauki fault experienced some amount of Coulomb stress change. Specifically, Coulomb stress increased along the eastern-third of the fault, whereas there was a decrease in stress towards the central segment of the fault. Along most of the remaining two-thirds of the fault Coulomb stress decreased. The western end of the fault has minimal to no Coulomb stress change. Furthermore, along the top of the fault to ~ 5 km down-dip, from the western end to ~ 74 km towards the interior, there is no Coulomb stress change. Overall, the extent of Coulomb stress decrease along the Dauki fault is slightly larger than the extent of Coulomb stress increase, but is far smaller in magnitude. The decrease in Coulomb stress across the Dauki fault varies between 0 and ~ -9 bar.

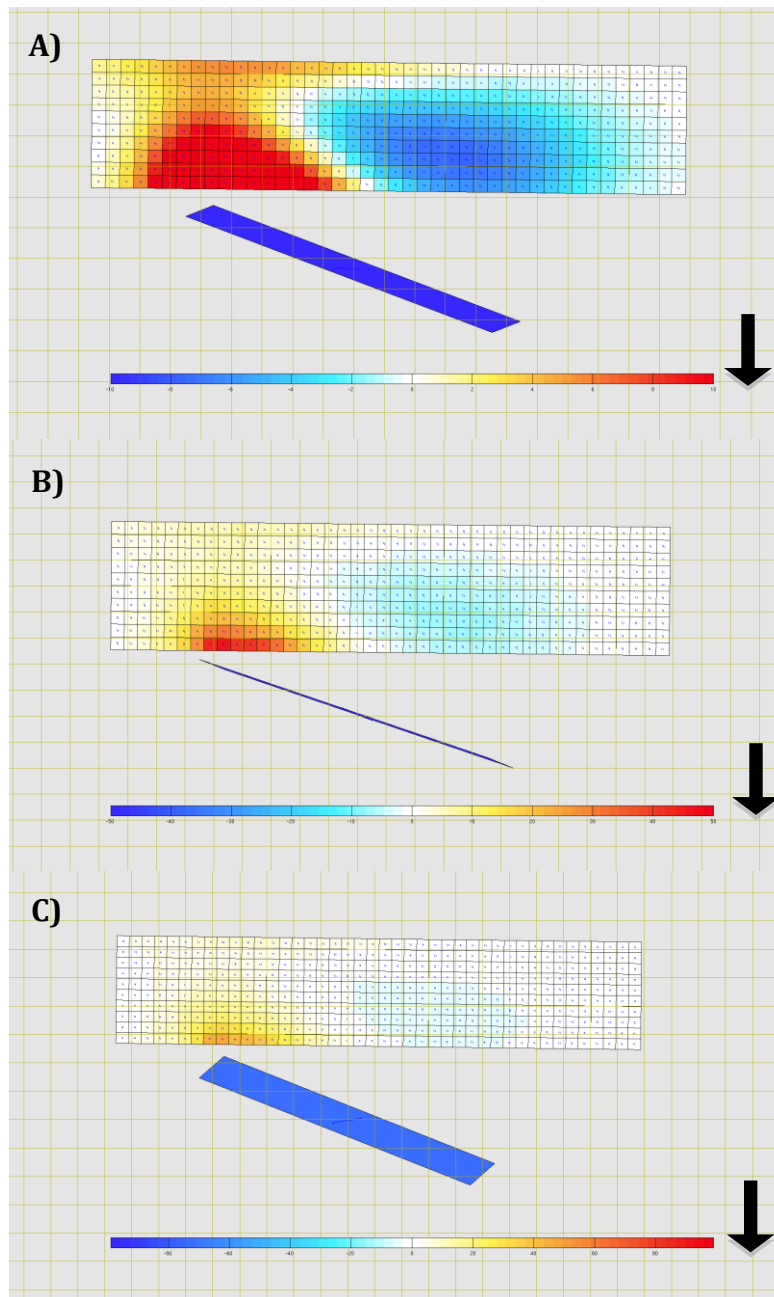


Figure 5.3: Coulomb stress change along the Dauki fault. A) Coulomb stress change along the split Dauki fault modeled with a color saturation index of -10 to 10 bar. B) Coulomb stress change along the split Dauki fault modeled with a color saturation index of -50 to 50 bar. C) Coulomb stress change along the split Dauki fault modeled with a color saturation index of -99 to 99 bar. In all cases the Oldham fault is solid blue. Thick black arrows indicate north. In A), B), and C) one grid unit is ~ 10 km along each side.

The upper ~18 km of the eastern segment, from the end to ~74 km towards the interior, experienced a moderate increase in Coulomb stress between 0 and ~7 bar. However, the Coulomb stress increase on the lower half of this eastern segment was of much greater magnitude. In order to better determine the magnitude of Coulomb stress increase I modeled the Dauki fault with ± 50 , ± 60 , ± 80 , ± 90 , and ± 99 bar indexes (Figure 5.3). With each increasing increment the color intensity decreases along the fault because the same color scheme is used to display a much greater interval of stress magnitude. In turn this allows for a more precise determination of Coulomb stress-change magnitude. Using this method it was determined that the lower half of the eastern-third of the Dauki fault experienced an increase in Coulomb stress between 0 and ~55 bar. The greatest increase in Coulomb stress occurred along the bottom eastern end, specifically between 36.8 km and 41.4 km from the lower eastern tip of the fault extending upward from 35 km to 30.4 km. It corresponds to a surface geographic location of (25.4°N, 91.7°E). Using the “Calc stress at a point” function, it was determined that a Coulomb stress increase of up to ~60 bar occurred in this area.

5.1.3 COULOMB STRESS CHANGE ON THE KOPILI FAULT

The Kopili fault was modeled with a splitting pattern of 26 by 3 giving 78 individual fault patches. This produced fault patches that had a length of 15.2 km and a width of 15.0 km giving each individual fault patch an area of $\sim 227.5 \text{ km}^2$. The Kopili fault was shown to be within the northern stress shadow lobe in the initial optimally-oriented calculations. However, modeling Coulomb stress change on the Kopili fault individually indicated both a decrease and increase in Coulomb stress along the fault (Figure 5.4).

The northern-quarter of the fault experienced a drop in Coulomb stress between 0 and ~ -1.5 bar along its entire surface. This was expected as initial Coulomb stress-change calculations showed this area to be within the northern stress shadow. Progressively, the central segment of the Kopili fault experienced an increase in Coulomb stress between 0 and 4 bar along its entire surface. This area of Coulomb stress increase occurred along ~ 150 km of the Kopili fault. There was no Coulomb stress change along the southern-quarter of the Kopili fault.

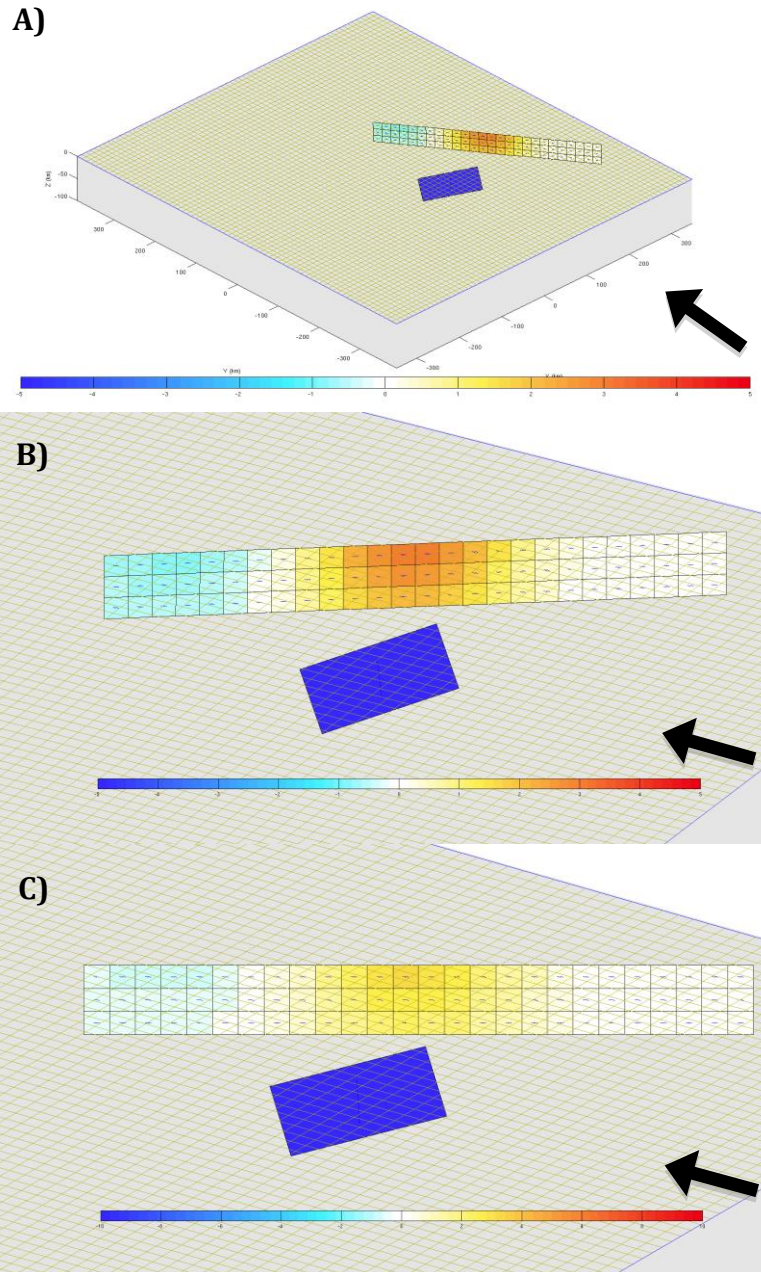


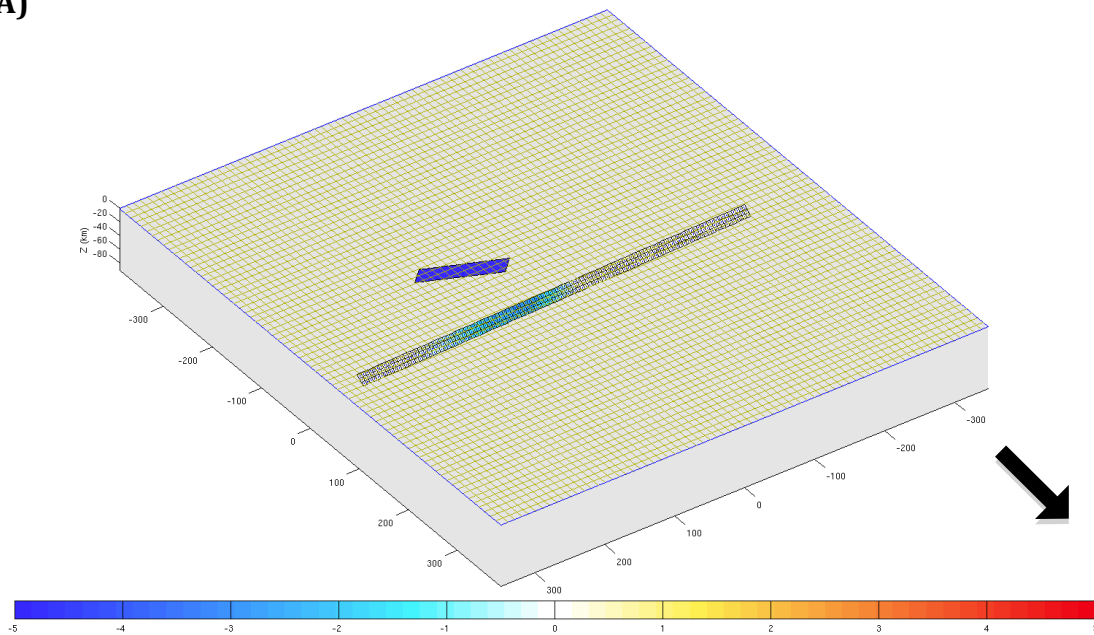
Figure 5.4: Coulomb stress change along the Kopili fault according to individual rake. A) Overview of the Kopili and Oldham faults modeled with a color saturation index of -5 to 5 bar. B) Coulomb stress change along the split Kopili fault modeled with a color saturation index of -5 to 5 bar. C) Coulomb stress change along the split Kopili fault modeled with a color saturation index of -10 to 10 bar. In all cases the Oldham fault is solid blue. Thick black arrows indicate north.

5.1.4 COULOMB STRESS CHANGE ON THE FRONTAL RAMP OF THE MFT

Both the frontal ramp and part of the basal detachment were within the northern stress shadow according to initial Coulomb stress-change calculations. However, I chose to model only the frontal ramp portion of the MFT individually for several reasons. First, the frontal ramp experienced the larger decrease in Coulomb stress, while the decrease in Coulomb stress along the basal detachment appeared negligible. Second, because larger magnitude earthquakes occur along the frontal ramp it was more important to examine the Coulomb stress change that had occurred along it, as opposed to the basal detachment.

The frontal ramp of the MFT was modeled with a splitting pattern of 110 by 3 giving 330 individual fault patches. This produced fault patches that had a length of 5.2 km and a width of 5.2 km giving each individual fault patch an area of $\sim 26.8 \text{ km}^2$. Individual modeling showed that the eastern-central segment of the frontal ramp experienced a decrease in Coulomb stress along its entire surface (Figure 5.5). The area directly north of the Oldham fault experienced the largest drop in Coulomb stress, while the surrounding areas had considerably lower levels. The area of Coulomb stress decrease was $\sim 187.0 \text{ km}$ long, whereas the most significant decrease occurred along the central $\sim 83.0 \text{ km}$. The decrease in Coulomb stress varied between 0 and $\sim -3 \text{ bar}$.

A)



B)

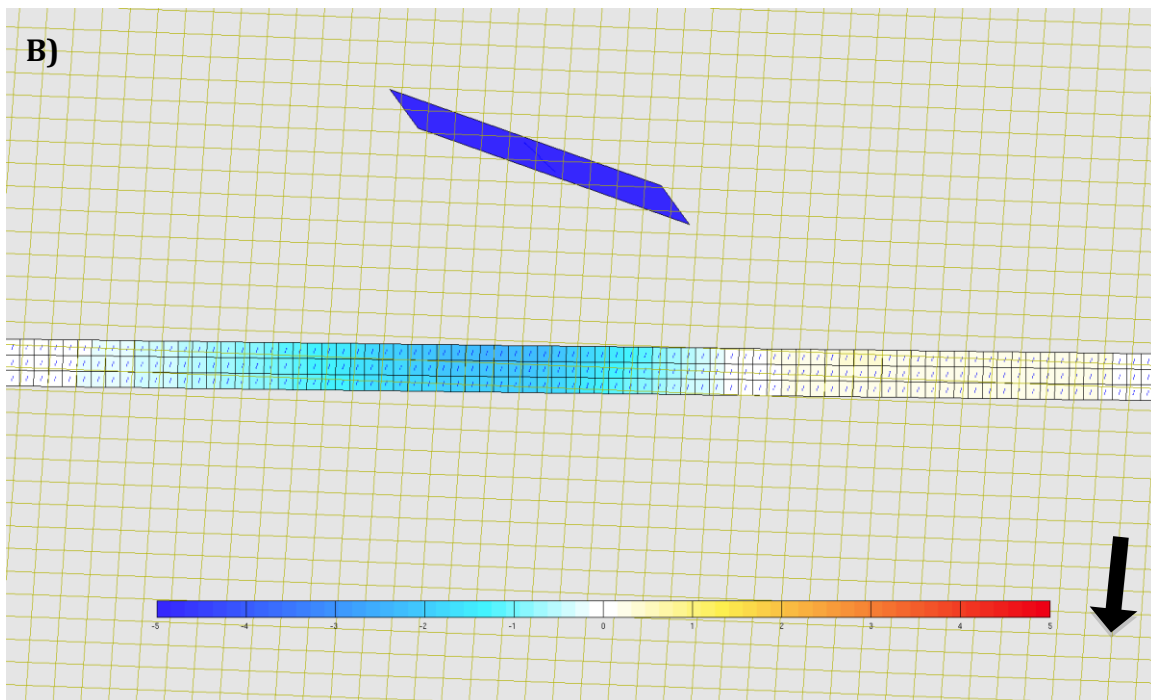


Figure 5.5: Coulomb stress change along the frontal ramp of the MFT according to individual rake. A) Overview of the frontal ramp of the MFT and Oldham fault modeled with a color saturation index of -5 to 5 bar. B) Coulomb stress change along the split frontal ramp of the MFT modeled with a color saturation index of -5 to 5 bar. In all cases the Oldham fault is solid blue. Thick black arrows indicate north. In A) the unit spacing for the x- and y-axes is 100 km as shown by the hash marks.

5.1.5 COULOMB STRESS CHANGE ON THE SAKTENG FAULT

The Sakteng fault was modeled with a splitting pattern of 10 by 3 giving 30 individual fault patches. This produced fault patches that had a length of 10.0 km and a width of 10.6 km giving each individual fault patch an area of $\sim 107.5 \text{ km}^2$. Individual modeling showed that almost the entire Sakteng fault experienced a decrease in Coulomb stress (Figure 5.6), very similar results as the optimally-oriented calculations. The northern tip of the fault did not experience a change in Coulomb stress. However, the remainder of the fault did experience a decrease in Coulomb stress between 0 and ~ -1.5 bar along its entire surface.

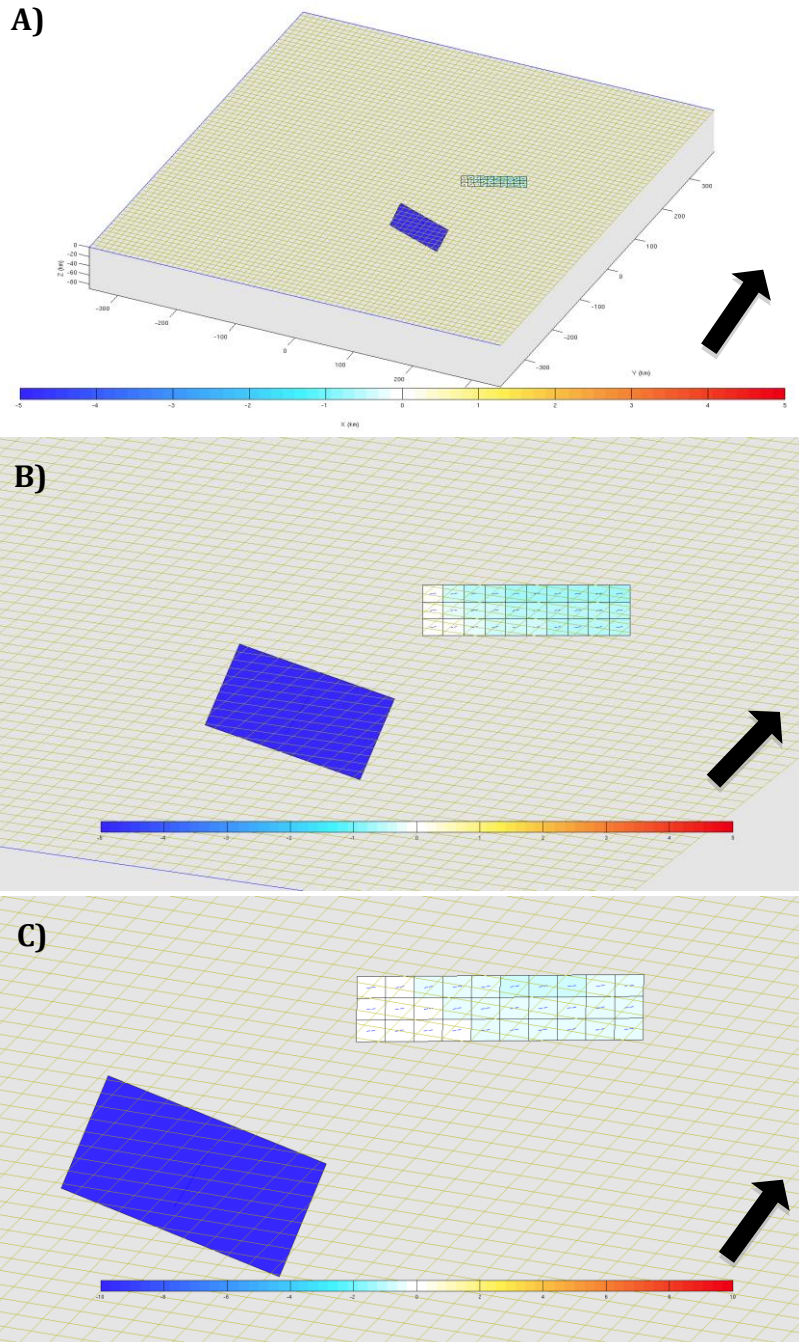


Figure 5.6: Coulomb stress change along the Sakteng fault according to individual rake. A) Overview of the Sakteng and Oldham faults modeled with a color saturation index of -5 to 5 bar. B) Coulomb stress change along the split Sakteng fault modeled with a color saturation index of -5 to 5 bar. C) Coulomb stress change along the split Sakteng fault modeled with a color saturation index of -10 to 10 bar. In all cases the Oldham fault is solid blue. Thick black arrows indicate north. In A) the unit spacing for the x- and y-axes is 100 km as shown by the hash marks.

5.1.6 COULOMB STRESS CHANGE ON THE TISTA FAULT

Initial Coulomb stress-change calculations suggested that the Tista fault was minimally affected by slip along the Oldham fault. The southern end of the Tista fault ran along the fringes of the southern stress shadow and north of this the fault was within an area of minimal Coulomb stress increase. The Tista fault was individually modeled with a splitting pattern of 38 by 5 giving 190 individual fault patches (Figure 5.7). This produced fault patches that had a length of 9.0 km and a width of 9.0 km giving each individual fault patch an area of $\sim 81.2 \text{ km}^2$.

Modeling showed that the southern-quarter of the Tista fault experienced an increase in Coulomb stress. Coulomb stress increased along the entire surface of the fault from the southern tip to $\sim 72 \text{ km}$ towards the interior (Figure 5.7B). The increase in Coulomb stress varied between 0 and $\sim 3.5 \text{ bar}$, whereby the largest increase occurred at the southern tip of the fault. There was no decrease in Coulomb stress.

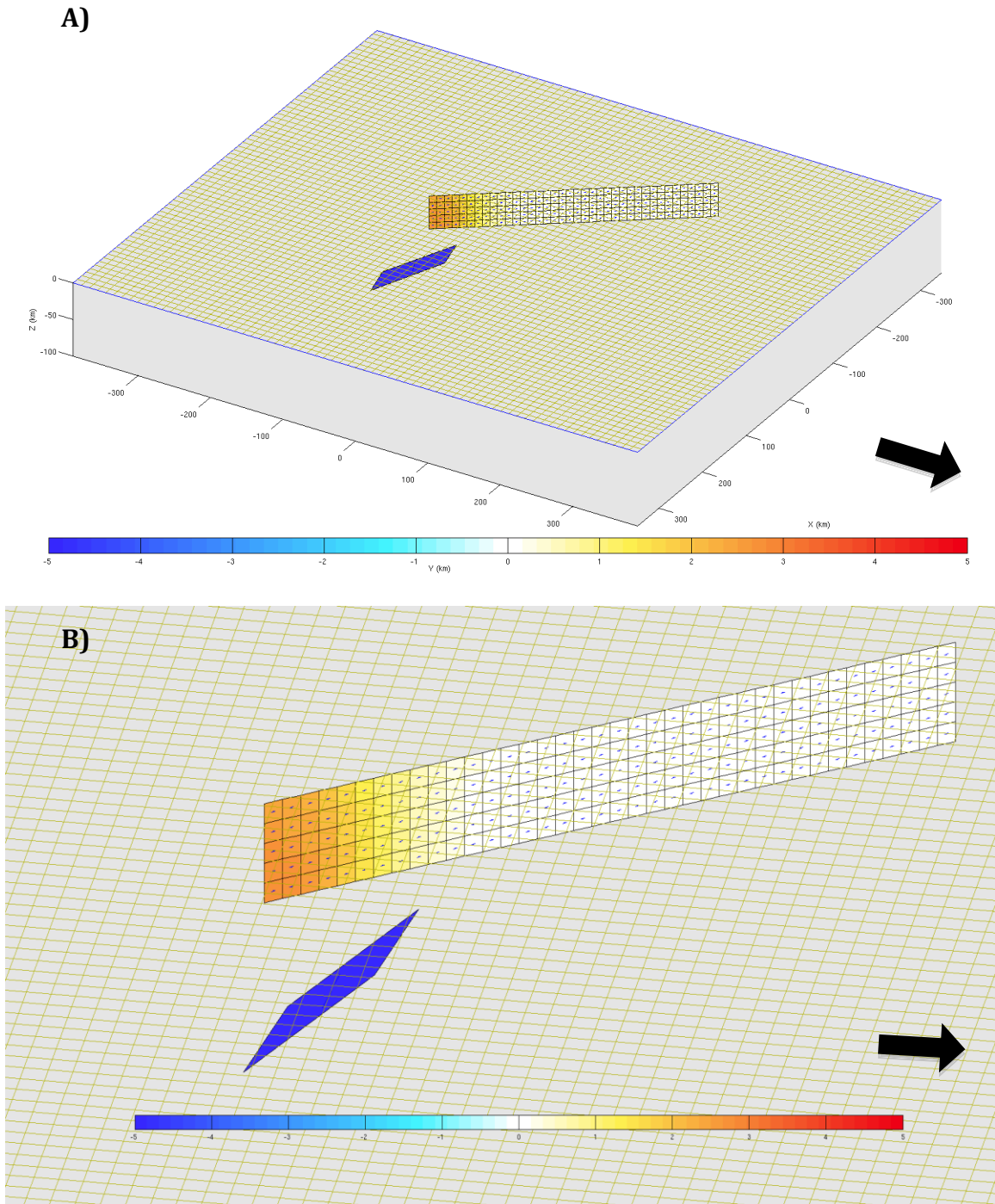


Figure 5.7: Coulomb stress change along the Tista fault according to individual rake. A) Overview of the Tista and Oldham faults modeled with a color saturation index of -5 to 5 bar. **B)** Coulomb stress change along the split Tista fault modeled with a color saturation index of -5 to 5 bar. In all cases the Oldham fault is solid blue. Thick black arrows indicate north. In A) the unit spacing for the x- and y-axes is 100 km as shown by the hash marks.

5.2 CAUSE OF THE SEISMIC GAP IN THE BHUTAN HIMALAYA

Gahalaut et al. (2011) concluded that low seismicity in the Bhutan Himalaya was the result of static stress changes caused by the 1897 Great Assam earthquake. Their model showed that a potential stress shadow between -1 and -2 bar, caused by the earthquake, coincides with the putative seismic gap along the Bhutan Himalaya (Figure 2.11). Gahalaut et al. (2011) also noted that low seismicity in the Bhutan Himalaya may be attributed to strain accumulation during the inter-seismic period. During this period, small to moderate earthquakes occur along the down-dip edge of the detachment under the Lesser Himalayas, while the up-dip region underneath the Sub Himalaya experiences very little seismicity.

In addition to this, Gahalaut et al. (2011) notes that variation in sub-surface structure may control seismicity rates, specifically the presence or absence of the ramp on the MFT, along which the earthquakes of the HSB occur. Earthquakes of the HSB occur along the ramp where the transition from seismically active detachment to aseismic slipping detachment occurs (Gahalaut et al., 2011). However, Gahalaut et al. (2011) note that seismicity rates may not be very influenced by the presence of the ramp because it is located along both the Bhutan and Nepal Himalayas, of which the latter has not shown a lack of seismicity as the former. Therefore, Gahalaut et al. (2011) attributes the putative seismic gap of the Bhutan Himalaya to stress changes caused by the 1897 Great Assam earthquake, which resulted in a stress shadow along the region.

Results of my research partially agree with the results of Gahalaut et al. (2011). The numerical model shows that a stress shadow over the foothills of the Bhutan Himalaya was formed by the 1897 Great Assam earthquake and coincides

with part of the putative seismic gap of the Bhutan Himalaya (Figure 4.1). However, the magnitude of Coulomb stress decrease shown in the model suggests that the stress shadow is not the main cause of the putative seismic gap.

Results show that the frontal ramp of the MFT, north of the Oldham fault, did experience a potential drop in Coulomb stress up to ~ -3 bar. This region of the MFT is directly south of the putative seismic gap. This drop in Coulomb stress could have had a potentially significant effect on seismicity along the seismogenic detachment in the area. The lack of seismicity due to a drop in Coulomb stress would result in less stress transfer to the basal detachment segment of the MFT leading to prolonged stress and strain accumulation.

The 1897 Great Assam earthquake resulted in significant Coulomb stress change to other nearby strike-slip faults, of which the most affected were the Kopili, Tista, and Sakteng faults. The northern-quarter of the Kopili fault and the entire Sakteng fault experienced a small decrease in Coulomb stress, which is attributable to the stress shadow. However, the southern-quarter of the Tista fault and central segment of the Kopili fault experienced a small-to-moderate increase in Coulomb stress.

The most affected fault was the Dauki fault, which experienced very significant increases in Coulomb stress along its eastern segment, which is a serious seismic hazard risk that needs to be further assessed, as it is the most likely location for a future seismic event according to the model.

6.0 CONCLUSION

Based on my research the 1897 Great Assam earthquake resulted in widespread Coulomb stress change that could have long-term implications for future seismic activity in the region. My models showed that as a result of the earthquake, a stress shadow of up to ~ -2 bar formed in the area of the putative seismic gap along the Bhutan Himalaya. Despite the fact that Coulomb stress changes of 0.1 bar can lead to significant changes in seismicity rates (Ross Stein; personal comm. 2014), my results showed that multiple factors likely contributed to the formation of a seismic gap along the Bhutan Himalaya. It is the result of several outcomes of the 1897 Great Assam earthquake including both the stress shadow and resulting Coulomb stress change imparted to nearby strike-slip and reverse faults, and their effect on stress loading in the Shillong Plateau region. The predominance of strike-slip faulting in the eastern Himalayas was noted by De and Kayal, (2003) and Drukpa et al. (2006). Results from this study show that seismicity can be affected by Coulomb stress change imparted to strike-slip faults in the eastern Himalaya and Shillong Plateau.

The $M_w \sim 8.1$ 1897 Great Assam earthquake resulted in widespread Coulomb stress change, of which the majority of faults investigated experienced some amount of Coulomb stress change. The most affected fault in the region is the Dauki fault, which experienced a large increase in Coulomb stress along the bottom eastern end where an increase of up to ~ 60 bar potentially occurred. This area of intense Coulomb stress increase is the most likely location for a future seismic event. Since the 1897 Great Assam earthquake, the Shillong Plateau has continued to be an area

of high seismicity, with seismic events recorded at depths up to 50 km (Figure 6.1A-B). Two large earthquakes have occurred in the Shillong Plateau since 1897; a Mw 7.5 in 1923 and a Mw 7.1 in 1930 (Kayal, 2008). In addition to this many more seismic events of lower magnitude have been recorded. Although seismic events of the Shillong Plateau are inferred to occur along plateau-bounding faults (Bilham and England, 2001; Biswas et al., 2007; Kayal et al., 2012), the majority of recorded seismic events have been within the plateau itself (Figure 6.1B). This suggests the need for additional modeling of the stress regime within the plateau itself.

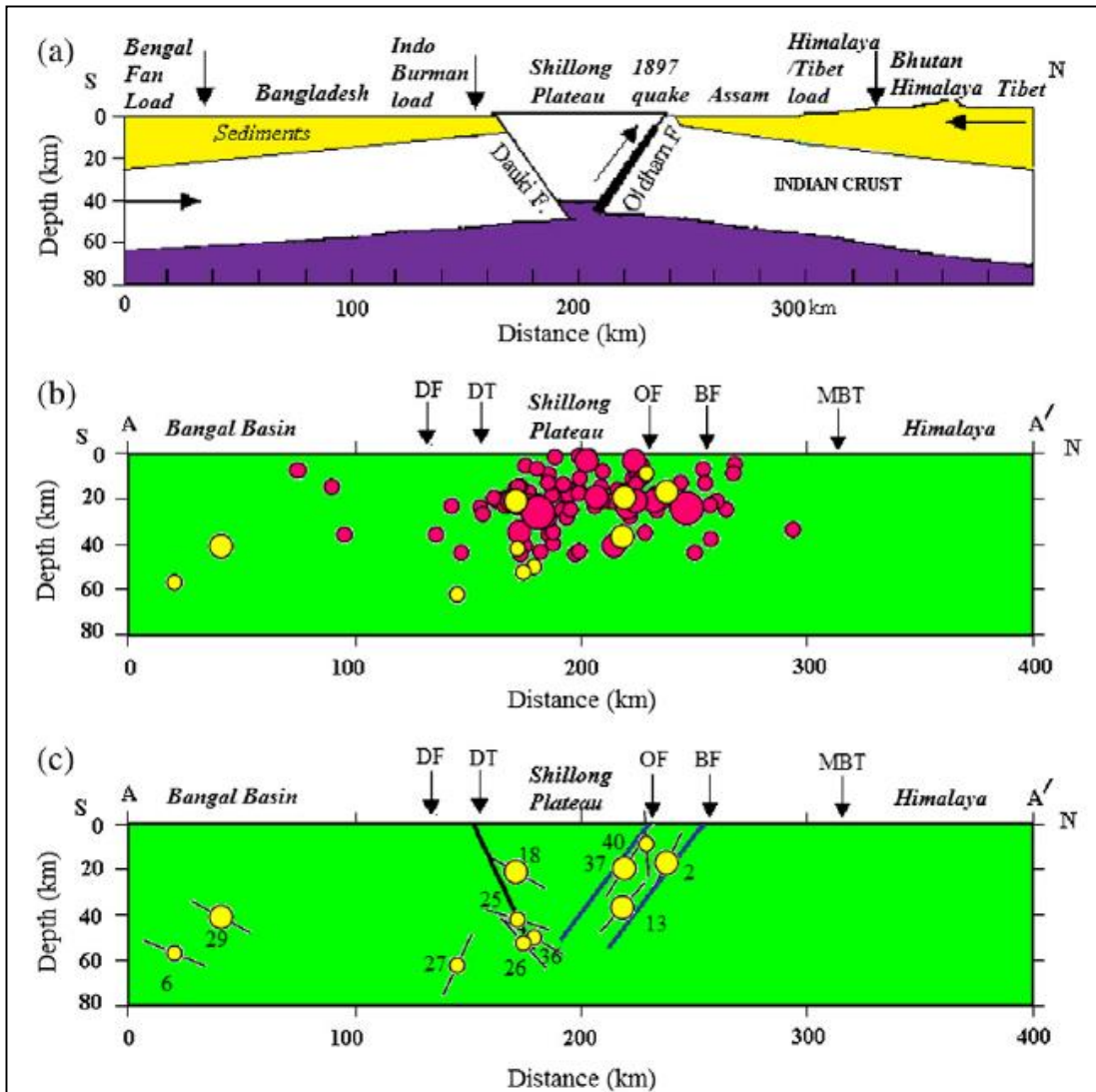


Figure 6.1: Seismicity of the Shillong Plateau based on recordings from 2001-2009. A) Cross-section of pop-up tectonic model of the Shillong Plateau after Bilham and England, 2001. B) Cross-section of seismic events across the Dauki, Dapsi, Oldham, and Brahmaputra fault zones. C) Cross-section of inferred fault planes of the selected solutions by the model of Kayal et al., 2012. Seismic events are displayed with circles and the location of major tectonic structures are shown with arrows (Kayal et al., 2012).

Coulomb stress change on strike-slip faults in the region was variable with faults experiencing an increase, decrease, or no Coulomb stress change at all. The 1897 Great Assam earthquake did not impart a Coulomb stress change to either the Gish or Lingshi faults. It did, however, impart a small decrease in Coulomb stress between 0 and ~ -1.5 bar to the majority of the Sakteng fault and northern-quarter of the Kopili fault. The central segment of the Kopili fault experienced an increase in Coulomb stress between 0 and ~ 4 bar. The southern-quarter of the Tista fault experienced an increase in Coulomb stress between 0 and ~ 3.5 bar. Therefore, it is evident that the 1897 Great Assam earthquake had widespread effects on the majority of faults within the region. Specifically, Coulomb stress has been imparted to the Dauki fault and to a much lesser extent strike-slip faults such as the Kopili and Tista.

The Kopili fault has been identified as the most seismically active fault in the region (Bhattacharya et al., 2012). Two large earthquakes ($M_w > 7.0$) occurred along the Kopili fault; in 1869 ($M_w 7.7$) and 1943 ($M_w 7.2$), both within a span of 75 years (Kayal et al., 2012). The former seismic event occurred along the south-eastern end of the fault where my results showed no change in Coulomb stress. The latter seismic event occurred along the center of the fault, where my results showed an increase in Coulomb stress. In addition to this recent seismic activity has been recorded along the Kopili fault (Figure 6.2). In 2009, a $M_w 5.1$ earthquake occurred along the center of the Kopili fault and a $M_w 6.3$ earthquake occurred along the northern end near the MFT (Kayal et al., 2012). The recording of two separate seismic events of significant magnitude (1943/ $M_w 7.2$ and 2009/ $M_w 5.1$) occurring

along the center of the Kopili fault suggests the release of built up Coulomb stress. Conversely, the presence of seismic events along the northern end of the Kopili fault where my results showed a decrease in Coulomb stress suggests the potential for unexpected seismicity in a region with a complex tectonic regime.

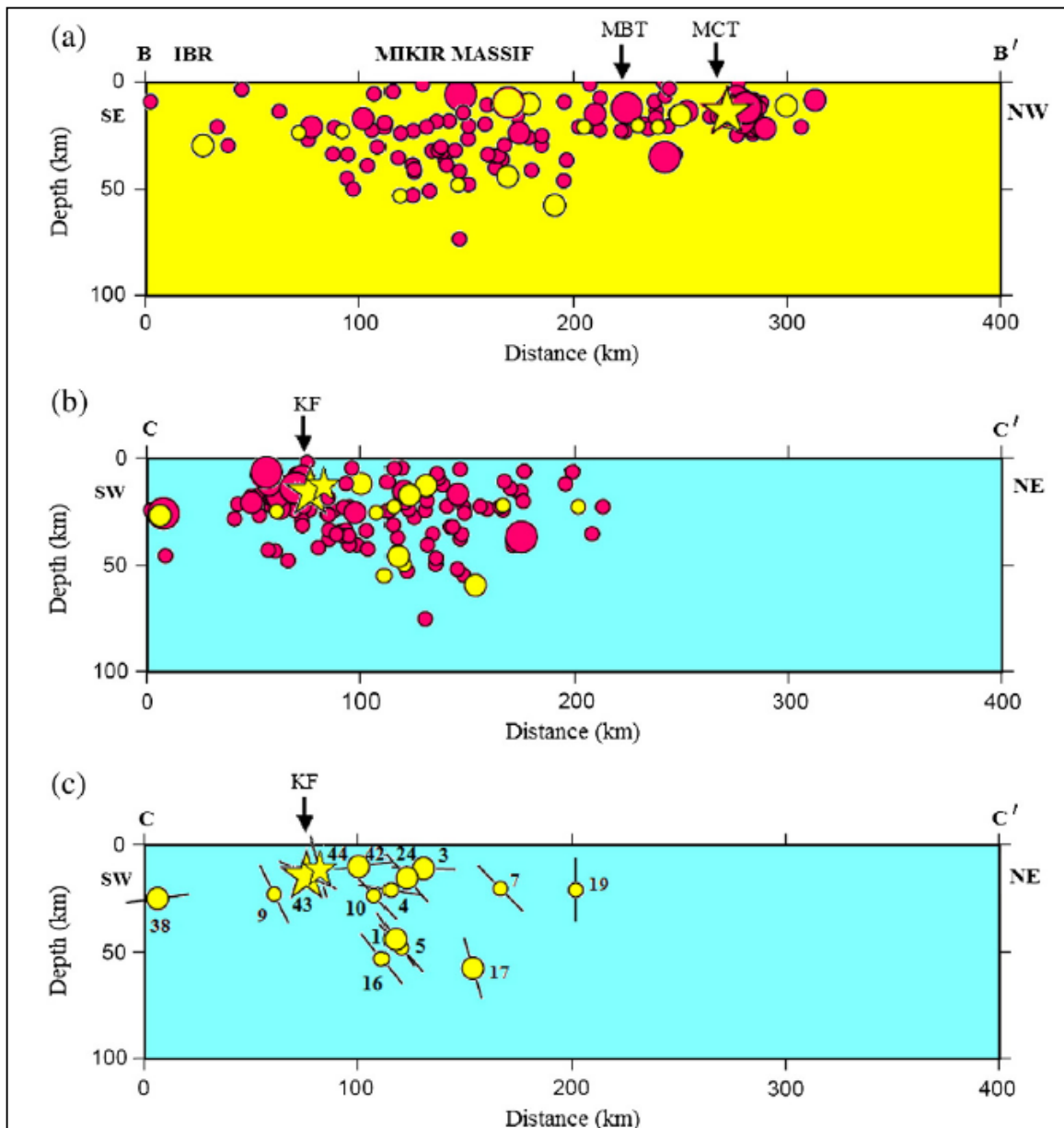


Figure 6.2: Seismicity of the Kopili fault based on recordings from 2001-2009. A) Cross-section of seismic events along the Kopili fault. B) Cross-section of seismic events across the Kopili fault (note the 50 km wide fault zone). C) Cross-section of inferred fault planes of the selected solutions by the model of Kayal et al., 2012. Seismic events are displayed with circles and the location of major tectonic structures are shown with arrows (Kayal et al., 2012)

The frontal ramp of the MFT experienced a small decrease in Coulomb stress between 0 and ~ -3 bar along its eastern-central segment, the remaining part of the MFT seems unaffected by the earthquake. This segment of the MFT is directly south of the putative seismic gap. This drop in Coulomb stress could have had a potentially significant effect on seismicity along the seismogenic detachment in the area. The lack of seismicity due to a drop in Coulomb stress would result in less stress transfer to the basal detachment segment of the MFT leading to prolonged stress and strain accumulation, in turn contributing to lower seismicity levels.

I conclude that the 1897 Great Assam earthquake did result in the formation of a stress shadow that overlies part of the putative seismic gap along the Bhutan Himalaya, but it is not the only cause of the gap. Based on the model, I propose the putative seismic gap is due to both the stress shadow along the MFT and Coulomb stress transfer and loading in strike-slip and reverse faults. Stress transfer resulted in a large increase in Coulomb stress along the eastern-end of the Dauki fault and small increases in Coulomb stress along segments of the Kopili and Tista faults. Conversely the frontal ramp of the MFT, just south of the putative seismic gap, incurred a small decrease in Coulomb stress, which has a significant effect on seismicity along the seismogenic detachment. In turn, this has an effect on stress transfer to the basal detachment of the MFT, which is directly below the Bhutan Himalaya. Decreased stress transfer may result in lower seismicity levels along the basal detachment because of prolonged stress and strain accumulation, further enhancing the stress shadow effect. Furthermore, the partitioning of Coulomb stress along the Dauki fault and nearby strike-slip faults such as the Kopili and Tista

faults also decreases stress loading on the Bhutan Himalaya. The coupled effect of the stress shadow, decreased stress transfer along the MFT, and the partitioning of Coulomb stress along the Dauki, Kopili, and Tista faults contribute to a potential seismic gap along the Bhutan Himalaya.

6.1 RECOMMENDATIONS FOR FUTURE RESEARCH

Lastly, as the area is seismically active it is a matter of time until another seismic event occurs, potentially one of significant magnitude. Based on the model, the next seismic event would most likely occur along the Dauki fault. Specifically, it would occur at the location of the largest Coulomb stress increase, along the bottom eastern-end. In this area there was a Coulomb stress increase of up to ~ 60 bar, a very significant increase that poses a serious seismic hazard. It is crucial to develop an estimate for a time frame of recurrence for potential seismic events, especially along the Dauki fault.

Sukhija et al. (1999) noted that paleo-seismic evidence suggests a recurrence period of 500 ± 100 years for great events ($M_w \geq 7.0$) in the Shillong Plateau. However, complex tectonics and tectonic stress due to rapid shortening could result in large earthquakes at any time (Kayal et al., 2012). My recommendation for future research is to calculate potential Coulomb stress accumulation along the Dauki fault since the 1897 Great Assam earthquake, and compare it to potential Coulomb stress release by earthquakes since 1897. This may be used to determine the amount of stress energy built up over time and a potential time frame for the recurrence of seismic events along the Dauki fault.

7.0 REFERENCES

- Andronicos, C. L., Velasco, A. A., & Hurtado Jr., J. M. (2007). Large-scale deformation in the India-Asia collision constrained by earthquakes and topography. *Terra Nova*, 19(2), 105-119. doi: 10.1111/j.1365-3121.2006.00714.x
- Banerjee, P., Burgmann, R., Nagarajan, B., & Apel, E. (2008). Intraplate deformation of the Indian subcontinent. *Geophysical Research Letters*, 35(18), 1-5. doi: 10.1029/2008GL035468
- Bhattacharya, P. M., Mukhopadhyay, S., Majumdar, R. K., and Kayal, J. R., 2008, 3-D seismic structure of the northeast India region and its implications for local and regional tectonics: *Journal of Asian Earth Sciences*, v. 33, no. 1-2, p. 25-41. doi: 10.1016/j.jseaes.2007.10.020
- Bilham, R. (2004). Earthquakes in India and the Himalaya: tectonics, geodesy and history. *Annals of Geophysics*, 47(2/3), 839-858. doi: 10.4401/ag-3338
- Bilham, R., & Ambraseys, N. (2005). Apparent Himalayan slip deficit from the summation of seismic moments for Himalayan earthquakes, 1500-2000. *Current Science*, 88(10), 1658-1663.
- Bilham, R., & England, P. (2001). Plateau 'pop-up' in the great 1897 Assam earthquake. *Nature*, 410, 806-809. doi: 10.1038/35071057
- Biswas, S., and Grasmann, B., 2005, Quantitative morphotectonics of the southern Shillong Plateau (Bangladesh/India): *Austrian Journal of Earth Sciences* v. 97, p. 82-93.

- Biswas, S., Coutand, I., Grujic, D., Hager, C., Stockli, D., & Grasemann, B. (2007). Exhumation and uplift of the Shillong plateau and its influence on the eastern Himalayas: New constraints from apatite and zircon (U-Th-[Sm])/He and apatite fission track analyses. *Tectonics*, 26(6), 1-22. doi: 10.1029/2007TC002125
- Burgess, W. P., Yin, A., Dubey, C. S., Shen, Z. K., & Kelty, T. K. (2012). Holocene shortening across the Main Frontal Thrust zone in the eastern Himalaya. *Earth and Planetary Science Letters*, 357-358, 152-167. doi: 10.1016/j.epsl.2012.09.040
- Cattin, R., & Avouac, J. P. (2000). Modeling mountain building and the seismic cycle in the Himalaya of Nepal. *Journal of Geophysical Research*, 105(B6), 13389-13407. doi: 10.1029/2000JB900032
- Clark, M. K., 2012, Continental collision slowing due to viscous mantle lithosphere rather than topography: *Nature*, v. 483, p. 74-77. doi: 10.1038/nature10848
- Clark, M. K., & Bilham, R. (2008). Miocene rise of the Shillong Plateau and the beginning of the end for the eastern Himalaya. *Earth and Planetary Science Letters*, 269(3-4), 337-351. doi: 10.1016/j.epsl.2008.01.045
- De, R., and Kayal, J., 2003, Seismotectonic model of the Sikkim Himalaya: Constraint from microearthquake surveys: *Bulletin of the Seismological Society of America*, v. 93, no. 3, p. 1395. doi: 10.1785/0120020211
- De, R., and Kayal, J. R., 2004, Seismic activity at the MCT in SikkimHimalaya: *Tectonophysics*, v. 386, no. 3-4, p. 243-248. doi:10.1016/j.tecto.2004.06.013

- Drukpa, D., Velasco, A. A., & Doser, D. I. (2006). Seismicity in the Kingdom of Bhutan (1937-2003): Evidence for crustal transcurrent deformation. *Journal of Geophysical Research*, 111(B6), 1-14. doi: 10.1029/2004JB003087
- Fielding, E., Isacks, B., Barazangi, M., and Duncan, C., 1994, How flat is Tibet?: *Geology*, v. 22, no. 2, p. 163-167. doi: 10.1130/0091-7613(1994)0222.3.CO;2
- Fossen, H. (2010). *Structural Geology*. (1st ed.). New York, NY: Cambridge University Press.
- Gahalaut, V. K., Rajput, S., & Kundu, B. (2011). Low seismicity in the Bhutan Himalaya and the stress shadow of the 1897 Shillong Plateau earthquake. *Physics of the Earth and Planetary Interiors*, 186(3-4), 97-102. doi: 10.1016/j.pepi.2011.04.009
- Hirschmiller, J. (2013). Pliocene to recent shortening of the Siwalik group in the Himalayan foreland belt.
- Hodges, K. V. (2000). Tectonics of the Himalaya and southern Tibet from two perspectives. *GSA Bulletin*, 112(3), 324-350. doi: 10.1130/0016-7606(2000)1122.0.CO;2
- Jade, S., Bhattacharyya, A. K., Mukul, M., Vijayan, M. S. M., Jaganathan, S., Kumar, A., Tiwari, R. P., & Kumar, A., Kalita, S., Sahu, S.C., Krishna, A.P., Gupta, S.S., Murthyl, M.V.R.L., Gaur, V.K., (2007). Estimates of interseismic deformation in northeast India from GPS measurements. *Earth and Planetary Science Letters*, 263(3-4), 221-234. doi: 10.1016/j.epsl.2007.08.031

- Kapp, P., Yin, A., Harrison, T., and Ding, L., 2005, Cretaceous-Tertiary shortening, basin development, and volcanism in central Tibet: *Bulletin of the Geological Society of America*, v. 117, no. 7-8, p. 865-878. doi: 10.1130/B25595.1
- Kayal, J. R., Arefiev, S. S., Baruah, S., Hazarika, D., Gogoi, N., Gautam, J. L., Baruah, S., Dorbath, C., and Tatevossian, R., 2012, Large and great earthquakes in the Shillong plateau-Assam valley area of Northeast India Region: Pop-up and transverse tectonics: *Tectonophysics*, v. 532-535, no. C, p. 186-192. doi: 10.1016/j.tecto.2012.02.007
- King, G. C. P., Stein, R. S., & Lin, J. (1994). Static stress changes and the triggering of earthquakes. *Bulletin of the Seismological Society of America*, 84(3), 935-953.
- Lin, J., & Stein, R. S. (2004). Stress triggering in thrust and subduction earthquakes and stress interaction between the southern San Andreas and nearby thrust and strike-slip faults. *Journal of Geophysical Research*, 109(B02303), 1-19. doi: 10.1029/2003JB002607
- Meade, B. J. (2007). Present-day kinematics at the India-Asia collision zone. *Geology*, 35(1), 81-84. doi: 10.1130/G22924A.1
- Molnar, P. (1984). Structure and Tectonics of the Himalaya: Constraints and Implications of Geophysical Data. *Annual Review of Earth and Planetary Sciences*, 12, 489-518. doi: 10.1146/annurev.ea.12.050184.002421
- Molnar, P., & Stock, J. M. (2009). Slowing of India's convergence with Eurasia since 20 Ma and its implications for Tibetan mantle dynamics. *Tectonics*, 28 (3), 1-11. doi: 10.1029/2008TC002271

- Mukul, M., Jade, S., Ansari, K., & Matin, A. (2014). Seismotectonic implications of strike-slip earthquakes in the Darjiling-Sikkim Himalaya. *Current Science*, 106(2), 198-210.
- Najman, Y., Appel, E., Boudagher-Fadel, M., Bown, P., Carter, A., Garzanti, E., Godin, L., Han, J., Liebke, U., and Oliver, G., 2010, Timing of India-Asia collision: Geological, biostratigraphic, and palaeomagnetic constraints: *Journal of Geophysical Research: Solid Earth* (1978-2012), v. 115, no. B12. doi: 10.1029/2010JB007673
- Pognante, U., & Spencer, D. A. (1991). First report of eclogites from the Himalayan belt, Kaghan valley (northern Pakistan). *European Journal of Mineralogy*, 3(3), 613-618.
- Searle, M. P., Law, R. D., Godin, L., Larson, K. P., Streule, M. J., Cottle, J. M., & Jessup, M. J. (2008). Defining the Himalayan main central thrust in Nepal. *Journal of the Geological Society*, 165, 523-534. doi: 10.1144/0016-76492007-081
- Sukhija, B.S., Rao, M.N., Reddy, D.V., Nagabhusanam, P., Hussain, S., Chadha, R.K., Gupta, H.K., 1999. Timing and return of major paleoseismic events in the Shillong Plateau, India. *Tectonophysics* 308, 53-65. doi: 10.1016/s0040-1951(99)00082-7
- Tapponnier, P., Peltzer, G., Le Dain, A., Armijo, R., and Cobbold, P., 1982, Propagating extrusion tectonics in Asia: new insights from simple experiments with plasticine: *Geology*, v. 10, no. 12, p. 611-616. doi: 10.1130/0091-7613(1982)10<611:PETIAN> 2.0.CO;2
- Tapponnier, P., Xu, Z., Roger, F., Meyer, B., Arnaud, N., Wittlinger, G., and Jingsui, Y., 2001, Oblique stepwise rise and growth of the Tibet Plateau. *Science*, v. 294, no. 5547, p. 1671-1677. doi: 10.1126/science.105978

Toda, S., R.S. Stein, K. Richards-Dinger and S. Bozkurt, 2005, Forecasting the evolution of seismicity in southern California: Animations built on earthquake stress transfer, *Journal of Geophysical Research*, v. 110, B05S16, doi: 10.1029/2004JB003415

van der Beek, P., Robert, X., Mugnier, J. L., Bernet, M., Huyghe, P., & Labrin, E. (2006). Late Miocene – Recent exhumation of the central Himalaya and recycling in the foreland basin assessed by apatite fission-track thermochronology of Siwalik sediments, Nepal. *Basin Research*, 18(4), 413-434. doi: 10.1111/j.1365-2117.2006.00305.x

Velasco, A. A., Gee, V. L., Rowe, C., Grujic, D., Hollister, L. S., Hernandez, D., Miller, K. C., Fort, M., Harder, S., & Tobgay, T. (2007). Using Small, Temporary Seismic Networks for Investigating Tectonic Deformation: Brittle Deformation and Evidence for Strike-Slip Faulting in Bhutan. *Seismological Research Letters*, 78(4), 446-453. doi: 10.1785/gssrl.78.4.446

8.0 APPENDIX

<u>Figure 8.1 – Coulomb stress change along all receiver faults</u>	<u>120</u>
<u>Figure 8.2 – Coulomb stress change along all receiver faults</u>	<u>121</u>
<u>Figure 8.3 – Coulomb stress change along all receiver faults</u>	<u>121</u>
<u>Figure 8.4 – Coulomb stress change along all receiver faults</u>	<u>122</u>
<u>Figure 8.5 – Coulomb stress change along all receiver faults</u>	<u>122</u>
<u>Figure 8.6 – Coulomb stress change along the Dauki Fault</u>	<u>123</u>
<u>Figure 8.7 – Coulomb stress change along the Dauki Fault</u>	<u>123</u>
<u>Figure 8.8 – Coulomb stress change along the Dauki Fault</u>	<u>124</u>
<u>Figure 8.9 – Coulomb stress change along the frontal ramp of the MFT</u>	<u>124</u>
<u>Figure 8.10 – Coulomb stress change along the frontal ramp of the MFT</u>	<u>125</u>
<u>Figure 8.11 – Coulomb stress change along the Tista fault</u>	<u>125</u>

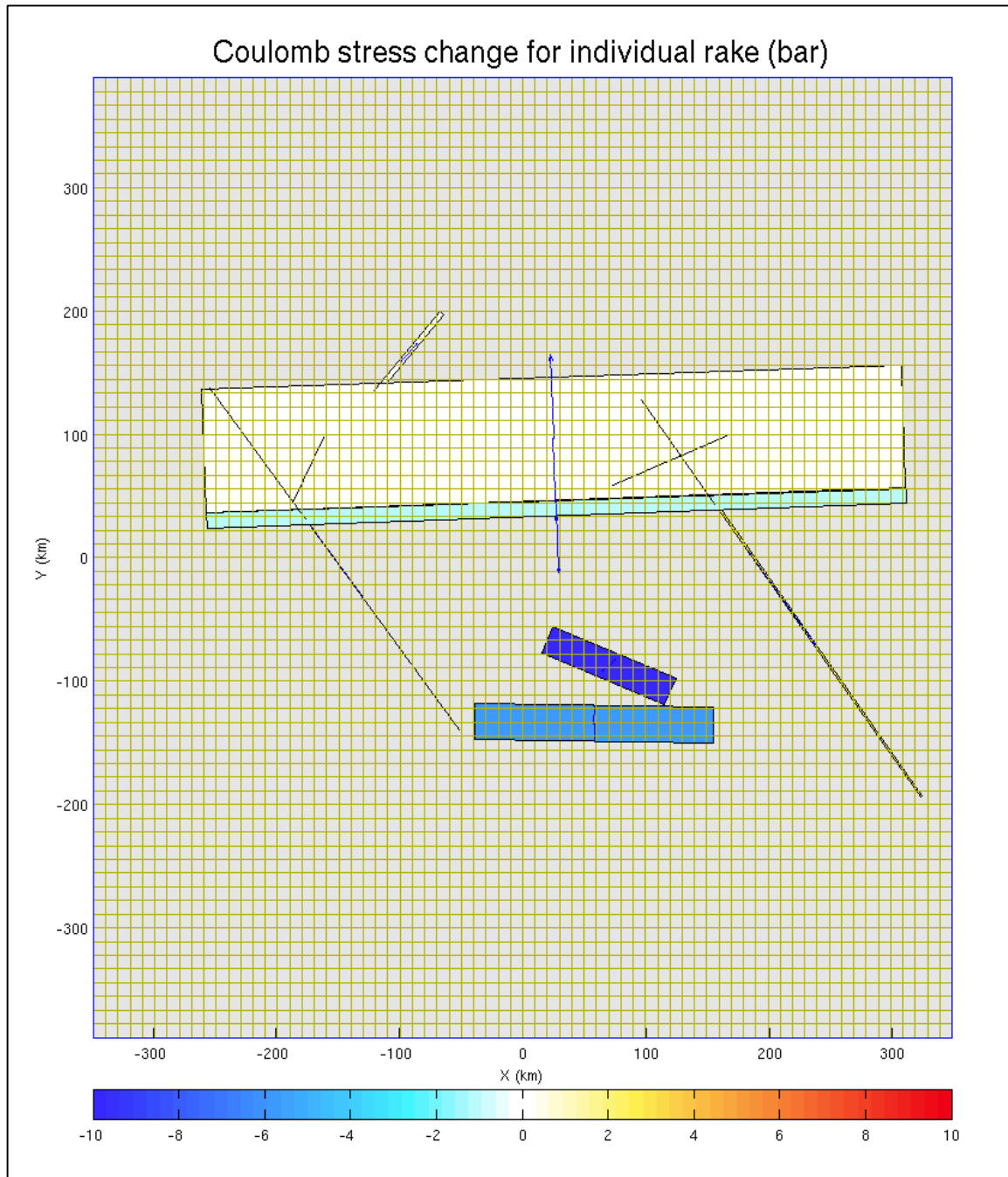


Figure 8.1: Coulomb stress change along all receiver faults as a function of individual rake. The calculation was modeled with a color saturation index of -10 to 10 bar.

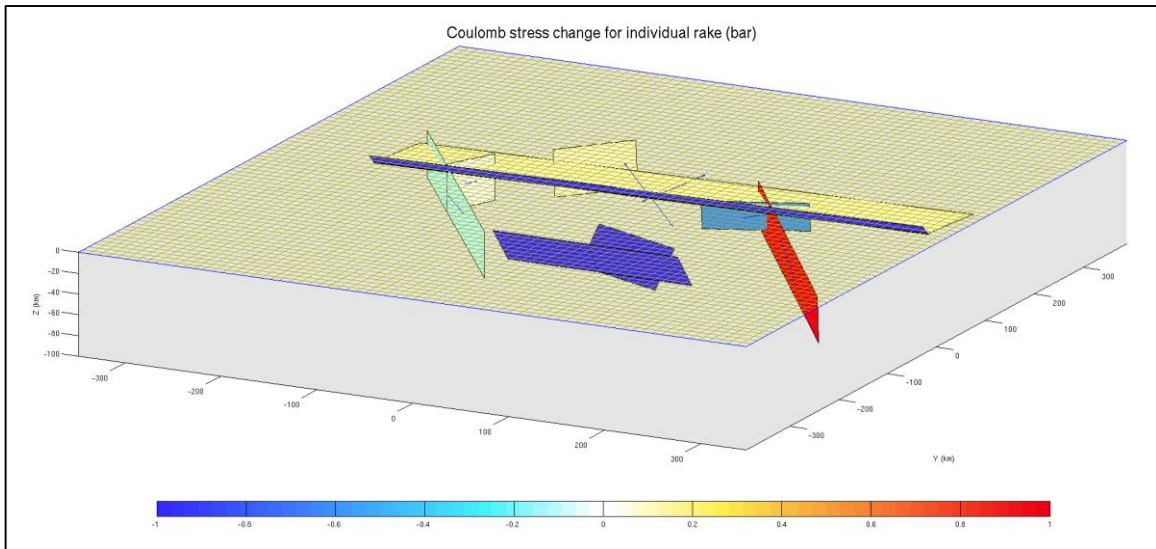


Figure 8.2: Coulomb stress change along all receiver faults as a function of individual rake. The calculation was modeled with a color saturation index of -1 to 1 bar.

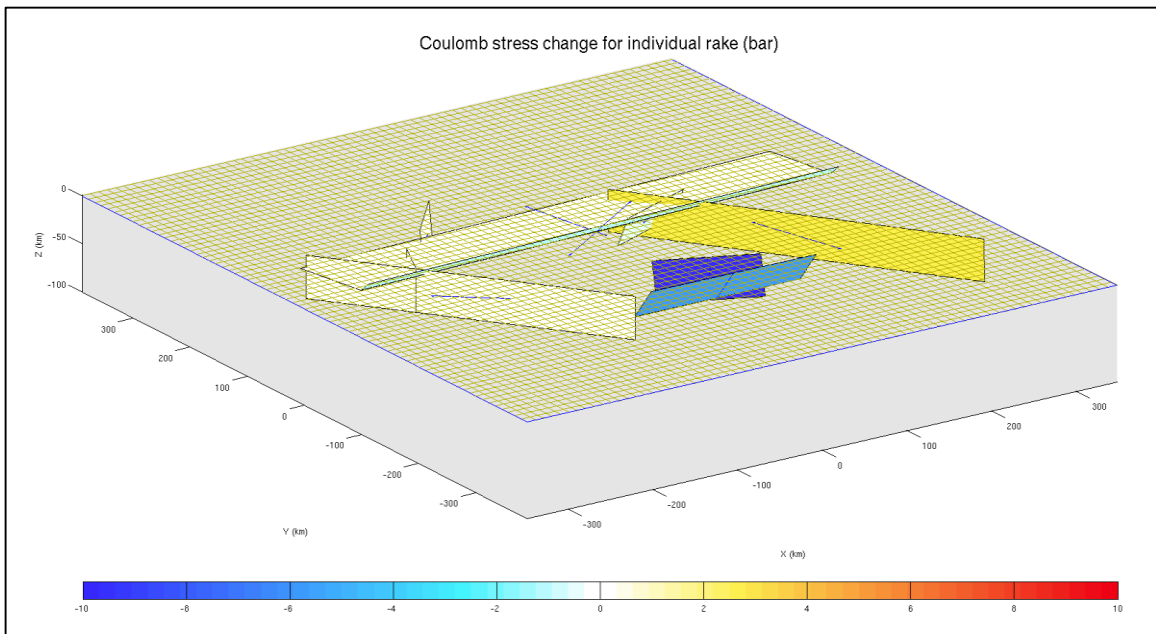


Figure 8.3: Coulomb stress change along all receiver faults as a function of individual rake. The calculation was modeled with a color saturation index of -10 to 10 bar.

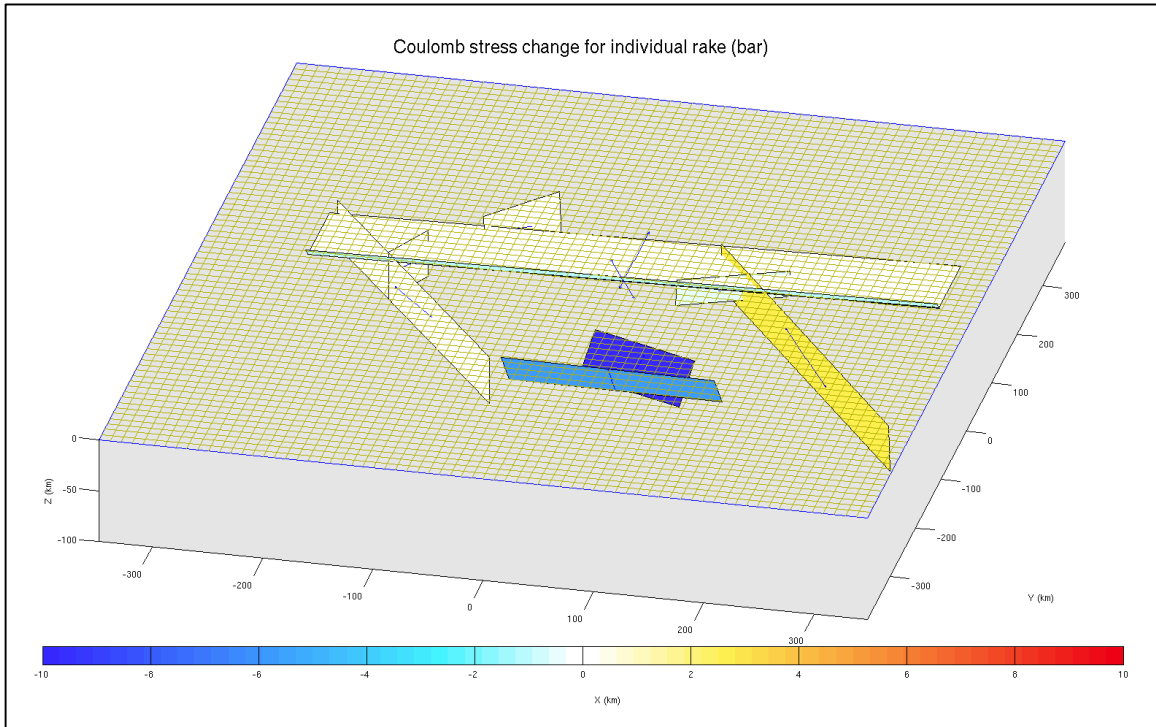


Figure 8.4: Coulomb stress change along all receiver faults as a function of individual rake. The calculation was modeled with a color saturation index of -10 to 10 bar.

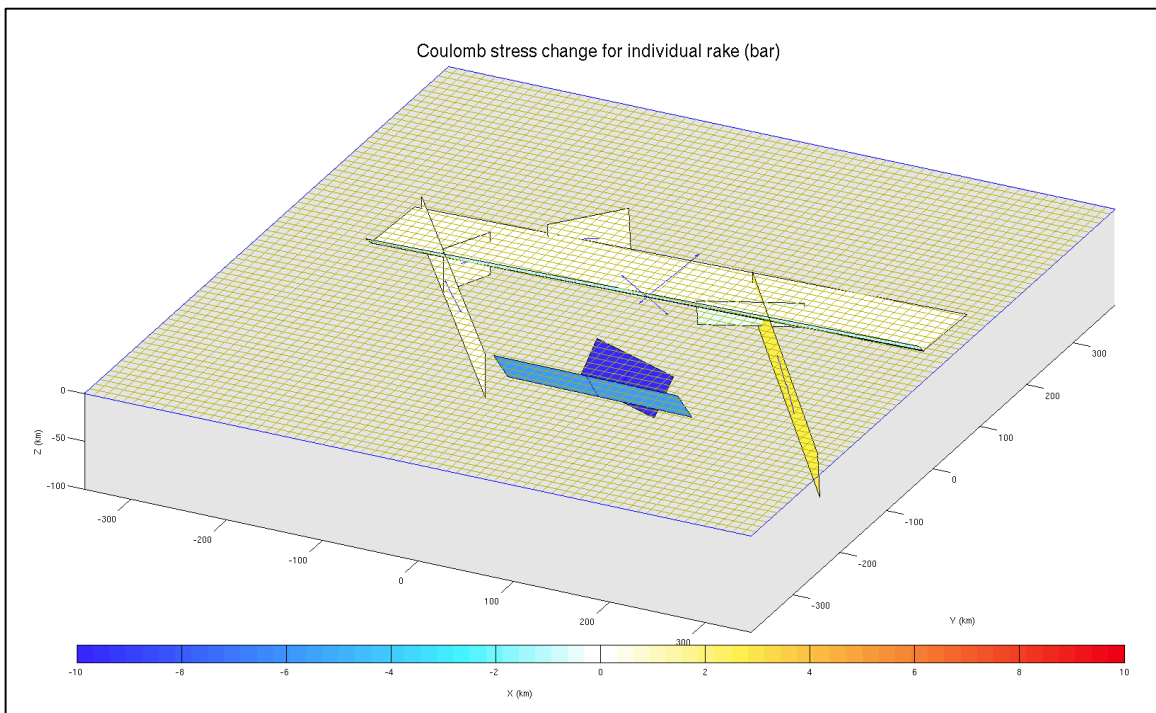


Figure 8.5: Coulomb stress change along all receiver faults as a function of individual rake. The calculation was modeled with a color saturation index of -10 to 10 bar.

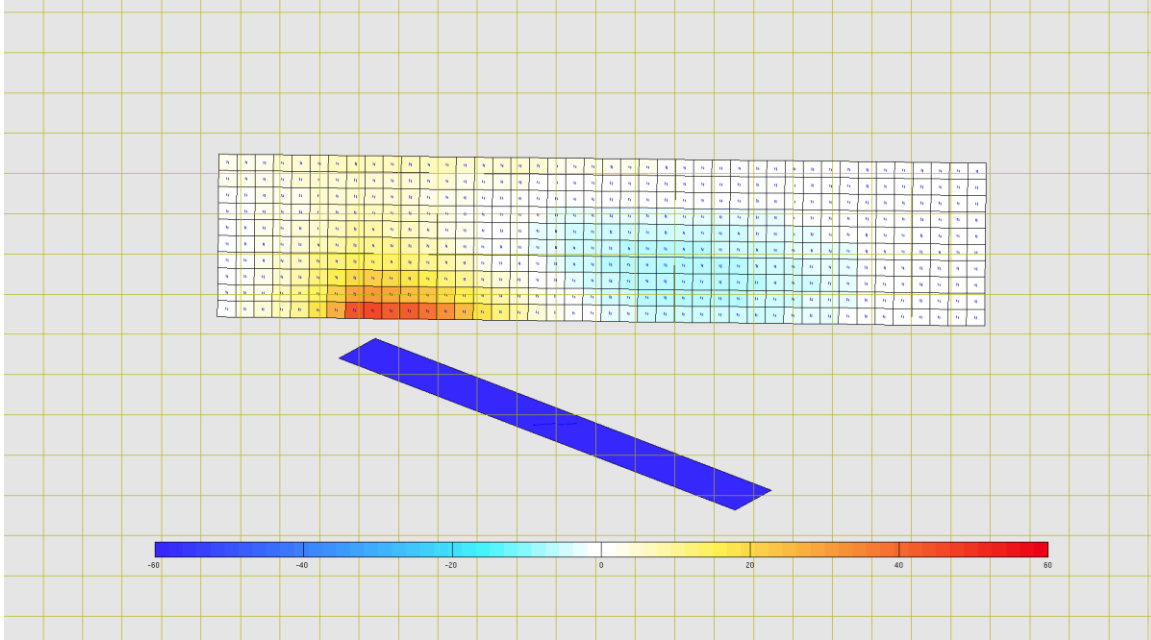


Figure 8.6: Coulomb stress change along the split Dauki fault as a function of individual rake. The calculation was modeled with a color saturation index of -60 to 60 bar.

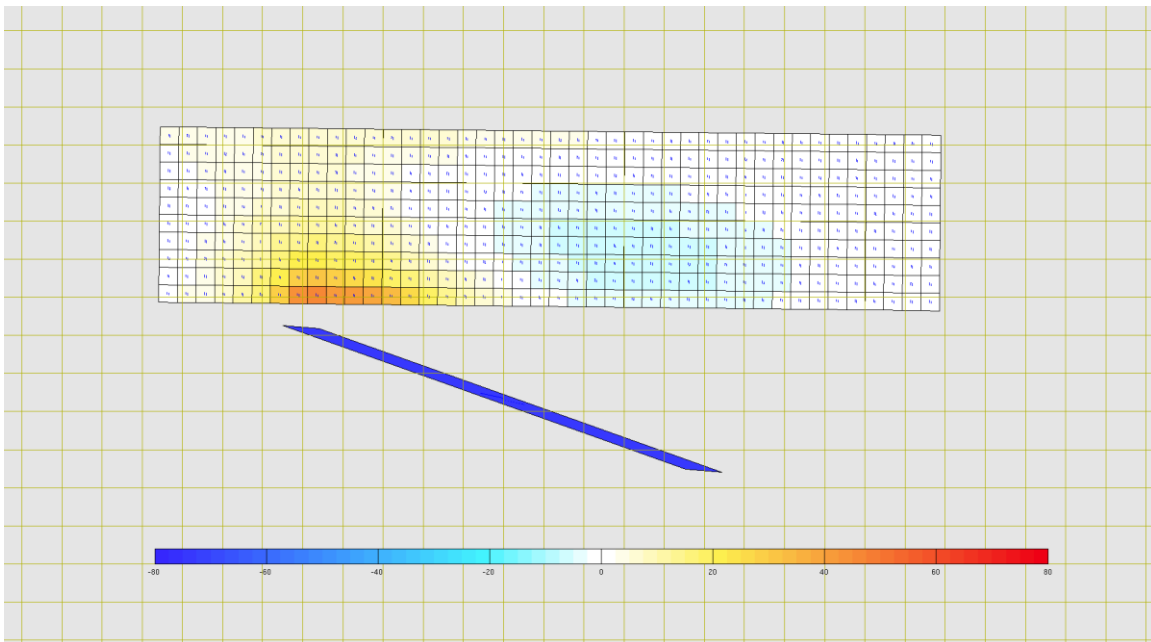


Figure 8.7: Coulomb stress change along the split Dauki fault as a function of individual rake. The calculation was modeled with a color saturation index of -80 to 80 bar.

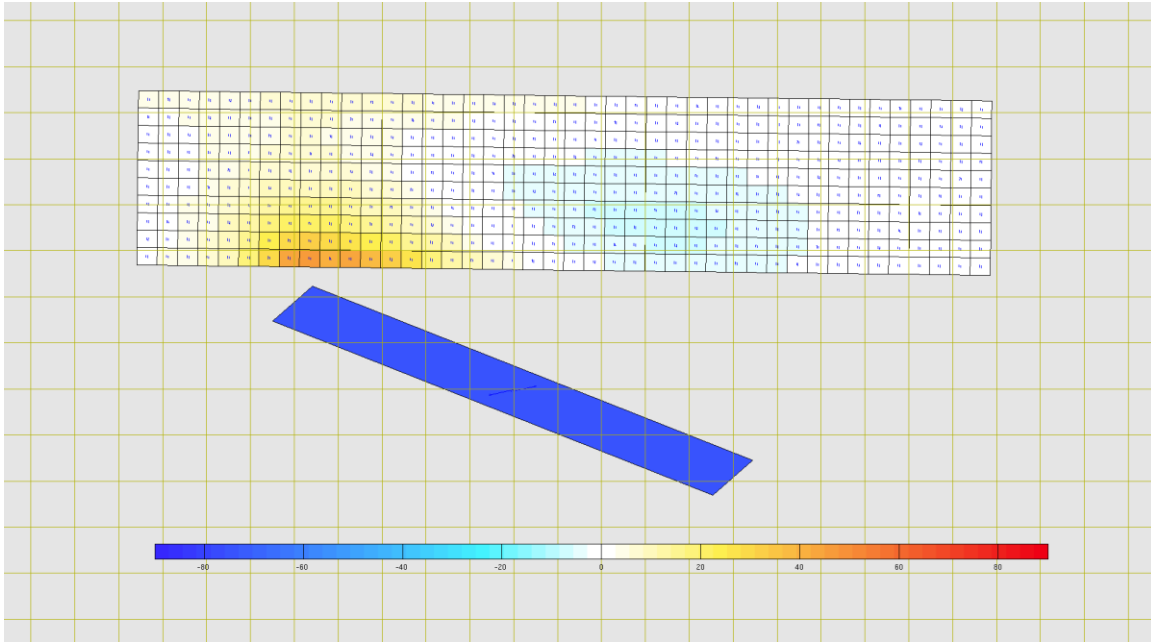


Figure 8.8: Coulomb stress change along the split Dauki fault as a function of individual rake. The calculation was modeled with a color saturation index of -90 to 90 bar.

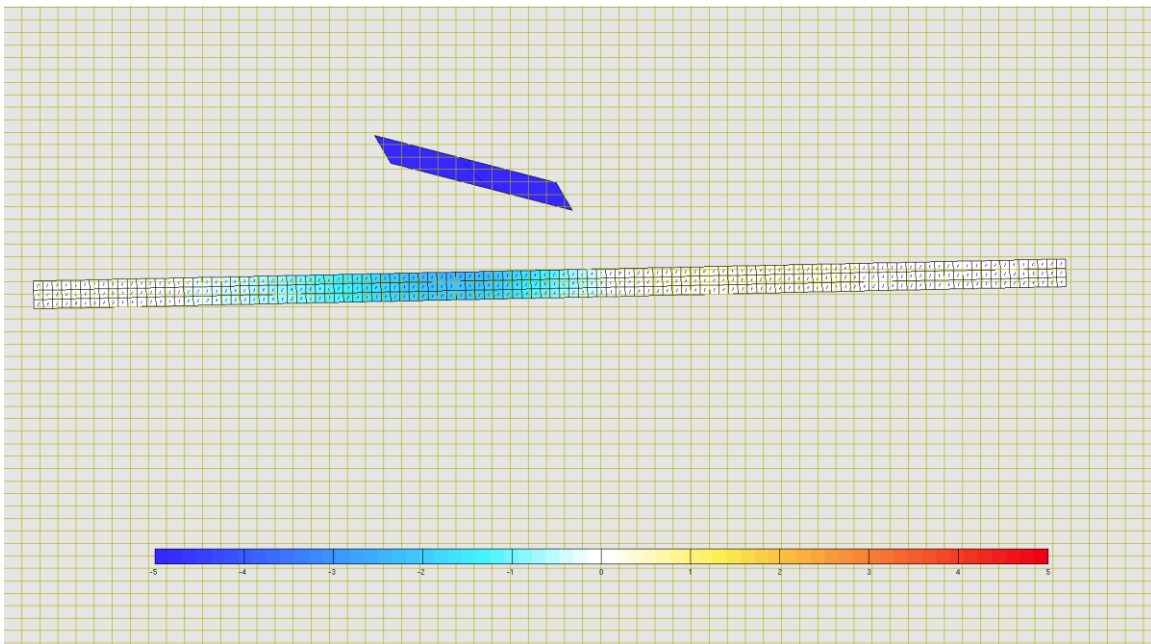


Figure 8.9: Coulomb stress change along the split frontal ramp of the MFT as a function of individual rake. The calculation was modeled with a color saturation index of -5 to 5 bar.

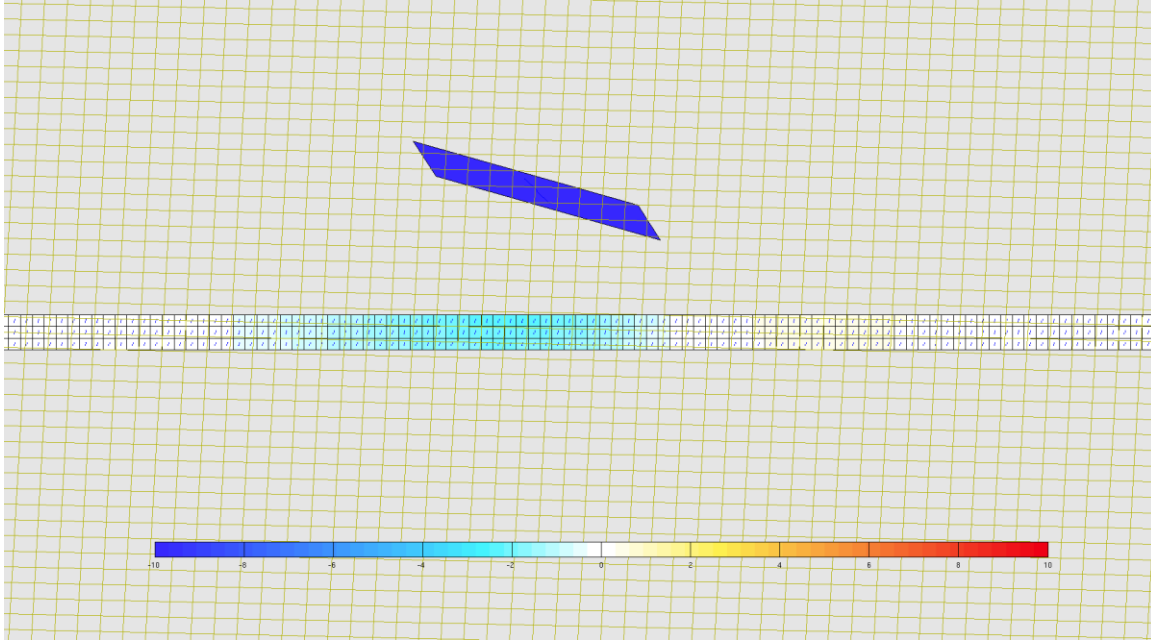


Figure 8.10: Coulomb stress change along the split frontal ramp of the MFT as a function of individual rake. The calculation was modeled with a color saturation index of -10 to 10 bar.

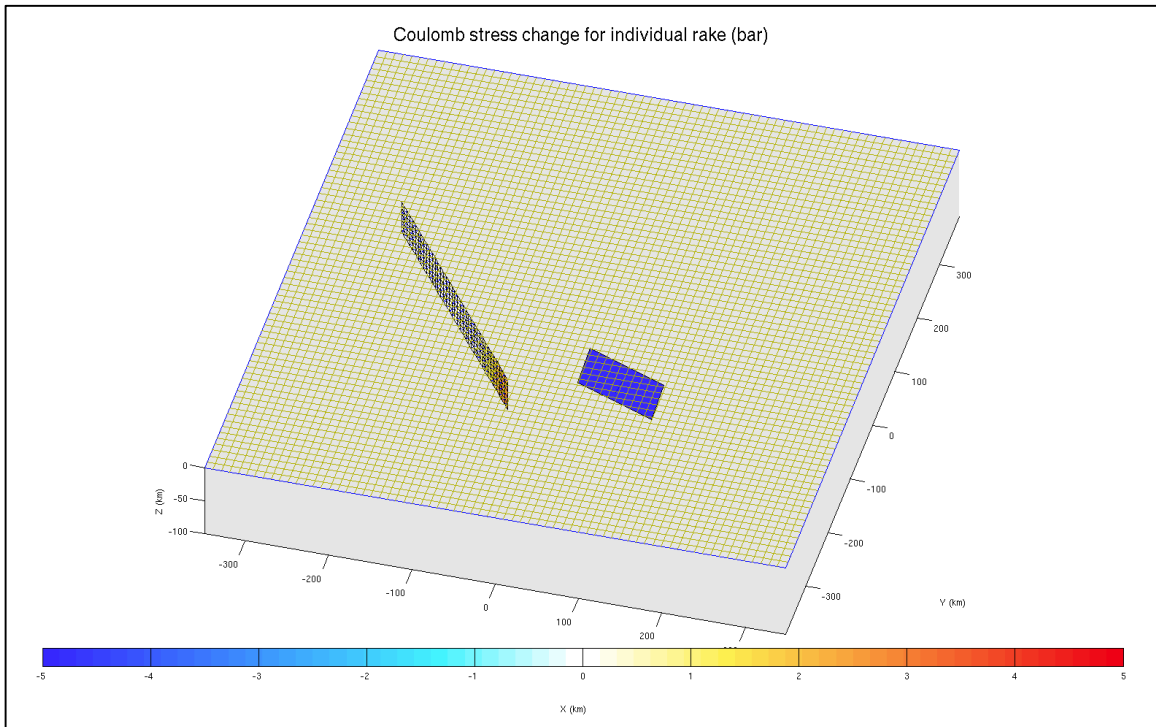


Figure 8.11: Coulomb stress change along the split Tista fault as a function of individual rake. The calculation was modeled with a color saturation index of -5 to 5 bar.